# Recent Advances of MOF-Based Nanoarchitectonics for Chemiresistive Gas Sensors

Jaydip D. Bhaliya[1] · Vraj R. Shah[2] · Gautam Patel[2] · Kalim Deshmukh[3]

## Abstract

It is sad but true that, as industrialization increases, a large number of hazardous gases are discharged into the environment, which can cause major health problems relating to respiratory disorders. Thus, to eliminate this pressing issue constant monitoring of air quality is mandatory, for this gas sensors play a huge role. There have been various gas sensors developed till now with respect to high sensitivity and selectivity. However, a sensor which having properties of high surface-to-volume ratio, good reactivity, long life cycles, and so on is difficult to produce. To remove this issue, a metal organic framework (MOF) can be utilized to measure various analytes as it has high sensitivity and selectivity. Further to upgrade the properties of a sensor in terms of optimum pore size, and high surface reactivity, which cannot only create a sensor with high efficiency, but also reduce energy consumption and maintenance, nanostructures have been incorporated into the MOFs. Furthermore, numerous reviews on gas sensing using MOF-based materials have been published. Only chemiresistive-based nanostructures embedded in MOF have yet to be described. In a nutshell, this review elicits thorough insightful details regarding advancements in MOF-derived nanostructure-based gas sensors for the measurement of various gas analytes, as well as the chemical mechanism, challenges associated with it, factors impacting the gas sensing process, and morphological data, which are also explained.

**Keywords**  MOFs · Chemiresistive gas sensor · Nanostructures · Gas sensing mechanism

## 1 Introduction

As we move into the twenty-first century, the pace of human life has been drastically altered due to the industrial revolution. Despite the enormous development, the threat of environmental damage is soared, particularly unhealthy air quality and enchanting effects such as climate change and global warming [1–5]. The measurement of air quality is becoming mandatory as it directly affects human health and public lifestyle. Numerous categories of hazardous gases and toxins are linked to health risks, hence there is a high demand for toxic gas monitoring. Varieties of sensor technologies have been developed to monitor various gases, and most of them require costly equipment, complicated process time as well as huge test times [6]. Therefore innovative sensing protocols are highly required to provide rapid detection, high sensitivity and selectivity, long-term stability, and real-time monitoring [7–10]. The sensor generally operates on the transduction function concept, which is based on changes in electrical or optical properties when it interacts with the target analytes and converts them into a detectable signal. Further, Temperature, selectivity, sensitivity, long-lasting stability, cost, and response/recovery time are all important sensing parameters to consider [11–13]. As a result, the selection of materials and their shape in gas sensors is critical to achieving good performance [14, 15]. Since the first chemiresistive gas sensors were built in the early 1960s using $SnO_2$ and ZnO, metal oxide semiconductor materials have been the leading contender for gas detection. On both academic and commercial platforms, the use of tin oxide ($SnO_2$), zinc oxide (ZnO), cobalt oxide ($Co_3O_4$), tungsten oxide ($WO_3$), and iron oxide ($Fe_2O_3$) has advanced the field

✉ Gautam Patel
gautampatel1573@yahoo.co.in

1   Polymers & Functional Materials Division, CSIR-Indian Institute of Chemical Technology, Uppal Road, Tarnaka, Hyderabad, Telangana 500007, India

2   Department of Applied Chemistry, School of Science, ITM SLS Baroda University, Vadodara, GJ 391510, India

3   New Technologies - Research Centre, University of West Bohemia, Plzeň, Czech Republic

of gas sensors. However, as these sensors frequently function at higher temperatures (200–500 °C), additional micro heaters must be included with the detecting material. Operating at high temperatures can result in problems like excessive power consumption, complicated manufacture, baseline drift, short lifetime, and deteriorating sensor sensitivity over time [16–19]. Besides this, metal oxide sensors are incapable of achieving great selectivity and consistent gas response in humid environments. As a result of the aforementioned difficulties, the use of sensors based on metal oxide will be hampered in the upcoming decades. So, lower usage of electricity, operations at room temperatures, consistent selectivity, and device structure downsizing are key requirements for modern gas sensor devices to be integrated into growing Internet of Things (IoT) systems [20–23].

To light shed on, Metal–organic frameworks (MOFs), a growing family of highly crystalline coordination polymers made up of organic linkers and metal-containing nodes, have a highly organized, adjustable porosity architecture, and have a large surface area [24]. In 1995, Yaghi and colleagues published the MOF idea, which has a great porosity of 60% and a huge surface area of 2900 $m^2$/g. Due to their varied architectures, more than 20,000 MOFs have been studied so far in a variety of research areas, including sensors, energy storage, catalysis, solar cells, and others [25]. Since MOFs are porous and have a large surface area, it is simple to interact with target gases quickly by adsorption and desorption to produce high sensitivity. Additionally, due to their selective gas penetration and adsorption properties, MOFs' adjustable structure could make it possible to easily fabricate a variety of nanomaterials and help to eliminate the selectivity issue in chemiresistive gas sensors [26–32]. The physicochemical and structural characteristics of MOFs would be significantly altered upon the adsorption of guest molecules, as well as their selectivity, which may be caused by contact between both the organic ligand's functional groups and the MOFs' active sites [26, 33–35]. Their capacity to attach to many analytes through H-bonds, electrostatic interactions and van der Waals interactions are further intriguing characteristics that make them exceptionally sensitive and selective materials for many gases [36–39]. In addition to this, MOFs could be employed as adaptable precursors to create different kinds of hybrid nanostructures, which demonstrated superior capabilities when used as gas sensing materials in comparison to their equivalents [39, 40]. Figure 1 elicits the number of publications based on MOFs usage as the gas sensor has exponentially surged over the period of 10 years.

Numerous reviews based on MOFs-based gas sensors have been published to date, such as recently Mahmoud and his group reported an article on MOFs-based sensors for gas sensing application, but more focus is devoted to the transduction function and random examples are depicted [40]. Then, in the year 2019 Zang et al. reported the
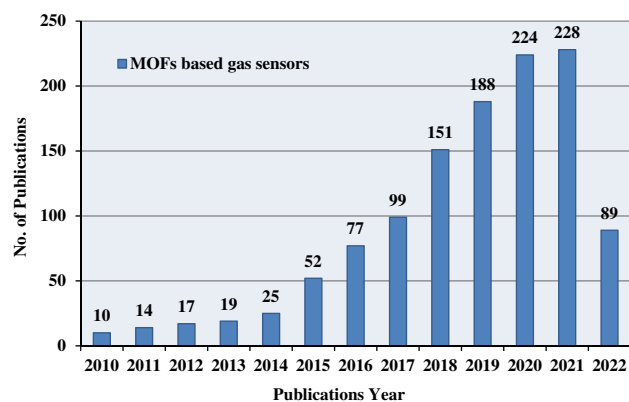


**Fig. 1** Hazardous gas and volatile organic compound (VOC) sensors based on metal–organic frameworks (MOF), and the total number of papers on MOFs in the previous ten years (Web of Science, accessed on 18th December 2022)

functionalized MOFs as a gas sensor, however, deep insights related to chemiresistive gas sensors are lacking, and also less examples concerning the integration of nanomaterial observed [41]. Further, in the year 2022, Zhao et al. had written a review paper that includes a detailed description of MOF as a gas sensor, but nowhere mentioned the morphological aspects or synthesis methods of the material is missing and also diverse focus is devoted in terms of sensing types [42]. Thus, to the best of our knowledge, it can be said that a comprehensive review on this topic is not been reported yet, hence, our aim in this paper is to narrate a detailed description related to MOFs embedded nanostructures as a gas sensor, particularly chemiresistive type for the detection of various oxidizing ($NO_2$, $CO_2$, $SO_2$, $O_2$, $O_3$, $Cl_2$), reducing ($H_2S$, $NH_3$, CO, NO, $CH_4$, $H_2$), and VOCs-volatile organic compounds (ethanol, formaldehyde, butanol, acetone and to a name of few.,). Along with this, this review also consists of the advanced synthesis techniques to produce MOFs-nanostructure with adequate properties, which are required to generate optimum gas sensors. Further, the in-depth sensing mechanism is explained with the aid of graphical representation. Lastly, the review ends with the challenges associated with the MOFs-based gas sensor and possibly future perspectives. The overview figure of the paper is illustrated in Fig. 2.

## 2 General Synthesis Methods

Metal–organic frameworks are made up of positively charged metal ions contained by organic molecules (MOF). Metal ions from nodes bind the organic molecule's arms together to form a repeating, cage-like structure. MOFs' primary fields of application include storage, sensing, catalysis, separation, drug delivery, and purification [43–47]. The
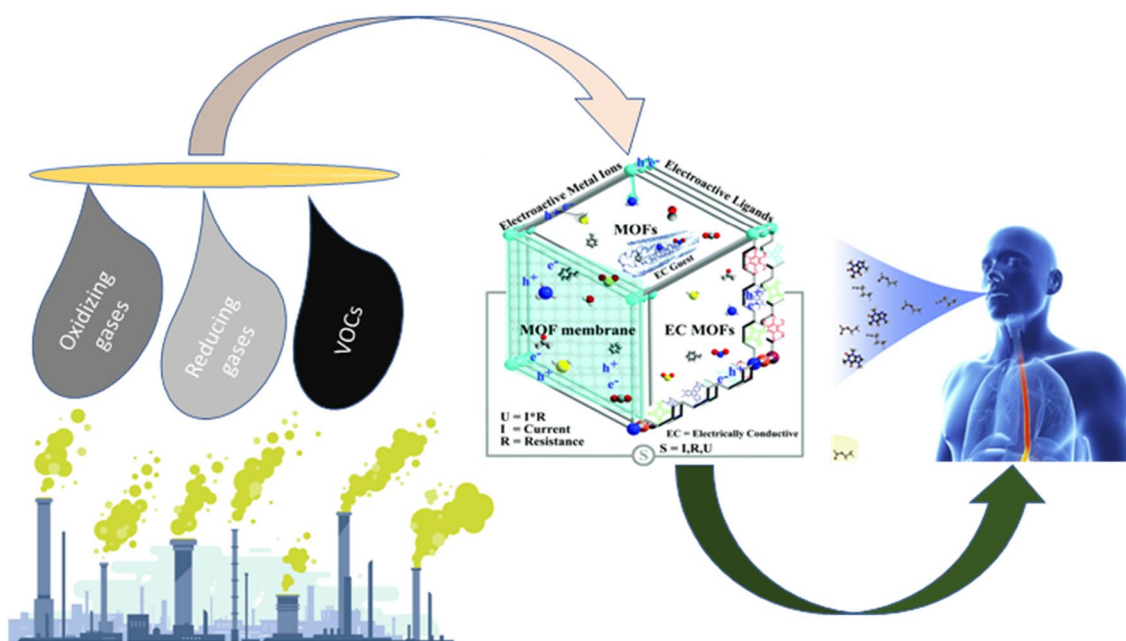
**Fig. 2** The overview of chemiresistive MOF-based gas sensors utilized for the detection of various toxic gases and eventually use to prevent respiratory-related health issues

synthesis of MOFs using traditional procedures and new methodologies is increasing interest among investigators because of its broad applications in a variety of sectors. MOFs can be produced via solvothermal, hydrothermal, slow diffusion, electrochemical, crystallization, mechanochemical, microwave-assisted synthesis, Sonochemical synthesis, and other methods depending on their final structure desired attributes and uses. As-synthesized MOFs can be used to create nanostructures using techniques such as hydrothermal, solvothermal, precipitation, co-precipitation, electrospinning, sol–gel process, and so on [48, 49]. Moreover, Fig. 3 elicits the overview of various fabrication methods utilized to develop MOFs-based nanostructure for chemiresistive gas sensing applications.

## 2.1 Hydrothermal and Solvothermal Method

The hydrothermal process, the most popular method of nanomaterial synthesis, can be used to create a wide range of morphologies. The autoclave is filled with reactants and water as a solvent, and the reaction is carried out under higher process conditions. Solubility in hot water at higher pressure is required for hydrothermal synthesis. Post-treatments like as annealing, calcination, drying, and so on are sometimes provided following an autoclave treatment. Current approaches have significant chemical activity, improved solubility at higher temperatures and pressures,

size controllability, and other advantages, whereas the need for an expensive autoclave and safety concerns are drawbacks [50–54].

One of the potential protocols for the synthesis of metal organic frameworks is solvothermal. This approach is similar to the hydrothermal method, except that an organic solvent is used instead of water. The solvent is employed in the Solvothermal process, and the reaction temperature is often higher than the solvent's normal boiling point. A bomb or autoclave-like confined vessel speeds up the process at high temperatures by boosting solubility. The precursor may be intractable or less soluble under normal temperature and pressure conditions, but at its critical point, solubility increases, and compounds are easily solubilized. Following the reaction time, nonmaterial frameworks are cleaned with water or alcohol to eliminate impurities before being vacuum dried [55, 56]. Variations in reaction time, temperature, pressure, pH, concentration, autoclave volume, and other factors alter the size, shape, structure, and characteristics of nanomaterials, allowing materials to be simply and effectively designed. Because it is performed at higher temperatures, the solvothermal approach addresses the major issue of heavy organic material solubility. Another benefit is the quick nucleation of uncommon compounds. The viscosity of water is lowered as the temperature rises, favoring the mobilization of a precursor [57–59]. Both methods have been widely utilized to develop a variety of nanostructures.
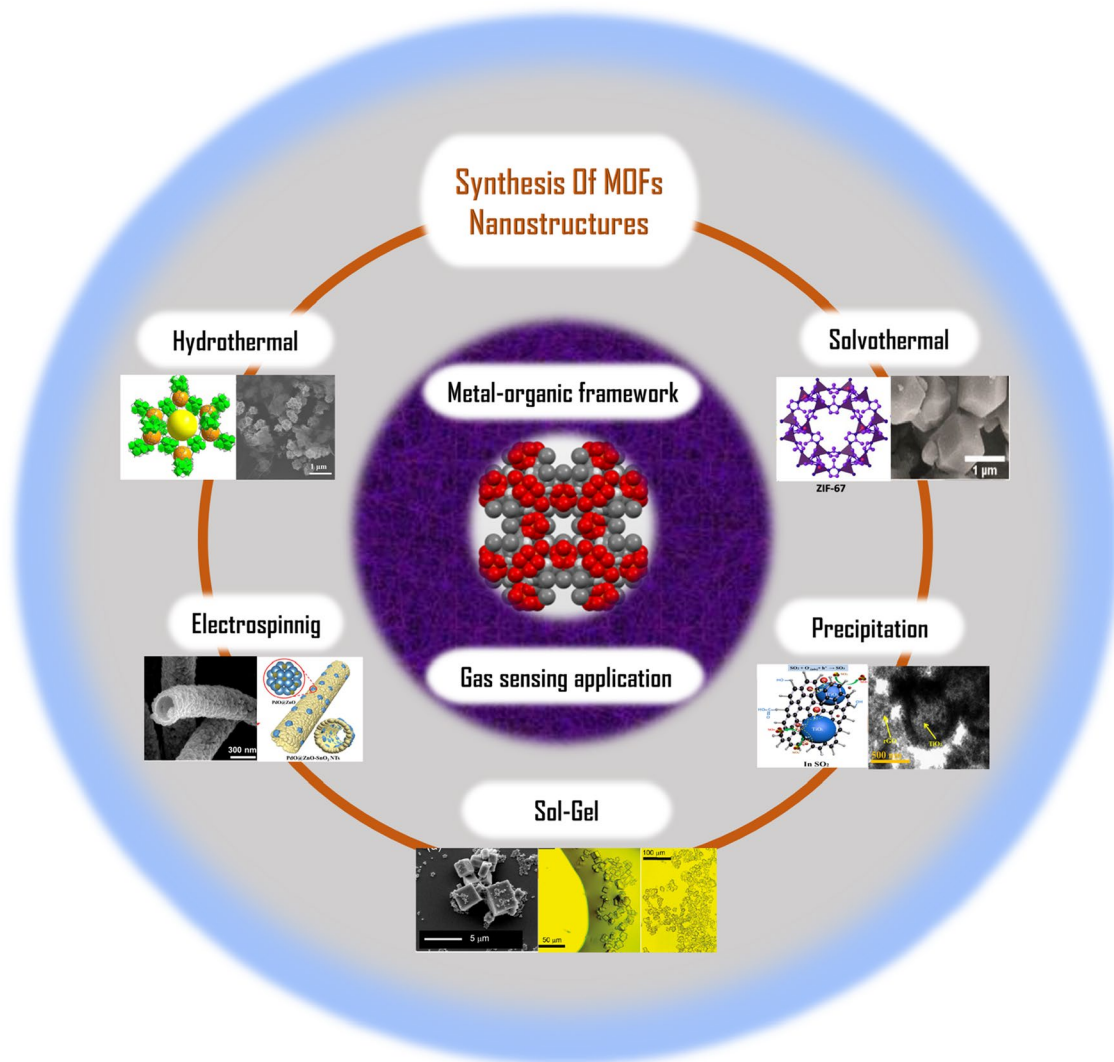
**Fig. 3** Pictrorial illustration of various fabrication methods and its morphology to develop MOFs-nanostructure

## 2.2 Precipitation Method

To prepare the solution, the precipitation method uses the right solvent to dissolve the precursor. Slow or drop-wise addition of precipitating chemicals causes nucleation, followed by growth, and formation of the desired product precipitates. Impurities are removed by washing with water or alcohol. The resulting precipitates are dried. The precipitation method has several advantages, including environmental friendliness, low cost, higher purity, higher yield, normal process conditions, and so on. The key obstacles encountered during the manufacturing of nanostructures using this technology are control of particle size and form, as well as crystallinity [60, 61].

## 2.3 Electrospinning Method

The most dependable technique for producing MOF nanofibers. This process produces one-dimensional nanomaterials such as nanofiber, nanorods, nanotubes, and nanowires. Electrospinning can be used to create a nonwoven web of nanofibers by providing stronger electrical fields between the syringe and the collector. The solution or liquid extrudes from the needle or nozzle, forming a jet that is collected on a collector (e.g., aluminum or stainless steel foil) to produce fibers [62]. At a greater temperature, the fibers are calcined again. The electrospinning process is heavily influenced by parameters such as viscosity, voltage, pressure, flow velocity, temperature, and so on. This technology has advantages

such as cost-effectiveness, manufacturing fibers with a large surface area, a greater aspect ratio, easy processing, and good mechanical strength of nanofibers, but it cannot readily construct big volume scaffolds [63, 64].

## 2.4 Sol–Gel Method

The sol–gel process involves the formation of a colloidal solution- Sol- through hydrolysis and condensation reactions, to which a catalyst is added to produce the gel. This method produces material with a regular solid backbone surrounded by liquid. The removal of the solvent phase in supercritical drying or evaporative drying makes the structure more porous in nature. This process is more compatible with other traditional procedures, and the as-synthesized material can be shaped into a variety of nanostructures [65, 66].
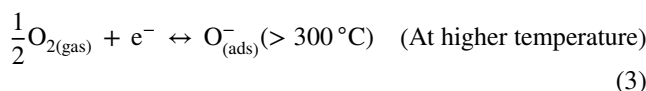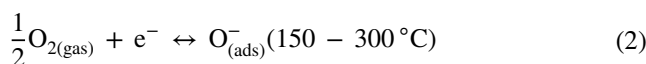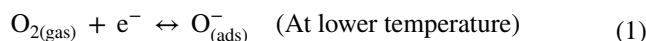
Based on a detailed literature survey, a compiled report for the above-discussed methods is tabulated in Table 1.

Table 2 elicits the information regarding various metal–organic framework materials-synthesis routes followed by its merits as well as demerits for the material properties. MOF synthesized by methods like hydrothermal, precipitation, crystallization, sol–gel, etc. can be utilized as precursors to synthesize various nanostructures. Usage of MOF as a precursor furnishes benefits like desired topological textures, implementation of desired properties in the structure, reduction in undesired structure collapse during calcination, etc. Enhanced sensing potential is also observed for MOF-derived sensors. Figure 4 indicates the fabrication method appropriate for detecting toxic analytes in a specific temperature range.

# 3 General Gas Sensing Mechanism of MOFs-Based Gas Sensor

In general, the sensing mechanisms and sensing operations of MOFs are determined by major components such as metal oxide, 2D materials, carbon nanomaterials, and so on due to their high compatibility and diversity [90]. Chemiresistive gas sensors using metal oxides are very well known and they operate based on surface reactions or adsorptions of gases by the transfer process of electrons and holes [91]. Therefore, when sensing materials interact with the target gases or adsorbed oxygen, the conductance (or resistance) change occurs. In the case of MOF-chemiresistors, functional groups and metal nodes act as an adsorption site and cause conductivity change by a redox reaction. Moreover, chemiresistive-based sensors provide a simple sensing mechanism, compatibility with electronic devices, and low-cost fabrication. The common in-depth mechanism can be explained as, when the MOF-based sensor is situated in the air, the electrons inside the materials are being absorbed by the oxygen molecules. As a result, resistance in the material increases [92]. Likewise, when any reducing gas approaches the surface, it makes the bond with oxygen molecules and trapped electrons are pushed back into the material. Through this process, the difference created in terms of resistance and that difference can be calculated as the sensor sensitivity. The process may be seen in a reverse manner in the case of the oxidizing gas. Apart from this, the pictorial representation of the MOF-based gas sensor sensing mechanism can be observed in Fig. 5 [93, 94]. The generation of oxygen ions generally depends upon the temperature. The following reaction Eqs. 1, 2, 3 includes the number of oxygen ions based on various temperature ranges:

$$O_{2(gas)} + e^- \leftrightarrow O^-_{(ads)} \quad \text{(At lower temperature)} \tag{1}$$

$$\frac{1}{2}O_{2(gas)} + e^- \leftrightarrow O^-_{(ads)}(150 - 300\,°C) \tag{2}$$

$$\frac{1}{2}O_{2(gas)} + e^- \leftrightarrow O^-_{(ads)}(> 300\,°C) \quad \text{(At higher temperature)} \tag{3}$$

## 3.1 Significant Parameters in the Gas Sensing Process

The gas sensing parameters are very significant in order to understand the proper mechanism of gas sensing devices. Apart from that, through these parameters observation can be made, and also comparison can be done in terms of new sensor results and conventional sensors [95–97].

### 3.1.1 Sensor Response or Sensitivity (S)

The often-used definitions of S are the following: A ratio of resistance in the air to that exposure of gas i.e.

$$S = R_{air}/R_{gas}, \textbf{for reducing gas}\,(\textbf{like NH}_3,\ \textbf{H}_2\textbf{S},\ (\textbf{CH}_3)_2\textbf{CO})$$

$$S = R_{gas}/R_{air}, \textbf{for oxidizing gas}\,(\textbf{like NO}_2,\ \textbf{O}_3,\ \textbf{Cl}_2)$$

A high S value for a specific gas indicates that the material is highly sensitive, but that the high S value is dependent on the high surface area, surface reaction, or adsorption–desorption to achieve a higher response.

### 3.1.2 Response/Recovery Time

The reaction time is the period of time during which, when exposed to the target gas, the resistance reaches 90% of its final value from the baseline, and the recovery time is the

**Table 1** Fabrication of sensing elements by different methods

| Method | MOF | Sensing element | Major process condition | Shape | Target | References |
|---|---|---|---|---|---|---|
| Solvothermal followed by ultrasonication | [Cd(L1) (DMF)3 | CdO | 100 °C , 72 h | Nanoparticles | – | [50] |
| Solvothermal followed by thermal decomposition | MOF 5 | ZnO | 140 °C , 3 h | Nanocages | VOCs- Benzene, acetone | [55] |
| Co-precipitation followed by thermal decomposition | ZIF 67 | $Co_3O_4$ | RT | Nanoparticles | Acetone | [57] |
| Hydrothermal followed by calcination | Sn/Ni-based MOF | $SnO_2/NiO$ | 180 °C , 12 h | Nano flakes | TEA | [64] |
| Solvothermal followed by calcination | HKUST | $CuO/Cu_2O$ | 30 min stirring | Cages (Octahedra, truncated octahedra, cube) | Ethanol | [67] |
| Simple precipitation | ZIF 67 | $Co_3O_4$ | RT, 6 h | Nanocubes | Ethanol | [68] |
| Hydrothermal followed by annealing | MIL-53 | $Fe_2O_3$ $(PrFeO_3/\alpha-Fe_2O_3)$ | 140 °C ,20 h | Nano octahedron | Ethyl acetate | [69] |
| Hydrothermal | | $\alpha-Fe_2O_3$ | 120 °C , 20 h | Nano-Ellipsoids | $H_2S$ | [70] |
| Precipitation followed by calcination | ZIF 8 and ZIF 67 | $ZnO/Co_3O_4$ | RT | Nano-polyhedrons | Acetone | [71] |
| Hydrothermal followed by annealing | Sn/Ni-based MOF | $NiO-SnO_2$ | 150 °C , 24 h for Sn and 160 C, 6 h for nickel | Nanoplates | $NO_2$ | [72] |
| Hydrothermal followed by annealing | NiO based MOF | Fe/NiO | 160 °C , 12 h | Nest like Nanosheet | TEA | [73] |
| Precipitation followed by annealing | ZIF 67 | $CoSe_2$@NC/ MWC-NTs | RT | Nanotubes | $NH_3$ | [74] |
| Solvothermal | ZIF 8 | ZIF-8/ Pd/ZnO | 100 °C , 24 h | Nanowire | $H_2$ | [75] |
| Hydrothermal and solvothermal followed by calcination | MIL-125 | $TiO_2$ | 150 °C , 240 h | Nanosphere, nano-flowers | Humidity | [76] |
| Co-precipitation | Fe based MOF | $Fe_2O_3$ | 80 °C , 12 h | Nanoparticles | n-Butanol | [77] |
| Hydrothermal followed by thermolysis | MIL 88A | $\alpha-Fe_2O_3$ | 100 °C , 12 h | Nanorods | Acetone | [78] |
| Precipitation | Cu-MOF | $Au-SH-SiO_2$@Cu-MOF | RT | Nano-particles | Hydrazine | [79] |
| Precipitation followed by electrospinning and calcination | ZIF 8 | Zn doped $SnO_2$ | RT for precipitation and 15 kV for spinning | Nanofiber | Formaldehyde | [80] |
| Precipitation followed by Electrospinning and calcination | ZIF 8 | $PdO$@$ZnO-SnO_2$ | 16 kV for electrospinning | Nanotubes and nanofibers | Acetone | [81] |

**Table 2** MOF-based materials for chemiresistive sensors, as well as a comparison of the advantages and disadvantages of the synthesis method for material properties
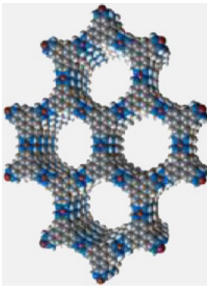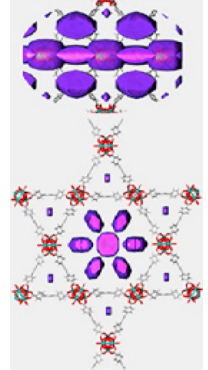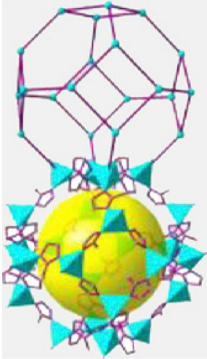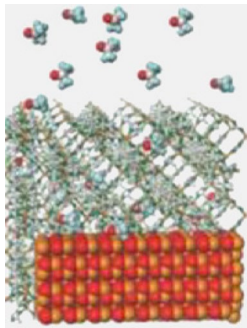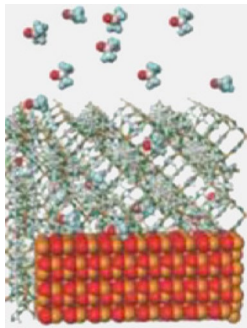
| Classification | Example | Synthetic method | Advantages | Disadvantages | References |
|---|---|---|---|---|---|
| Conductive MOFs (at r.t.) | Cu$_3$(HITP)$_2$ (through-bond)  | • Solvothermal hydrothermal<br>• Layer-by-layer spray coating<br>• In-situ growth on supports | • High surface area<br>• Micro- or mesoporous structure<br>• Operation at r.t<br>• Noticeable sensitivity at r.t | • Low selectivity<br>• Poor stability<br>• Low reproducibility<br>• Limited strategies for sensor fabrication w/o a loss of activity of MOFs | [82] |
| | tin oxide_Nu-1000 (through-space)  | • Deposition of conducting agents to MOFs<br>• Hydro- or solvothermal | • High surface area<br>• Micro- or mesoporous structure<br>• Operation at r.t | • Low sensitivity<br>• Low selectivity<br>• Poor stability<br>• Low reproducibility | [83] |
| 3D MOFs (not conductive at r.t.) | ZIF-67  | • Synthesis at r.t<br>• Solvothermal<br>• Hydrothermal | • Ultrahigh surface area<br>• Micro- or mesoporous structure | • Deprived conductivity<br>• Deprived stability<br>• High operating temp<br>• Low sensitivity<br>• Low selectivity | [84] |
| MOF-metal oxide composites | ZnO@ZIF-CoZn  | • In-situ growth by r.t. synthesis<br>• In-situ growth by hydro or Solvothermal | • Micro- or mesoporous structure<br>• Enhanced sensitivity<br>• Enhanced selectivity<br>• Durability to humidity | • Not uniform deposition of diverse MOFs<br>• Limited strategies for efficient fabrication of sensing devices<br>• High operating temp<br>• Poor long-term stability | [85] |

**Table 2** (continued)
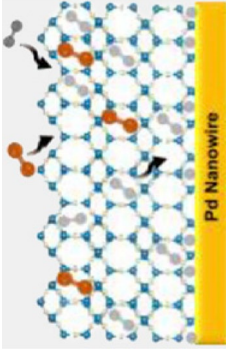
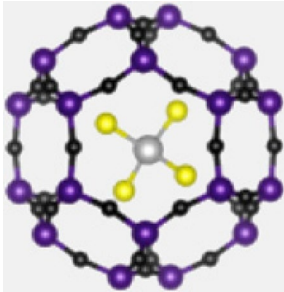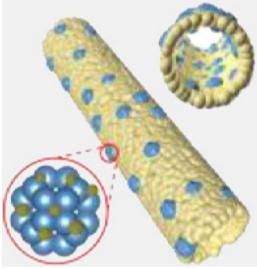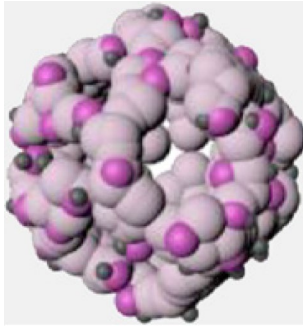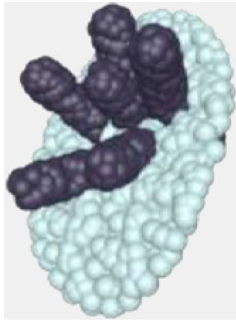| Classification | Example | Synthetic method | Advantages | Disadvantages | References |
|---|---|---|---|---|---|
| MOF-metal composites |  Pd nanowire@ZIF-8 | • In-situ growth by r.t. synthesis<br>• In-situ growth by hydro or solvothermal | • Micro- or mesoporous structure<br>• Selective gas separation and adsorption<br>• High selectivity or fast sensing speed | • Low response<br>• Not uniform Deposition of diverse MOFs<br>• Limited strategies for efficient fabrication of sensing devices | [86] |
| Carbon composites |  carbon-WS$_2$ composites | • Integration of MOF with active materials<br>• Pyrolysis | • High surface area micro- or mesoporous structure<br>• Operation at low temp<br>• Noticeable sensitivity at r.t<br>• improved selectivity | • Vulnerability to humidity<br>• Low reproducibility<br>• Slow sensing speed<br>  poor long-term stability<br>• Poisoning of active materials | [87] |

**Table 2** (continued)

| Classification | Example | Synthetic method | Advantages | Disadvantages | References |
|---|---|---|---|---|---|
| Metal oxides | PdO@ZnO loaded SnO2 nanotubes<br> | • Electrospinning of MOFs or metal@ - MOFs<br>• Subsequent calcination | • Meso- or macroporous structure<br>• High sensitivity<br>• Improved selectivity<br>• High thermal and<br>• Chemical stability | • High operating temp<br>• Vulnerability to humidity<br>• Baseline drift during<br>• Long-term operation<br>• Catalyst poisoning | [81] |
| | PdO-loaded SnO$_2$-Co$_3$O$_4$ hollow cubes<br> | • Durability to humidity<br>• Post-treatment of metal @ MOF-derived metal oxides | • Meso- or macroporous structure<br>• High sensitivity<br>• Improved selectivity<br>• High thermal and chemical<br>• Stability | • High operating temp<br>Vulnerability to humidity<br>• Baseline drift during<br>• Long-term operation catalyst poisoning | [88] |
| | Co$_3$O$_4$ @ZnO sheet<br> | • Morphology & composition control of MOFs<br>• Subsequent calcination | • Meso- or macroporous structure<br>• Enhanced sensitivity high thermal/chemical stability | • High operating temp<br>• Vulnerability to humidity<br>• Low selectivity<br>• Baseline drift during long-term operation | [89] |
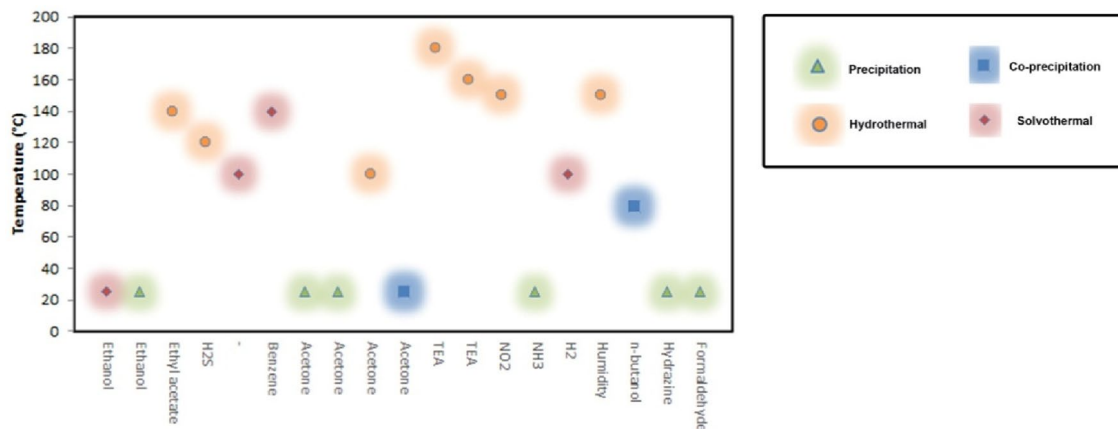
**Fig. 4** Based on literature the pictorial illustration depicts the MOF-based material used to detect toxic gases synthesized by which specific method at a specific temperature [50, 55, 57, 64, 67–81]
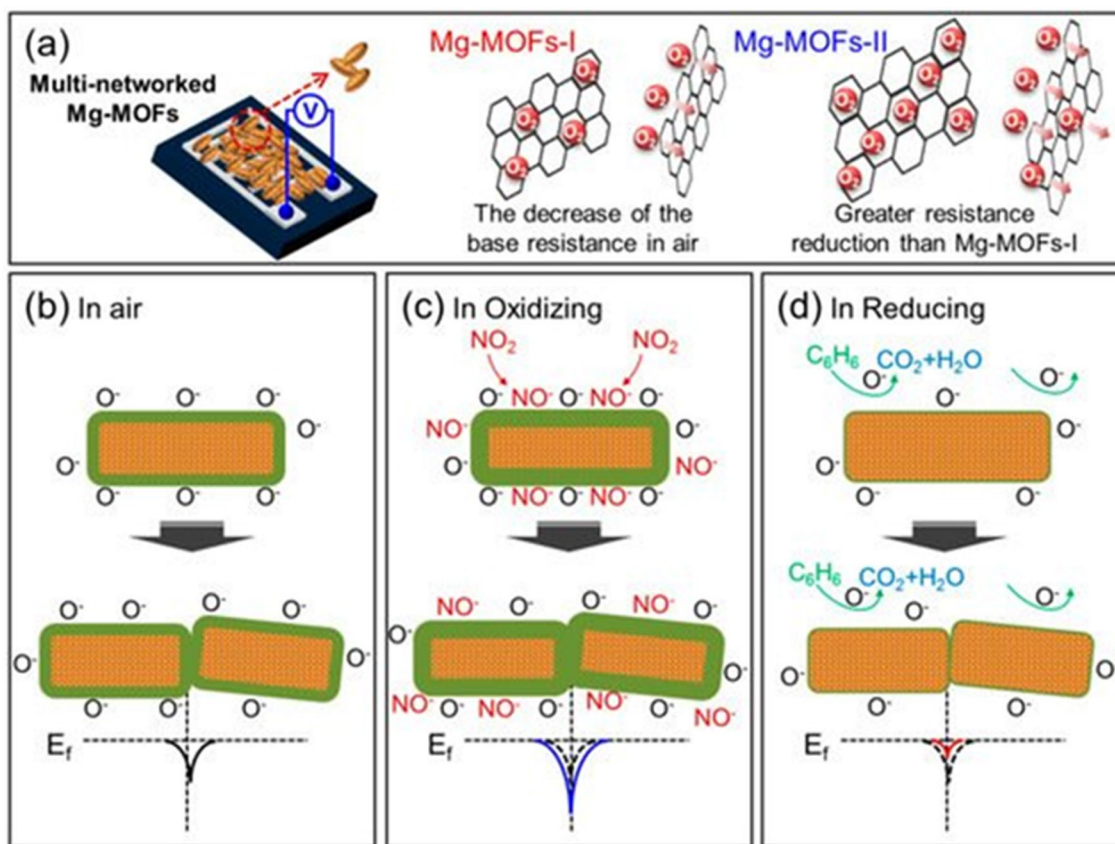


**Fig. 5 a** Resistance change phenomenon while exposed to analytes; **b** Alteration in potential barrier in the atmosphere of air; **c** Reaction mechanism and change in potential barrier while exposed to oxidizing gas, **d** Reaction mechanism and change in potential barrier while exposed to reducing gas [94]

period of time during which, when exposed to clean air, the sensor resistance has reached up to 10% of the saturation value. So that it may be used again, a good sensor should have a quick recovery and response time.

### 3.1.3 Selectivity

The most critical factor is selectivity because numerous interfering gases can harm the sensor device and shorten its

life. A sensor's selectivity or specificity toward an analyzing gas is represented in terms of dimension, which compares the concentration of the matching target gas that produces the same sensor signal. Surface modification with noble metals or doping can improve the sensor's selectivity even further.

### 3.1.4 Long-Term Stability

The sensor's long-term stability displays its capacity to preserve its qualities when operated continuously for lengthy periods of time in a hostile environment. Good sensors should last for several years with no drift in any of the above-mentioned metrics. All of these factors are affected by the sensor material, gas interaction, operating circumstances, and so forth. To regulate these characteristics, various new technical concepts and unique materials have been developed. Chemiresistive sensors have the following characteristics: a good sensor response, a short reaction time, quick recovery, excellent selectivity, accuracy, and a low cost.

### 3.2 Factors Affecting Sensing Performance

Improved chemical sensing performance with regards to selectivity and sensitivity is in great demand, and innovative materials with high sensitivity and low limit of detection always pique the interest of researchers. This section lists the primary factors for improving the gas sensitivity and selectivity of these materials [98–100].

### 3.2.1 Morphology, Size, and Shape of the Materials

Chemiresistive sensors can be classified into three types based on their receptor, transducer, and usefulness. The receptor function is concerned with the ability of the surface to interact with the target gas. The transducer function refers to the transducer's ability to convert the signal created by the chemical interaction of the surface (work function change) into an electrical signal. The utility factor affects how effectively surface and bulk oxide granules are used for the detected response. The transducer function is highly dependent on the microstructure of the element, notably the grain size (D) and the depth of the surface space-charge layer (L). The sensor's responsiveness is substantially increased when the grain size D is 2 L. It has been established that increasing the surface area to volume ratio by declining particle size results in an exponential rise in sensor response [101].

### 3.2.2 Chemical Composition

The chemical composition is critical for understanding sensory properties as well as material qualities such as adsorption ability, catalytic activity, sensitivity, stability, and so on. Composite materials, for example, give higher catalytic activity on the surface and a richer redox reaction to attain high sensitivity as compared to pristine materials [5, 102–106].

### 3.2.3 Surface Modification

Using a noble metal or oxide materials to modify the surface is a well-known method for improving selectivity. Gold, platinum, palladium, and other noble metals have all been utilized thus far to increase the selectivity of gas sensors. It is assumed that when catalytic additives, such as Pt or Pd doped Tin Oxide ($SnO_2$) material, are exposed to hydrogen, hydrocarbons, or carbon monoxide, the metal surface first activates the reduction of the gas molecules, creating the active surface species. The active pores on the surface react to a spillover process with the charged oxygen molecules adsorbed on $SnO_2$, resulting in improved gas sensing properties. [30, 46, 107, 108].

### 3.2.4 Operating Temperature

The operating temperature is critical since the sensor's response is temperature-dependent due to the adsorption–desorption process. The various oxygen species are first adsorbed on the surface, and then the adsorption, desorption, and diffusion process occur, depending on the operating temperature. As a result, temperature modulation produces response patterns that are unique to the species in the gas mixture. This enables multivariate data from any sensor to be measured [109].

## 4 Gas Sensing Characteristics

We all know that air pollution is a major concern these days. The main causes of pollution and the deterioration of the atmosphere are toxic gases and volatile organic compounds (VOCs). Nitrogen dioxide ($NO_2$), sulphur dioxide ($SO_2$), hydrogen sulphide ($H_2S$), ammonia ($NH_3$), and other well-known hazardous gases are examples of poisonous gases, while volatile organic compounds (VOCs) include ethanol, acetone, formaldehyde, n-butanol, acetaldehyde, and methanol [110, 111]. Several methods, including mass spectrometers, gas chromatographs, flame ionization detectors, and Fourier transform infrared spectrometers, have been employed to identify various hazardous gases and VOCs. But the problems associated with these devices are they are bulky and expensive and a skilled operator is required for handling this equipment which leads to the Evaluation and utility of smart sensors for gas detection [112, 113]. Over the past years, there has been an inclination toward nano gas

sensors that can detect and discriminate various analytes. These nanosensors were designed and fabricated through the measurements of physical quantities such as resistance, capacitance, fluorescence, absorbance, luminescence, refractive index, etc. There are many sectors where these sensors are becoming inevitable such as the chemical industry, environmental monitoring, textile industry, etc. Except for sensing gases, applications of gas sensors include detection of vapors of volatile chemicals such as methanol, benzene, etc., food smell, health care, fragrances, etc. [114–116].

Toxic gases and VOCs may cause harm to the life of living organisms even at very low concentrations. There is a limit to the quantity for inhalation of various gases and beyond that limit, they are dangerous for human health, which is called a threshold limit value (TLV). For example, TLV of Nitrogen dioxide ($NO_2$) an oxidizing gas is reported to be 3 ppm, which is regarded as the maximum amount of $NO_2$allowed for repeated exposure over the course of an 8-h workday. 1,2 Exceeding this limit may culminate in adverse health effects such as irritation to the eye, fatigue, nausea and lung damage to lungs, etc. [117].In addition, Table 3 shows the limitations of hazardous gases in the environment as well as their harmful effect on human health. Figure 6 displays the different analytes as well as their origins that need to be found.
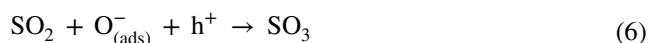
## 4.1 Oxidizing Gas

To begin with examples, exemplary SWCNTs functionalized $PdO-Co_3O_4$ HNCs nanosensors have been reported by Choi et. al which have $NO_2$measurement capacity at 100 °C with optimum sensitivity (S) of 44.11% at 20 ppm and a lower measurement limit of 1 ppm [118].

Similarly, Yang et al. [119]have reported $In_2O_3$hollow microtubes/$MoS_2$ nanoparticles produced by a layer-by-layer self-assembly process for $NO_2$ sensing. SEM and TEM images of nanostructures presented in Fig. 6a and b, prove the systemized preparation of sensing material. The authors have compared the performance of the $In_2O_3$ sensor with the $In_2O_3/MoS_2$ film sensor. This can be explained well with a optimum response, optimum linearity, promising reproducibility, and astonishing selectivity as seen in Fig. 7c–f. A response value of 371.9 toward 100 ppm $NO_2$ was observed for the $In_2O_3/MoS_2$ composite sensor, which is much higher in comparison to individual $In_2O_3$ and $MoS_2$ sensors Fig. 7f. The increased specific surface area and development of n–n heterojunction at the interface between $In_2O_3$ hollow microtubes and $MoS_2$ nanoparticles can be used to explain why the constructed sensor has improved NO2-sensing capabilities [119]. Some other such results have been summarized in Table 4.

The burning of coal, fuel oil, and other sulfur-containing materials produces sulphur dioxide ($SO_2$), one of the

primary pollutants gases in the environment [120, 121]. It is quite concerning that SO2 gas contributes to environmental contamination like acid rain, which poses a major threat to both human life and economic productivity [122, 123]. Hence, it is domineering to fabricate $SO_2$ sensors with rapid and precise detection. Zhang et al. [124] synthesized a MOFs-based gas sensor of $TiO_2/rGO$ nanocomposites for the detection of $SO_2$ gas as shown in Fig. 8a experimental platform. $TiO_2/rGO$ nanocomposites sensors are fabricated by the method of layer-by-layer self-assembly on an epoxy substrate [124]. Figure 8b illustrates the schematic of MOFs $TiO_2/rGO$ sensor. The morphological structure of $TiO_2/rGO$ is identified by SEM analysis as elicited in Fig. 8c and d. The spherical-like shape and 500 nm to 1 μm size of $TiO_2$ are tightly contacted with rGO. Figure 8e and Fig. 8f have represented the TEM image of the $TiO_2/rGO$ and $TiO_2$, respectively. The pure $TiO_2$ and $TiO_2/rGO$ are exposed to the different concentrations range 0.25–20 ppm of $SO_2$ gas sensor at room temperatures as shown in Fig. 8g, and obtained response values between 1.31 to 2.06. The MOFs $TiO_2/rGO$ was also studied for the best selectivity toward different gases, in which the $TiO_2/rGO$ have the highest response for the $SO_2$ gas as shown in Fig. 8h. Moreover, good repeatability was observed for the $SO_2$ sensing at 1, 3, and 5 ppm by $TiO_2/rGO$ sensors (Fig. 8i). The $SO_2$ gas detection sensing mechanism is shown in Fig. 8j and k, in air and $SO_2$ atmosphere. when the sensor is exposed to an $SO_2$ atmosphere $O^-$ ion adsorbed on the surface of MOFs $TiO_2$ interacts with $SO_2$ (reducing gas), and generated unstable $SO_3$, as shown in Eqs. 4, 5, 6 sensing mechanism [124]. Zhang and his group has reported UiO-66-$NH_2$ MOFs/ polyvinylidenefluoride (PVDF) nanomaterials as a sensor for $SO_2$ detections at room temperature for 50 ppm concentrations with a very good response 88.7% [125].

$$O_{2(gas)} \rightarrow O_{(ads)} + O_{(ads)} \tag{4}$$

$$O_{(ads)} \rightarrow O^-_{(ads)} + h^+ \tag{5}$$

$$SO_2 + O^-_{(ads)} + h^+ \rightarrow SO_3 \tag{6}$$

Recently, $SnO_2$ (tin oxide) are most widely explored for the gas as a sensor due to its semiconducting nature as well as having a surface for redox-active in the attendance of reducing and oxidizing gasses [126, 127]. For CO detection, $SnO_2$ based sensors are commercialized [128, 129]. However, $CO_2$ detection is still challenged because it required a high operating temperature (> 300 °C) and suffers from low sensitivity and larger response time by $SnO_2$ based sensors. Dmello et al. [130] fabricated ZIF-67 MOFs incorporated with $SnO_2$ for the better enhancement of

**Table 3** Hazardous gas concentration limits, as well as their impact on human health and property, are depicted [6, 93]

| Gas name | TLV | IDLH | Human health issues | Properties |
|---|---|---|---|---|
| Acetone | 750 ppm | 25,00 ppm | Narcosis symptoms include weak muscles, a dry mouth, fatigue, nausea, and narcosis that damages the nerves | As a reagent, colourless liquid with a pungent smell is used in laboratories to dissolve polymers |
| Formaldehyde | 0.1–0.3 ppm | 20 ppm (OSHA) | A human carcinogen causes leukemia and lung damage in humans at 6 ppm (nasopharyngeal carcinoma) | Uncolored and flammable |
| Ethanol | (1000 ppm -STEL) (ACGIH) | 3300 ppm (NIOSH) | breathing issues, irritated eyes, fatigue, and headache | Volatile, flammable, and without colour |
| $NO_2$ | 0.3 ppm (ACGIH) | 13 ppm (NIOSH) | Ozone generation, irritation of the eyes, and lung damage | It smells strong and is not flammable |
| $H_2S$ | 1-5 ppm (ACGIH) | 100 ppm (NIOSH) | Injury to the olfactory system is caused by highly reactive t with hemoglobin | It is toxic, has a rotten egg odour, and is colourless |
| $NH_3$ | 25 ppm (ACGIH) | 300 ppm (NIOSH) | Caustic and irritating, as well as dangerous to the skin, eyes, and respiratory systems of people | It is toxic, corrosive, and colourless |
| CO | 50 ppm (OSHA) and 35 ppm (NIOSH) | 1200 ppm (NIOSH) | A hemoglobin bind can cause headaches, loss of consciousness, abrupt death due to limited oxygen transport and hemoglobin bind, dizziness collapse, and nausea | Colorless, odourless, tasteless, and non-irritating |
| $H_2$ | NA | NA | Along with vomiting (the pure form is a chemical asphyxiant), dizziness, headaches, sleepiness, and nausea, other symptoms include stinging in the nose and throat | Metal smelting, petroleum extraction, glassmaking, low minimum ignition energy (0.017 mJ), nontoxic, explosive, tasteless, and explosive |

*TLV* threshold limit value, *IDLH* immediately dangerous to life or health air concentration, *OSHA* Occupational safety health administration, *NIOSH* National institute for occupational safety and health, *ACGIH* American conference of governmental industrial hygienists
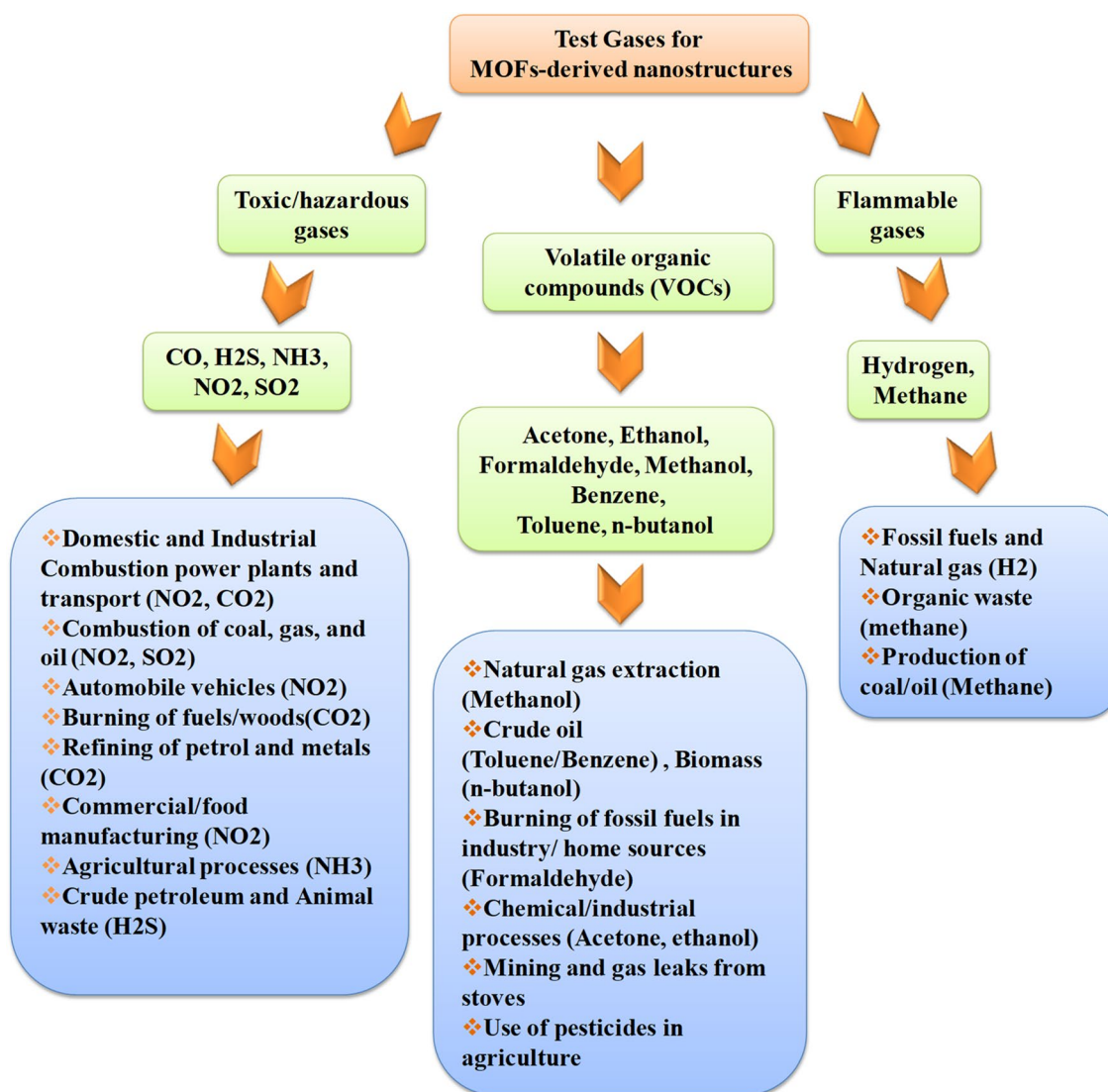
**Fig. 6** Differentiate between the different types of harmful gases and their sources of generation [6, 93]

sensor response towards the $CO_2$ gas, as shown in Fig. 9a by precipitation method for $SnO_2$ nanoparticle and ZIF-67 grow over $SnO_2$ under the solutions of $Co(NO_3)_2 \cdot 6H_2O$ and PVP. The SEM image of the $SnO_2$ and $SnO_2$@ZIF-67 are presented in Fig. 9b and Fig. 9c, respectively. The 50% $CO_2$ detection by $SnO_2$ and $SnO_2$@ZIF-67 is shown in Fig. 9f and Fig. 9g respectively, in which the performance of the $SnO_2$@ZIF-67 in response $80.6 \pm 2.2\%$ was observed at 205 °C temperature. Whereas for pure $SnO_2$ it is $8.8 \pm 2.8\%$. The $CO_2$ detection with different concentrations range 500 to 5000 ppm is elicited in Fig. 9h by sensor materials $SnO_2$ and $SnO_2$@ZIF-67. The MOFs-based sensor of $SnO_2$ also has less response and recovery times than pure $SnO_2$ as depicted in Fig. 9i. Response time surged by ~ 10 s while recovery time decreased 96 s to 25 s for 5000 ppm of $CO_2$ [130].

Ozone ($O_3$), is a strong oxidizing gas employed in a variety of essential industries, including water treatment, food processing, odour control, and medical disinfection [131, 132]. Aside from that, ozone is an essential indicator of air pollution, and ozone levels exceeding 120 ppb are harmful to human health [133]. Currently, for the detection of ozone gas MOFs based on 1 wt% $Ag/In_2O_3$ [134], a-$Ag_2WO_4$ nanorods [135], and $TiO_2$-$WO_3$ composite [136] are reported, but these sensors are not efficient in terms of low detection of concentrations, required high operating temperature, insufficient response, and high response-recovery time. Zhang et al. reported [137], that a gas sensor for the ozone detection based on MOFs $In_2O_3$ hollow microtubes decorated with ZnO nanoparticles, which is $In_2O_3$ prepared by the two steps facile solvothermal method than followed by calcination of the ZnO particle as shown in Fig. 10a. A series of $In_2O_3$/
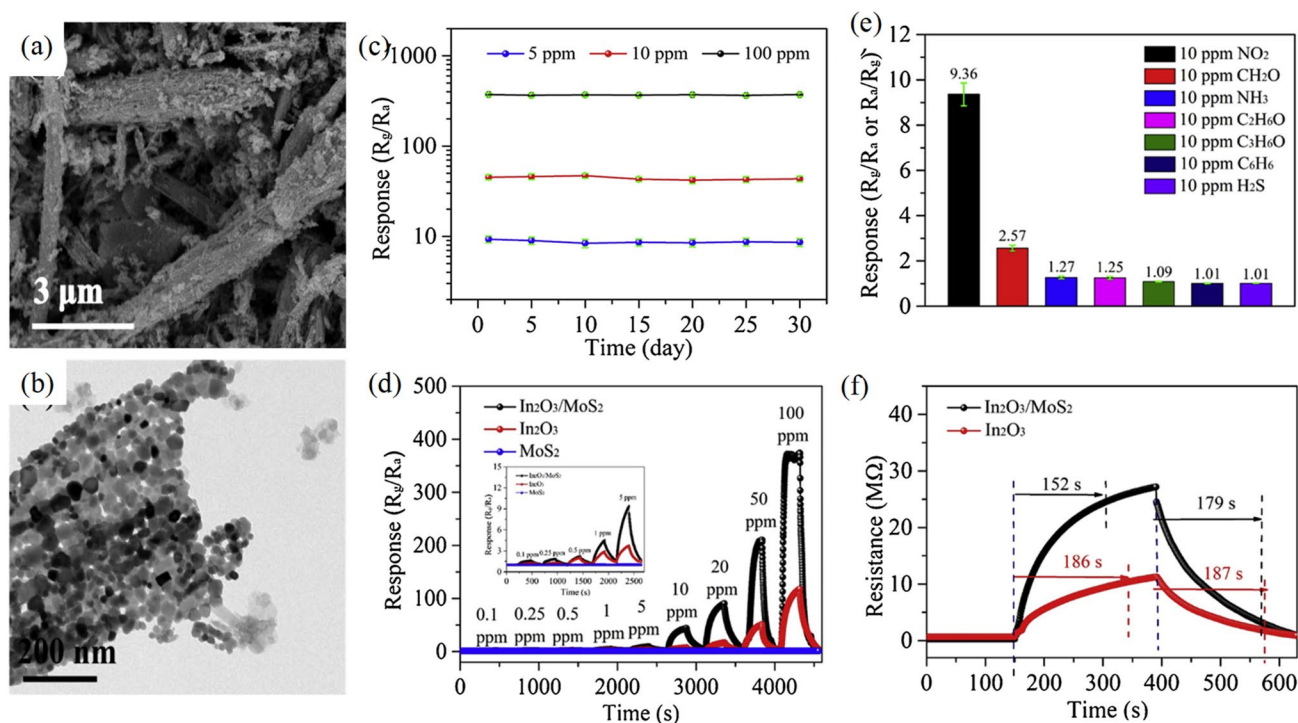
**Fig. 7** **a** Images of In2O3/MoS2 taken with a scanning electron microscope (SEM); **b** Images taken with a transmission electron microscope (TEM); **c** Long-term stability of the $In_2O_3$/MoS$_2$ composite sensor after exposure to 5, 10, and 100 ppm $NO_2$; **d** Responses of the $In_2O_3$/MoS$_2$ composite and individual $In_2O_3$ sensor toward various concentrations of $NO_2$ at 25 °C; **e** Selectivity of the [119]. *Reprinted with permission from Ref. (Yang* et al.*,2019), Copyright 2019, Elsevier*

ZnO composites prepared with various ratios of In:Zn in 1:1, 3:1, and 5:1 marked names as 1In:1Zn, 3In:1Zn, and 5In:1Zn, correspondingly. In which 3In:1Zn are the most accurate sensor found for ozone gas detections. The morphological structure of The SEM and TEM images are presented in Fig. 10. That indicates the clear decoration of ZnO NPs onto the $In_2O_3$ hollow microtubes. The 14.4 response was observed toward the $O_3$ at concentrations of 500 ppb and 26.12 response at 1 ppm concentrations of $O_3$ (Fig. 10e). Moreover, the response-recovery time is 21/42 s found for 500 ppb ozone gas as demonstrated in Fig. 10f [137].

Chlorine gas ($Cl_2$) is essential to human survival as a pungent and harmful gas. Like drinking water and swimming pools are sanitized with or include chlorine. When $Cl_2$ inhalation toxicity exceeds 30 ppm, it might cause cough and chest pain immediately [138]. However, $Cl_2$ sensor research is rare in comparison with other gas sensors and is mostly focused on semiconductor metal oxides [139–142]. For instance, nanoparticles of ZnO had been produced using a solid-state method and the gas reaction at 200 °C was only 4 to 10 ppm $Cl_2$ [143]. At ambient temperature, a CdSnO$_3$ sensor with a high sensitivity to $Cl_2$ (1338.9 to 5 ppm) was created using a hydrothermal technique. However, the recovery time is too long to be useful in practice [144]. The sensitivity of $In_2O_3$ microstructures produced

through the hydrothermal approach at a higher working temperature (300 °C) was 48.5 toward 10 ppm $Cl_2$ [145]. As a result, the growth of a $Cl_2$ gas sensor with outstanding gas performance is essential. Therefore, recently Ma et al. [146] developed MOFs-based nanostructure of $In_2O_3$ PHRs gas sensor for the detection of $Cl_2$ gas with excellent sensing response and highly selective sensor. The highly porous and hexagonal hollow structure of the $In_2O_3$ PHRs (porous hollow rods) is prepared from the MOFs precursor MIL-68 (In) as shown in Fig. 11a. Firstly, In-MOF (MIL-68 (In)) was manufactured by the facile hydrothermal process with a hexagonal shape. Then, $In_2O_3$ PHRs obtained after the calcination of MIL-68 (In) in air. The prepared $In_2O_3$ PHRs of the SEM image illustrated the smooth surface and hexagonal shape of the precursor MIL-68 (In) as depicted in Fig. 11b. The 10 to 60 μm length and 2 μm diameter of MIL-68 (In) with $In_2O_3$ PHRs microstructure is clear visibility founded. In addition to that, The TEM and HRTEM analysis of $In_2O_3$ PHRs exhibits the lattice fringers as shown in Fig. 11c at lattice spacing of 0.270 and 0.292 nm on the plane of $In_2O_3$ (321) and (222) corresponding [146]. The gas sensing mechanism for the oxidizing gas by prepared $In_2O_3$ PHRs schematic image is illustrated in Fig. 11d. The Sensor response curve of $In_2O_3$ PHRs towards the different gases of 10 ppm $Cl_2$, $NO_2$, and 100 ppm methanol, acetone,

**Table 4** Summary of work done on MOF-derived metal oxide sensors for oxidizing and reducing gases

| Analyte | Analyte type | MOF precursor | Sensor | Synthesis route | Response | Temperature | Response/Recovery | Detection limit | References |
|---|---|---|---|---|---|---|---|---|---|
| $H_2S$ | Reducing | ZIF-8u | 3D inverse opal ZnO (3DIO) with well-dispersed ZIF-8 encapsulated Pt nanoparticles | Synthesis of Pt@ZIF-8 followed by sacrificial template method for ZIF-8-derived 3DIO Pt/ZnO using PMMS(polymethyl methacrylate) and $Zn(NO_3)_2$ | Response of 11. 2 at 1 ppm of $H_2S$ | Optimal Temperature of 320 °C | 8.7 s/19.4 s | 25 ppb | [182] |
| | | CPP-3(In) micro rods | CuO/In$_2$O$_3$ heterostructure | Copper cation impregnation method to prepare $Cu^{2+}$/CPP-3(In) followed by calcination to obtain CuO/In$_2$O$_3$ | Rair/Rgas= 229.3 to 5 ppm | Low optimal operating temperature of 70 °C | 10 s/ 3600 s | 200 ppb | [183] |
| | | ZIF-67 | double-shelled hollow $Co_3O_4$/$NiCo_2O_4$ nanocages | Use of ZIF-67 as a template to form yolk-shell ZIF-67/Ni–Co nanostructure followed by its calcination | Response of about 57 for 100 ppm $H_2S$ at optimal 250 deg C. High selectivity | The optimal temperature of 250 °C | 153 s/40 s | Lowest conc. of 30 ppm reported | [184] |
| | | MIL-88 | MIL-88 derived $\gamma$-Fe$_2$O$_3$/rGO composite | Synthesis of MIL-88/rGO composites by solvothermal method followed by calcination under Ar atmosphere to yield $\gamma$-Fe$_2$O$_3$/rGO composites | A wide detection limit from 97 ppm to 2.91 ppm with a response from 520.73 to 1.47 respectively | Room temperature | – | Lowest conc. of 2.91 ppm reported | [165] |
| $Cl_2$ | Oxidizing | MIL-68 (In) | In$_2$O$_3$ porous hollow rods (PHRs) | In$_2$O$_3$ PHRs Constructed via a facile hydrothermal method and subsequent thermal treatment of In-MOFs | Outstanding gas response of 2256 for $Cl_2$ concentration 10 ppm | Optimal Temperature of 160 °C | 38 s/13 s | 3.2 ppb | [146] |
| $SO_2$ | Oxidizing | MIL125(Ti) | MOFs-derived titanium dioxide (TiO$_2$)/reduced graphene oxide (rGO) nanocomposite | Layer by layer self-assembly on an epoxy substrate | Higher response of 1.31–2.06 for SO$_2$ concentration from 0.25–20 ppm | Room temperature | Quick response/ recovery time | 250 ppb | [124] |

**Table 4** (continued)

| Analyte | Analyte type | MOF precursor | Sensor | Synthesis route | Response | Temperature | Response/Recovery | Detection limit | References |
|---|---|---|---|---|---|---|---|---|---|
| | | MFM-300 | Indium MOF (MFM-300 | Indium MOF (MFM-300), deposited on a functionalized capacitive interdigitated electrode | High sensitivity to concentrations down to 75 ppb | Room temperature | – | 5 ppb | [185] |
| | | Zr-MOF | Metal–organic framework (UiO-66-NH$_2$) on flexible electrospun polyvinylidenefluoride (PVDF) nanofibers | UiO-66-NH$_2$ is used as dielectric layer and PVDF NM provides a flexible substrateand diffusion layer at the same time | Highest sensitivity 88.7% towards 50 ppm SO | Room temperature | – | 50 ppm | [125] |
| | | Ni-Nanorodas MOF | Nanorods of nickel based MOF (Ni$_3$HHTP$_2$) | MOF (Ni$_3$HHTP$_2$) were synthesized by chemical method at 90 °C temperature | Response (13 s) and recovery time (32 s) at 875 ppb concentrations | NA | 13 s/32 s | 625 ppb | [186] |
| CO | Reducing | Sn-MOF | MOFs-derived SnO$_2$ nanoparticles-decorated MoSe$_2$ nanoflowers | SnO$_2$ nanoparticles by thermal decomposition of Sn-MOF and MoSe$_2$ nanoflowers by solvothermal route followed by SnO$_2$/MoSe$_2$ nanocomposite through a dissolution of both SnO$_2$ and MoSe$_2$ in DI water followed by drying | Response % of 12.21 for 500 ppm CO | Room temperature | 20 s/ 16 s | Lowest conc. of 1 ppm reported | [187] |
| NH$_3$ | Reducing | ZIF-8 | ZIF-8-derived zinc oxide (ZnO)/reduced graphene oxide (rGO) nanocomposite | Synthesis of ZIF-8 and ZIF-8 derived ZnO followed by layered self-assembly method for ZIF-8 derived ZnO/rGO nanocomposite | Response of 6.46 for 30 ppm NH$_3$ | Room temperature (25 °C) | 50 s/25 s | 0.5 ppm | [180] |

**Table 4** (continued)

| Analyte | Analyte type | MOF precursor | Sensor | Synthesis route | Response | Temperature | Response/Recovery | Detection limit | References |
|---|---|---|---|---|---|---|---|---|---|
| $NO_2$ | Oxidizing | ZIF-67 | ZIF-67 Derived MWCNTS | ZIF-67-Co was introduced into the stacked MWCNT sheets in a controlled amount via a facile drop-casting method | $R/R_0 = 1\%$ at 5 ppm | Room temp | – | 0.1 ppm | [188] |
| | | ZIF-67 | Co, N-doped hollow carbon nanocages ($WS_2$-Co-N-HCNCs) | $WS_2$ precursors are assembled in the surface cavity of the Co-based zeolite imidazole framework (ZIF-67) and subsequent pyrolysis produced $WS_2$-Co-N-HCNCs | $R/R_{gas} = 18\%$ @ 1 ppm | Room temp | – | 100 ppb | [87] |
| $CO_2$ | Oxidizing | ZIF 67 | Co-imidazole framework (ZIF67) over $SnO_2$, $SnO_2$@ZIF-67 | Precipitation method | Response of $16.5 \pm 2.1\%$ for 5000 ppm CO2 | 205 °C | 10 s/ 22 s | 5000 ppm | [130] |
| | | ZIF-8 | ZIF-8-based BiMW sensor | Self-assembly of a transparent film of zeolitic imidazolate framework-8 (ZIF-8) nanoparticles | Repeatability with an RSD <2% and a response time of only a few seconds | Room temp | – | 3130 ppm at room temperature and 774 ppm at 278 K | [189] |
| Ozone | Oxidizing | $In_2O_3$ | $In_2O_3$/ZnO composite | two-step solvothermal the method followed by calcination | $R_g/R_a = 26.12$ @ 1 ppm ozone | 150 °C | 21 s/ 42 s | 25 ppb | [137] |
| Oxygen | Oxidizing | MIL-100(In) | [MIL-100(In)$\supset$Tb$^{3+}$] | Post functionalization of MIL-100(In) with terbium ions | High oxygen sensitivity(KSV =7.59) and shorter response/ recovery time (6 and 53 s) t | – | 6 s/ 53 s | – | [190] |
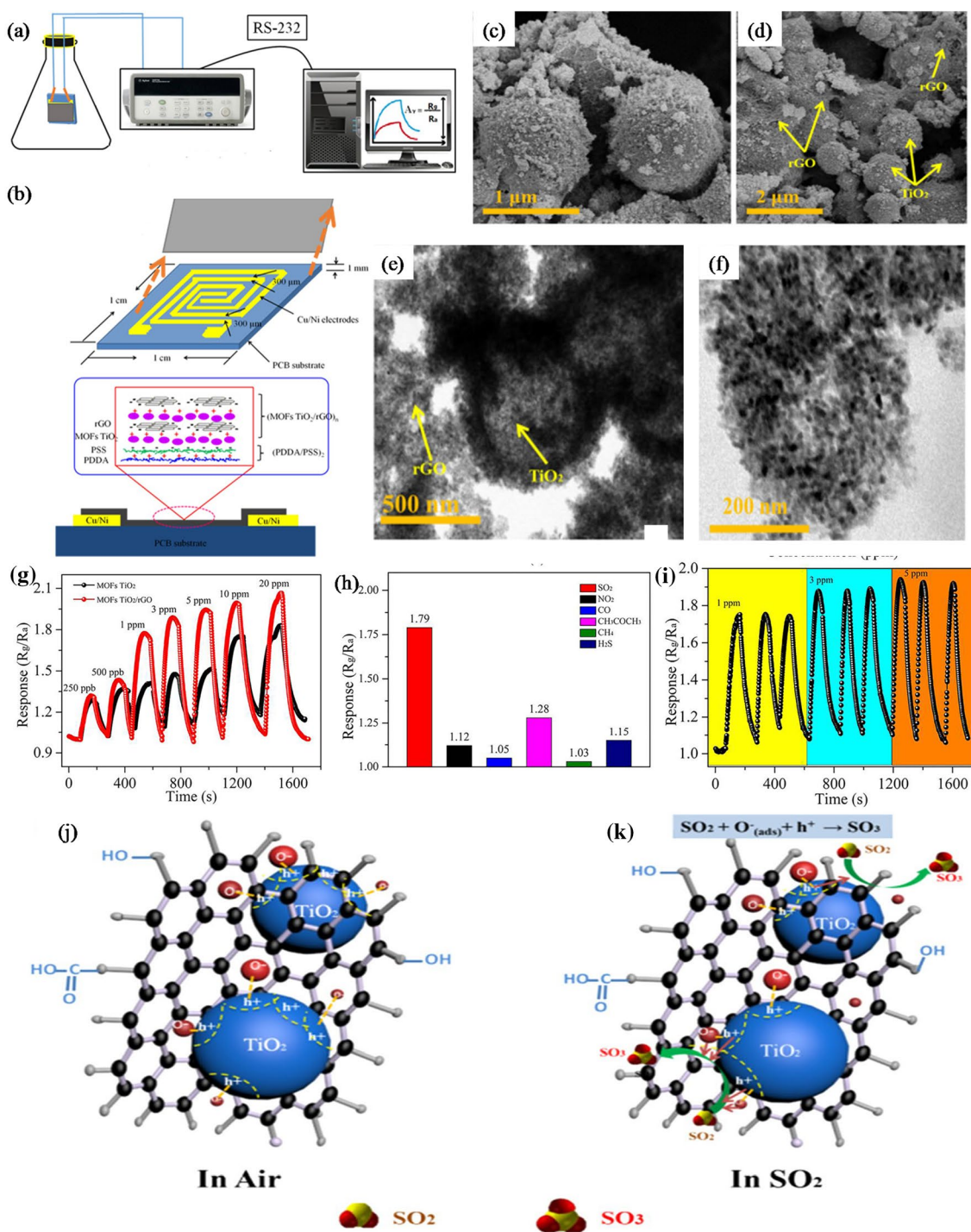
**Fig. 8** **a** SO$_2$ sensing experiment platform, **b** schematic of the MOFs-derived TiO$_2$/rGO Sensor, SEM pictures of **c** MOFs TiO$_2$, **d** MOFs TiO$_2$/rGO, **e,f** MOFs TiO$_2$/rGO TEM micrograph, **g** TiO$_2$, rGO, and MOFs TiO$_2$/rGO sensor responses at varied SO$_2$ concentrations **h** MOFs TiO$_2$/rGO selectivity for 1 ppm of different gas species, **i** Repeatability for SO$_2$ concentrations of 1, 3, and 5 ppm Schematic of the MOFs TiO$_2$/rGO sensor's sensing mechanism **j** in air and **k** in SO$_2$ gas [124]. Reprinted with permission from Ref. (Zhang group), Copyright 2019, Springers

ammonia, ethanol, and formaldehyde are experiments carried out at 160 °C as demonstrated in Fig. 11f. This sensor is highly selective for oxidizing gas as compared to reducing gas. Moreover, Fig. 11g and h elicit the response of the In$_2$O$_3$ PHRs for 10 ppm Cl$_2$ with different operating temperatures, with 160 °C to be found a most optimum temperature with
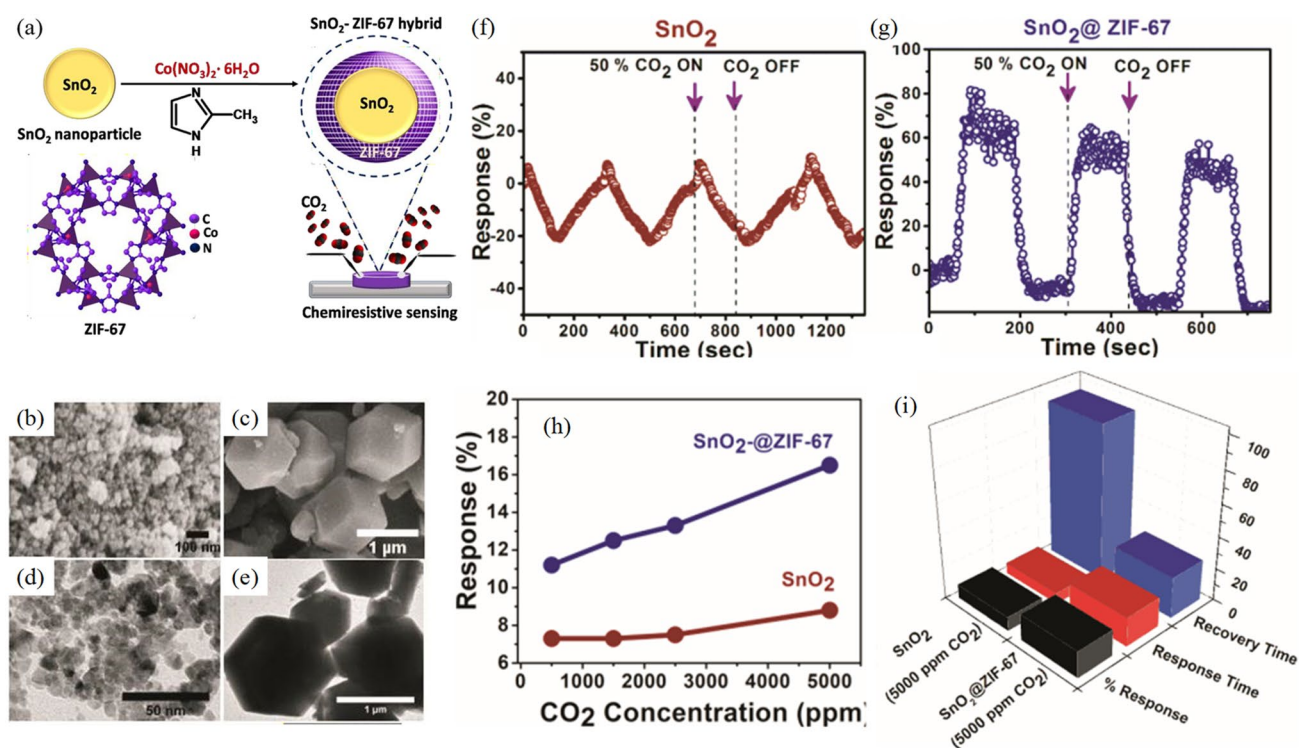
**Fig. 9 a** Schematic depiction of SnO$_2$@ZIF-67 formation for CO$_2$ detections; **b, c** SEM pictures of SnO$_2$ and MOFs SnO$_2$@ZIF-67 materials, respectively; **d, e** SEM images of SnO$_2$ and SnO$_2$@ZIF-67 materials, respectively; **f, g** SnO2 and SnO2@ZIF-67 materials, respectively; **h** Sensor SnO2 and SnO$_2$@ZIF-67 response for differ-ent CO$_2$ concentrations ranging from 500 to 5000 ppm; **i** Comparison of SnO$_2$ and SnO$_2$@ZIF-67 sensors for (percent response, response time, and recovery time of the 5000 ppm CO$_2$ concentration) [130]. *Reprinted with permission from Ref. (Dmello* et al.*), Copyright 2018, Wiley Online Library*

the response of 2256. In addition, fast response/recovery for 10 ppm Cl$_2$ at 160 °C Temperature obtained 38/13 s, respectively [146].

## 4.2 Reducing Gas

Chemiresistive gas sensors currently face challenges in the form of parts per billion level sensitivity, long-term stability, and accurate cross selectivity. MOF-based chemiresistive sensors have proved promising to overcome these obstacles owing to their very high surface areas [33]. One of the first MOF-based chemiresistive sensors was studied by Chen's group, where ZIF-67 (Co(mim)$_2$; mim = 2-methylimida-zolate) was used to sense formaldehyde (a reducing gas) of about 5 ppm concentration under an optimal temperature of operation is 150 °C. The MOF-based sensor unveiled high response and good selectivity [147]. They created a formal-dehyde sensor called the Co-based zeolite imidazole frame-work (ZIF-67), which is made of Co ions and methylimida-zole linkers (Fig. 12a). Be aware that sick building syndrome can result from low formaldehyde ppm levels [148]. The sensors had been worked at 150 °C to transduce the sensing signals since ZIF-67's electronic band gap (1.98 eV) and low electron orbital overlap prevent it from being conductive at ambient temperature [149]. Importantly, the sensors dis-played a detectable response of 1.8 and a detection limit of 5 ppm (Fig. 12b), which was explained by the enormous sur-face area (1800 m$^2$/g) of ZIF-67. Additionally, up to 70% rel-ative humidity (RH), the sensor performance was independ-ent. The sensing abilities of cobaltimidazole frameworks (Co[(IM)$_2$]n) produced by combining imidazole and cobalt (II) acetate were also studied by the same group (Fig. 12c) [150]. At an operating temperature of 75 °C, the Co[(IM)$_2$]$_n$ demonstrated selective sensing characteristics toward tri-methylamine (R$_{gas}$/R$_{air}$ = 2 to 2 ppm) (Fig. 12d). Similar to formaldehyde sensors built on the ZIF-67 standard, the sen-sors showed a steady response across a variety of humid-ity levels. Zr$_6$(O)$_4$(OH)$_4$(1,4-benzenedicarboxylate-NH$_2$)$_6$, NH$_2$-UiO-66, an amine-functionalized Zr-based MOF, also shown chemiresistive sensing capabilities to sulphur dioxide (SO$_2$) at 150 °C in an Ar environment (Fig. 12e) [151].The resistance of NH$_2$-UiO-66 (band gap = 2.75 eV) [152] fol-lowing SO$_2$ adsorption decreases (jDR/R0j = 21.6 percent to 10 ppm of SO$_2$) due to a charge transfer coupling caused by the high acidity of SO$_2$ (Fig. 12f) [33].

MOF-based metal-oxide-based chemiresistive analyte sensors have gathered great attention in recent years for reducing gases like Acetone, Ethanol, sulfur dioxide, carbon
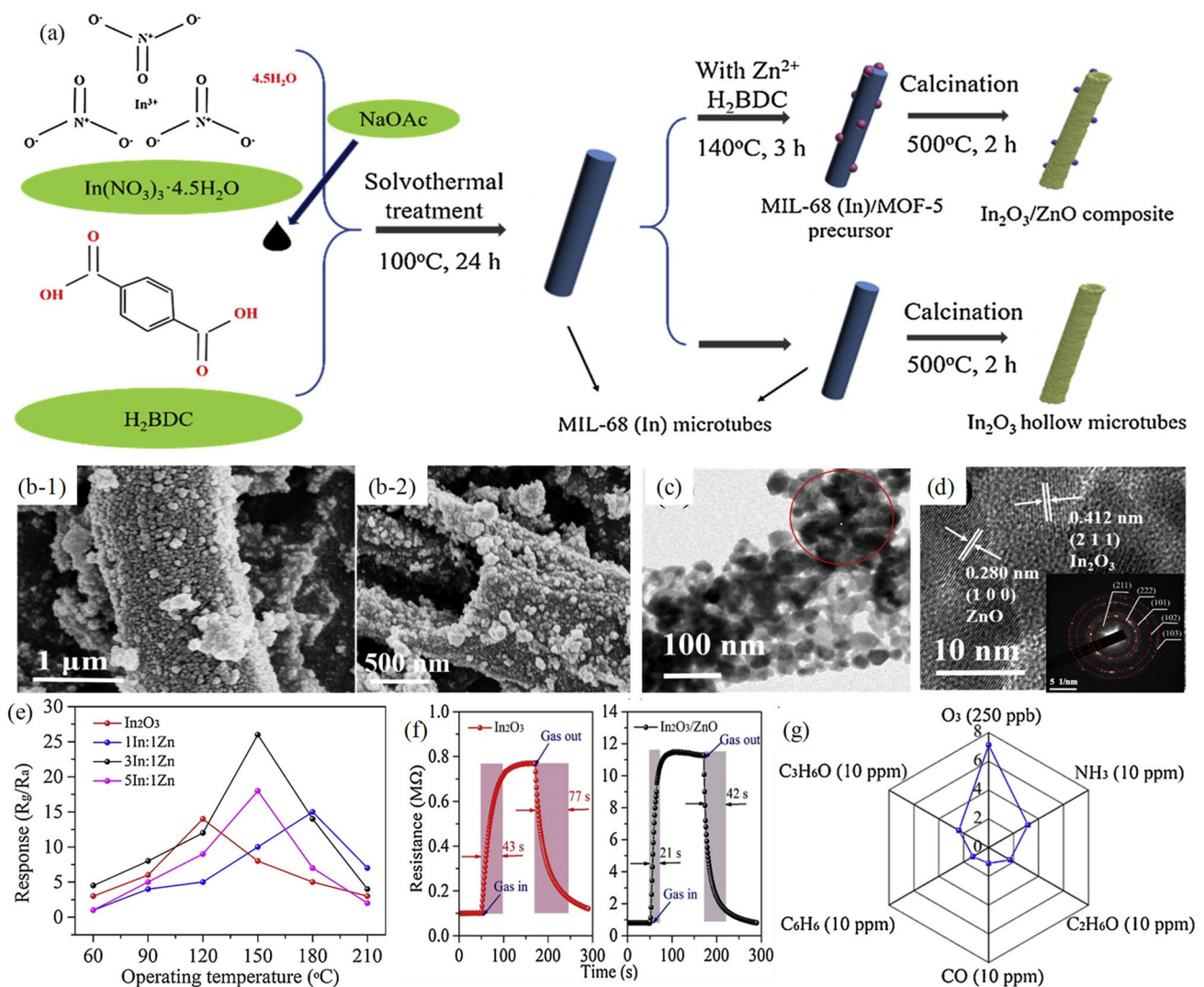
**Fig. 10** **a** A schematic showing how In$_2$O$_3$ hollow microtubes and In$_2$O$_3$/ZnO composite is made; **b** SEM images of the 3:1 In:Zn produced In$_2$O$_3$/ZnO composite; **c** TEM images of the composite; **d** HRTEM and SAED (inset) images of the composite; **e** Response-recovery curves of In$_2$O$_3$ and 3In:1Zn sensor toward 500 ppb ozone gas; **f** Response-recovery curves of In$_2$O$_3$ and 3In:1Zn sensor toward different interfering gases at 150 °C; **g** Selectivity of the 3In:1Zn sensor against different interfering gases at 60–210 °C; [137]. *Reprinted with permission from Ref. (Zhang* et al.*), Copyright 2019, Elsevier*

monoxide, hydrogen, hydrogen sulfide, ammonia, etc. Since MOFs have been reported to be unstable at high temperatures, metal oxide nanostructures derived from MOFs, which retain the unique properties of MOFs (like high porosity), have proved to be exceptional in improving the gas sensing recital of the conventional metal oxide-based sensors [153, 154].

Yuan and group have synthesized oxygen vacancies rich ZnO nanosheet sensors which were prepared by chip-level pyrolysis of zeolitic imidazolate framework. The sensors displayed ppb level carbon monoxide sensing along with other VOCs like 1,3 butadiene, toluene, and tetrachloroethylene. The presence of oxygen vacancies facilitated increased chemisorption of oxygen species which in turn led to surged

gas sensing properties for the detection of 447 ppb of CO and 100 ppb of VOCs at 300 °C. The curve of the dynamic response for both variable CO and VOC concentrations can be seen in Fig. 13b and c [155].

Recently, MOF-derived metal oxide-based sensors have also been accompanied by Metal oxide semiconductors (MOS) coated MOFs, also represented as MOS@MOFs. These involve putting a MOF on the MOS surface with pores smaller than the interfering gas. This control of the pore size provides special size-selective gas sensing properties [154]. For liquefied petroleum gas (LPG) sensing, many studies show the effectiveness of metal oxides-based sensors [156, 157]. However, MOF-derived metal oxides might offer those extra benefits of high porosity and surface area which may
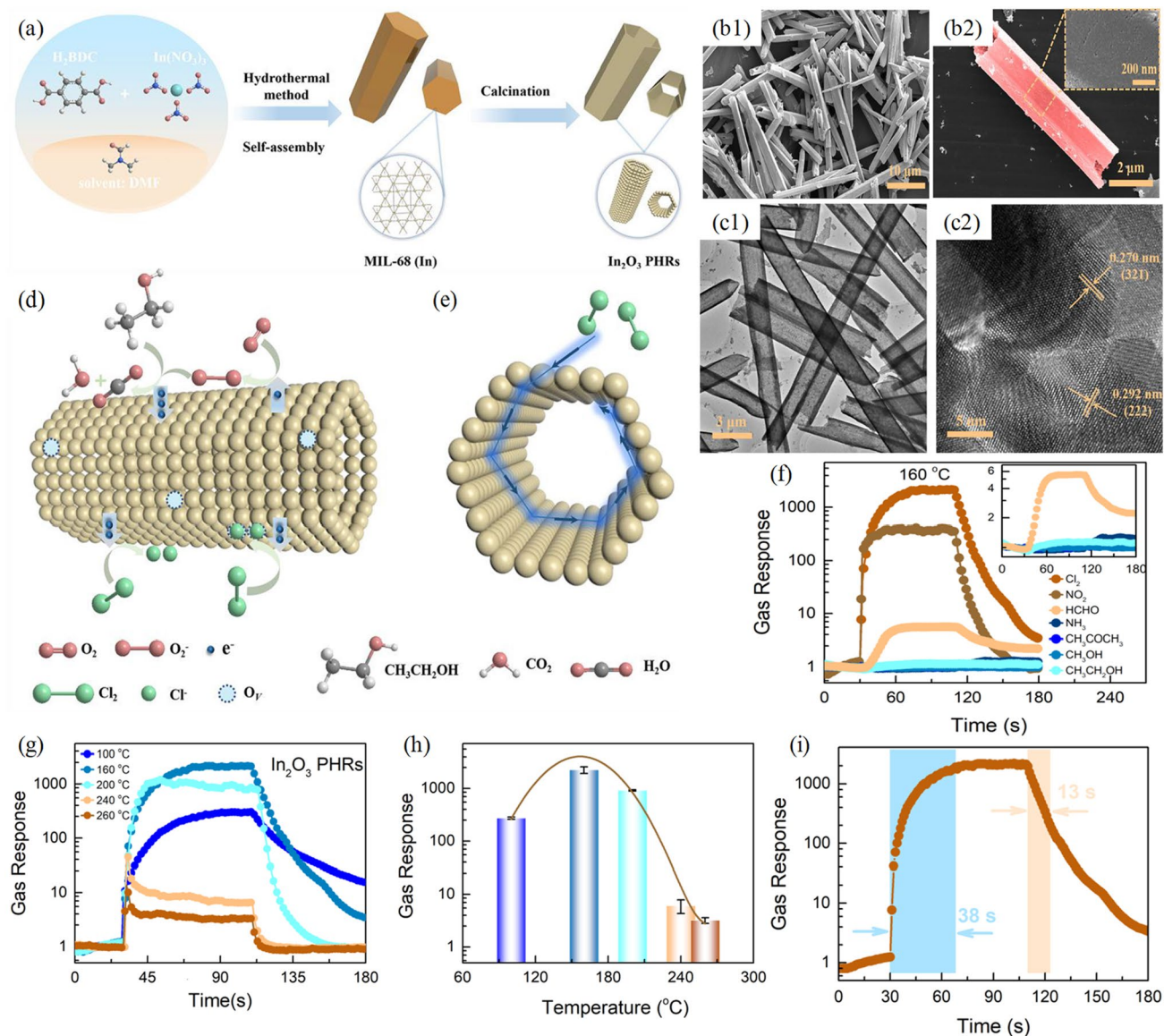
**Fig. 11** **a** Schematic illustration for the preparation of In$_2$O$_3$ PHRs; **b** SEM images of In$_2$O$_3$ PHRs; **c** TEM & HRTEM image of the In$_2$O$_3$ PHRs; **d**, **e** The illustration of the sensing mechanism of the In$_2$O$_3$ PHRs sensor; **f** Response curve of the In$_2$O$_3$ PHRs for various gases at 160 °C temperature; **g**, **h** Response of the In$_2$O$_3$ PHRs for the 10 ppm Cl$_2$ operating temperature ranging 100–260 °C; **i** illustrated the response and recovery time curve of In$_2$O$_3$ PHRs for 10 ppm Cl$_2$ gas [146]. *Reprinted with permission from Ref. (Ma et al.), Copyright 2020, Elsevier*

aid in ppb level detection thereby proving to be promising from a safety point of view.

Recently Khudiar et. al. have claimed regulated sensing activity of ZnO by the use of the zeolithicimodazole-based metal–organic framework family (ZIF-8). The author compared the sensing performance of ZnO for hydrogen and benzene gases with or without ZIF-8. It was claimed that the ZIF-8 coating functions as a molecular sieve, preventing the bigger benzene molecules from diffusing through the pores to the ZnO surface in comparison to the smaller H2 molecules [158]. Lv et al. [159], reported the most highly

selective gas ZnO@ZIF-8 MOFs-based gas sensor toward the H$_2$. In which, nanosize ZnO particles are prepared by the precipitation method. Then over the ZnO NPs, ZnO NPs' surface was where the ZIF-8 film was produced by the method of hydrothermal up to 20 h. The thickness of the film core–shell structure cannot form sufficient within 4 h but after 20 h, the NIF-8 form 130 nm thick film over the ZnO nanoparticles as shown in Fig. 14a, and the morphological SEM and TEM images are shown In Fig. 14b and c. The 20-ZnO@ZIF-8 sensor for the H$_2$ gas best response is obtained as demonstrated in Fig. 14e and f.
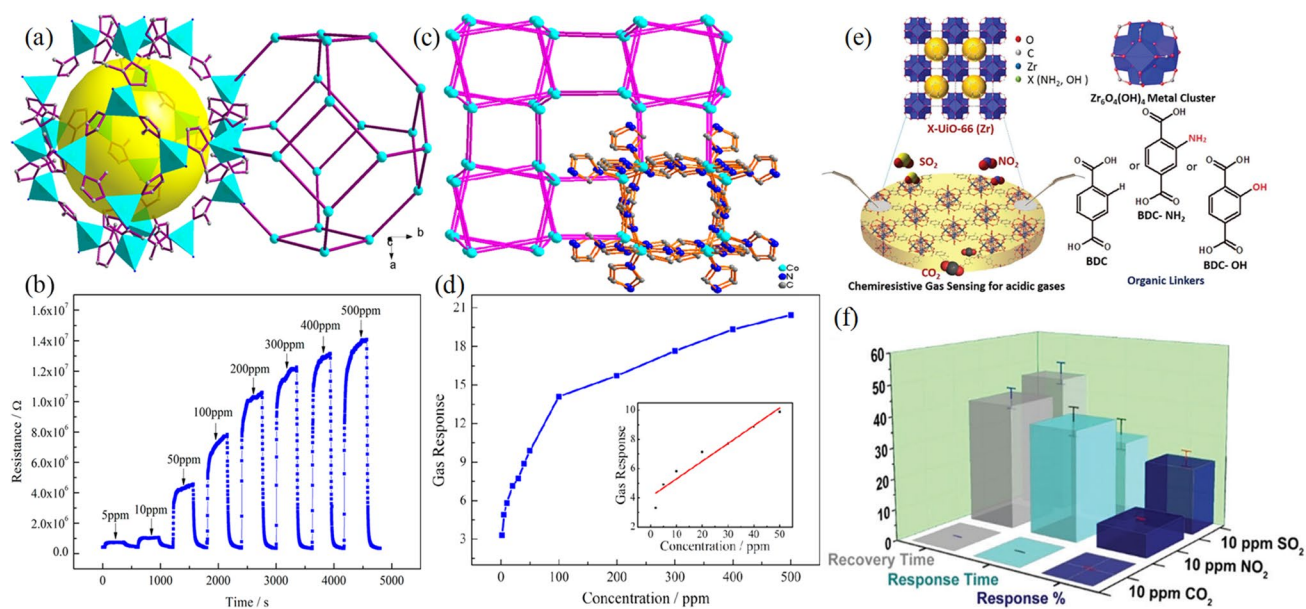
**Fig. 12** **a** The ZIF-67 SOD structure; **b** The dynamic resistance changes of ZIF-67 to formaldehyde concentrations of 5–500 ppm at 150 °C; **c** The crystal structure of [Co(IM)$_2$]n; **d** The response to trimethylamine concentration (with an inset showing the response to 2–50 ppm) at 75 °C; **e** The schematic illustration of NH$_2$-UiO-66; and **f** NH$_2$-UiO-66's gas-sensing properties for 10 ppm SO$_2$, NO$_2$, and CO$_2$ at 150 °C [33, 147]. *Reprinted with permission from Ref. (Koo et al.), Copyright 2019, Elsevier*

A kind of colourless, toxic gas called hydrogen sulphide (H$_2$S) is created when organic matter containing sulphur breaks down when sulphate is reduced by microorganisms, when crude oil is refined, and during other processes [160–162]. Olfactory hyposensitization prevents humans from recognizing harmful H$_2$S concentrations in time, despite the fact that H$_2$S emits the unpleasant smell of "rotten eggs". While this is happening, it has a deleterious effect on the neurological system and can cause unconsciousness [163, 164]. As a result of the high risk, the detection of H$_2$S becomes important for both industrial production and daily life because of the high risk. Zhang et al. [165], synthesized MOFs based γ-Fe$_2$O$_3$/rGO sensor for the detection of H$_2$S gas at room temperature with great response highly selective toward H$_2$S gas. The γ-Fe$_2$O$_3$/sensor was fabricated from MIL-88/rGO, in which the MIL-88 was synthesized by solvothermal method [166] followed by calculations under the Ar atmosphere to yield γ-Fe$_2$O$_3$/rGO.The different weights of rGO 10, 20, and 30 mg were utilized to form different composites and designated as γ-Fe$_2$O$_3$/rGO-10, γ-Fe$_2$O$_3$/rGO-20, and γ-Fe$_2$O$_3$/rGO-30 as shown in Fig. 15a. The most excellent sensor γ-Fe$_2$O$_3$/rGO-20 noted against H$_2$S gas at room temperature. The morphological SEM image of γ-Fe$_2$O$_3$/rGO-20 in Fig. 15b shows the size of the γ-Fe$_2$O$_3$ octahedron. Moreover, the TEM analysis observed for γ-Fe$_2$O$_3$/rGO-20 internal details as shown in Fig. 15c uniform γ-Fe$_2$O$_3$ octahedrons distributed on the almost transparent rGO. The great sensitivity toward H$_2$S gas by γ-Fe$_2$O$_3$/rGO composites was observed ($R_{air}/R_{gas}$ = 520.73, 97 ppm) as demonstrated in Fig. 15d as well as the minimum detection limit is 2.91 ppm ($R_{air}/R_{gas}$ = 1.47). In addition to that, the γ-Fe$_2$O$_3$/rGO-20 indicatesa high response (S = 520.73) to 97 ppm H$_2$S and a small response to other gases HCHO, SO$_2$, NO, CHCl$_3$, and NH$_3$ as elicited in Fig. 15f. The sensing mechanism for the H$_2$S gas by the γ-Fe$_2$O$_3$/rGO is illustrated in Fig. 15g [165]. Another sensor was also reported for the H$_2$S detection, but cannot sufficiently give a high response, required high operating temperature, and less response [166–171].

One of the main air pollutants is ammonia (NH$_3$) [172]. Ammonia gas at a particular concentration can harm the respiratory system and lead to tightness in the chest and breathing problems. It is crucial to set up a high-performance sensor in order to detect NH$_3$ concentrations accurately and quickly [173–175]. Recent research demonstrates that nano-ZnO is a highly effective material for making gas sensors since it has excellent gas sensitivity for NH$_3$ [176]. The drawbacks of the pure ZnO gas sensor are excessive energy use and weak reaction sensitivity [177]. In order to detect ethanol gas, Ren developed ZnO@ZIF-8 core–shell microspheres, and the sensor's response was significantly greater than that of pure hollow ZnO microspheres [178]. ZIF-8/MWCNT/AgNPs nanocomposite was developed by Jafari et al. for the detection of VOCs gas, and the sensor has shown a high sensing response and a quick reaction/recovery time [179]. Wang et al. [180] reported MOFs-based high-performance gas sensors at room temperature for the NH$_3$(ammonia) detection. The sensor was fabricated by Metal organic framework-based Zinc oxide(ZnO)/reduced

**Fig. 13** **a** After being exposed to 447 ppb CO, the sensors' gas sensing response (solid lines) and response time (dotted lines) were plotted against operating temperature. **b** The dynamic response of sensors with varied oxygen vacancy amounts to varying CO concentrations at 300 °C within 30 s. **c** Dynamic response to varying VOC concentrations at 300 °C within 30 s of the oxygen vacancy-rich sensor (blue curve). 1,3-butadiene, toluene, and tetrachloroethylene make up 100 ppb, 100 ppb, and 100 ppb, respectively, of the VOC mixture. Also exhibited is the sensor's reaction to 100 ppb VOCs without any oxygen vacancies (red curve). The linear fitting of the vacancy-rich sensor's response to varying VOC mixture concentrations is shown in the inset. **d** The oxygen vacancy-rich sensor's cyclic sensing capability for 100 ppb VOCs at 300 °C. **e** Gas sensor mechanism schematic diagram. The purple spheres in **e** represent oxygen vacancies, therefore take note of that **f, g** After calcination at a heating rate of 10 °C min$^{-1}$, SEM pictures of the active layer were taken [155]. *Reprinted with permission from Ref. (Yuan* et al.*), Copyright 2019, John Wiley and Sons* (Color figure online)
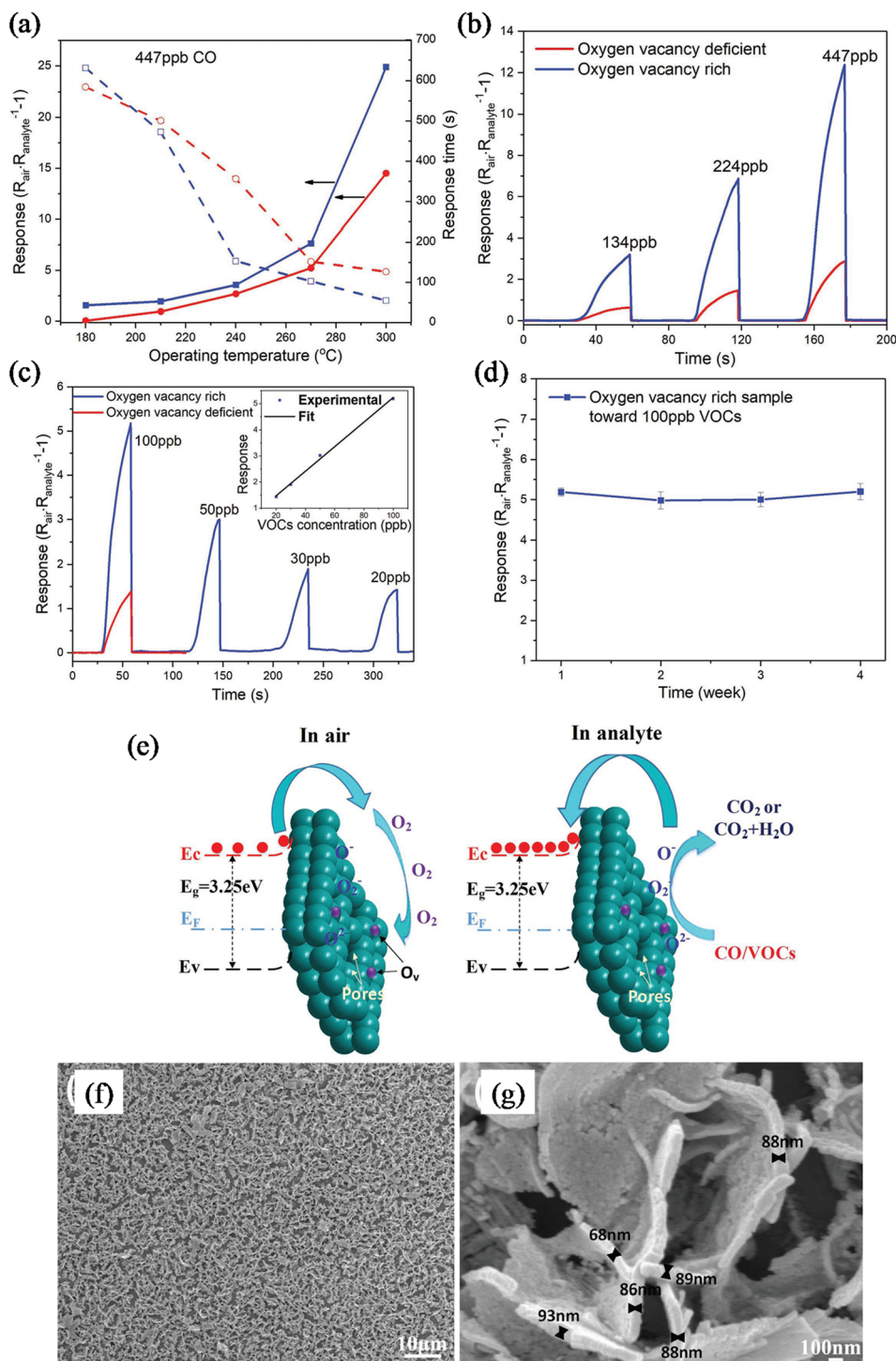


graphene oxide (rGO). By using the layered self-assembly method, a ZIF8-ZnO/rGO multilayer nanocomposite film was created. The cubic-shaped SEM image of the ZIF8-ZnO/rGO composites is shown in Fig. 16a. Additionally, the visible lattice spacing at 0.248 nm in the crystal plane of ZIF8-ZnO/rGO and the TEM study of the microstructure, as shown in Fig. 16b, are used to further analyze the microstructure. The ZIF8-ZnO/

rGO sensor's technique for detecting $NH_3$ gas is depicted in Fig. 16d. Airborne oxygen that is already present is adsorbently converted to $O_2$ on the sensor's surface (ads). Then, as shown in the reaction Eqs. 7 and 8, $O_2$(ads) capture the electrons from the surface of ZIF8-ZnO and become $O^-_2$(ads) and increase the resistance in the composites film. The ZIF8-ZnO/rGO film is exposed to $NH_3$, and the adsorbed $O^-_2$(ads) starts to react with
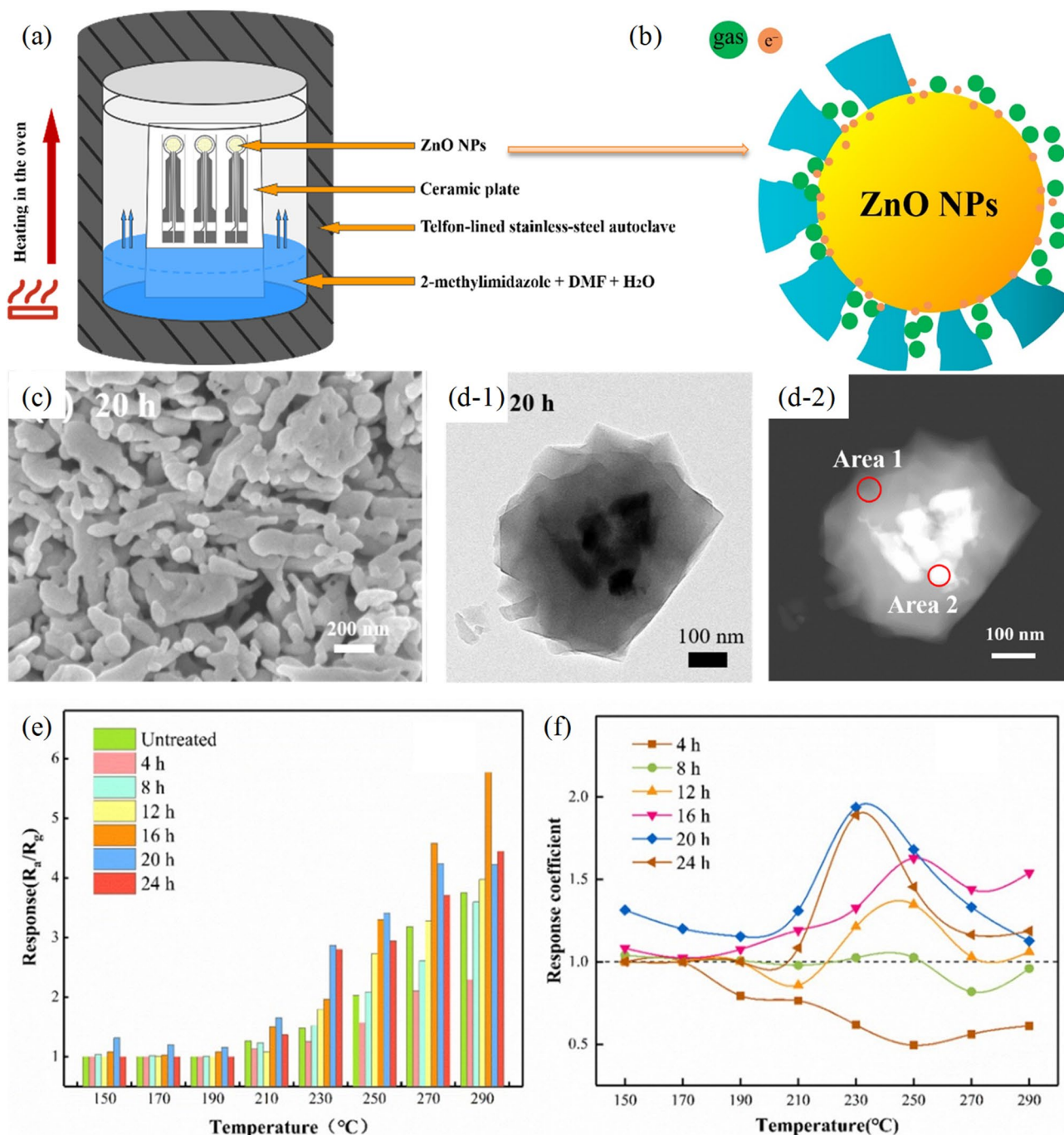
**Fig. 14** **a** Schematic diagram of hydrothermal synthesis; **b** Graphical representation of the ZnO@ZIF-8 composite with incomplete coating; **c** SEM of ZnO@ZIF-8 gas sensors after 20 h; **d** TEM image of 20-ZnO@ZIF-8; **e**, **f** The responses and response coefficients of the gas 1000 ppm $H_2$ sensor [159]

$NH_3$ as shown in Formula 9. Moreover, the highly ultra-thin drop present in the rGO nanosheets is essential to the improvement of the specific surface area of the ZIF8-ZnO/rGO sensor, due to its high surface area it greatly allows to adsorb $NH_3$ molecule and rGO also improve the conductivity of the sensor, which significantly allows the sensor's electrical conduction following the adsorption of ammonia molecules [181]. The

rGO, ZIF8-ZnO, and ZIF8-ZnO/rGO were measured over a range of 0.5–30 ppm of $NH_3$ as demonstrated in Fig. 16e. The highest response was observed by the ZIF8-ZnO/rGO ($R_{air}/R_{gas}=6.46$, 30 ppm) for the $NH_3$ gas. However, the recovery and response time of the sensor are illustrated in Fig. 16f for the 10 ppm $NH_3$ detection by three different sensors, among ZIF8-ZnO/rGO to be found response/recovery time 50 s/ 25 s,
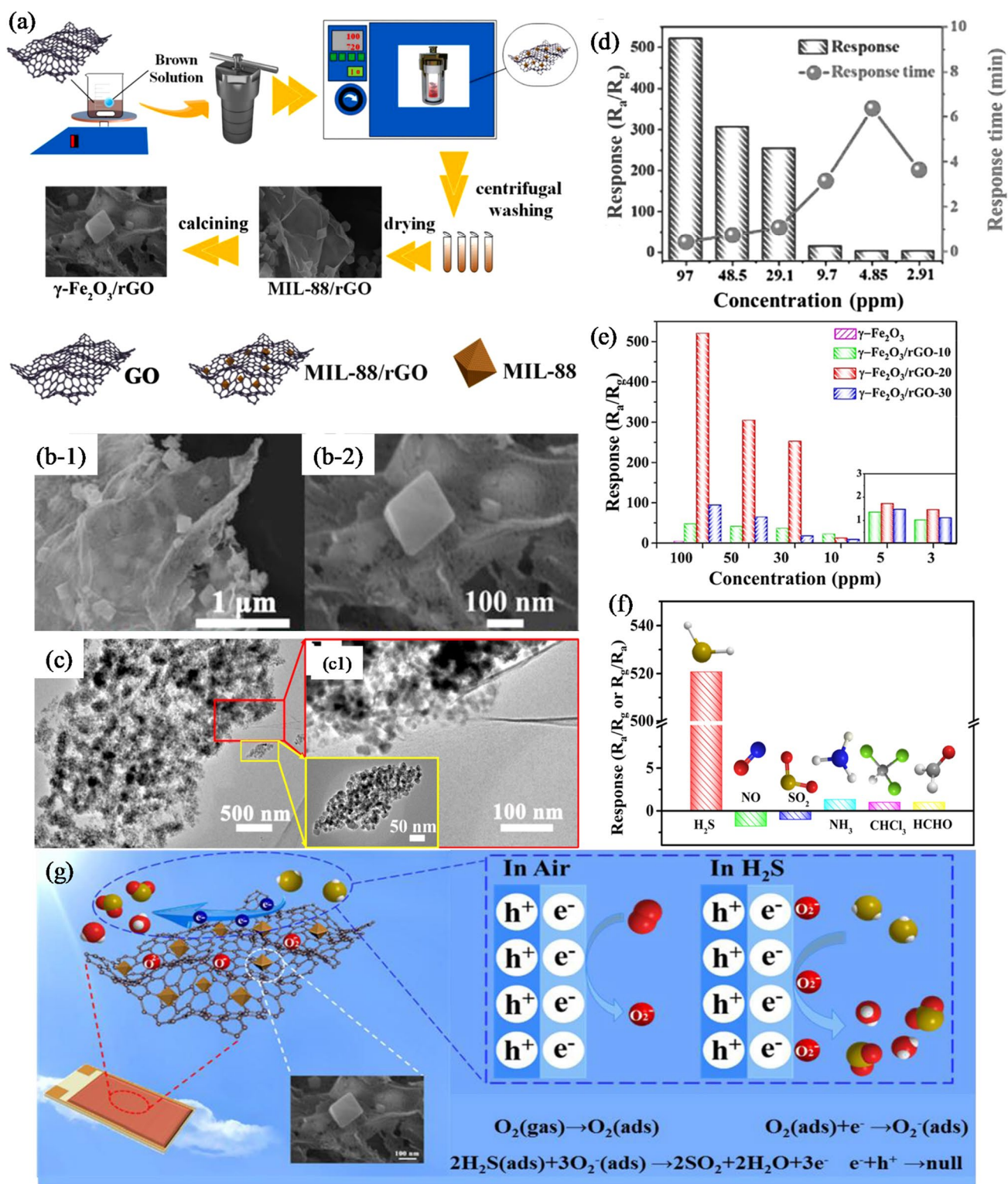
**Fig. 15 a** A schematic diagram illustrating how the -Fe$_2$O$_3$/rGO composites were made; **b** SEM images of γ-Fe$_2$O$_3$/rGO-20 composites; **c** TEM images of the γ-Fe$_2$O$_3$/rGO-20 composites; **d** Response and Response time for the H$_2$S gas at room temperature by sensor γ-Fe$_2$O$_3$/rGO-20 composites; **e** Response of the γ-Fe$_2$O$_3$/rGO composites toward the Different concentrations of the H$_2$S gas at room temperature; **f** sensing responses of the -Fe$_2$O$_3$/rGO-20 composite sensor to 97 ppm of various gases, such as H$_2$S, NO, SO$_2$, NH$_3$, and CHCl$_3$ at 50 ppm; **g** Schematic representation of the -Fe$_2$O$_3$/rGO sensor device for H$_2$S detection [165]. *Reprinted with permission from Ref. (Zhang* et al.*), Copyright 2020, Elsevier*
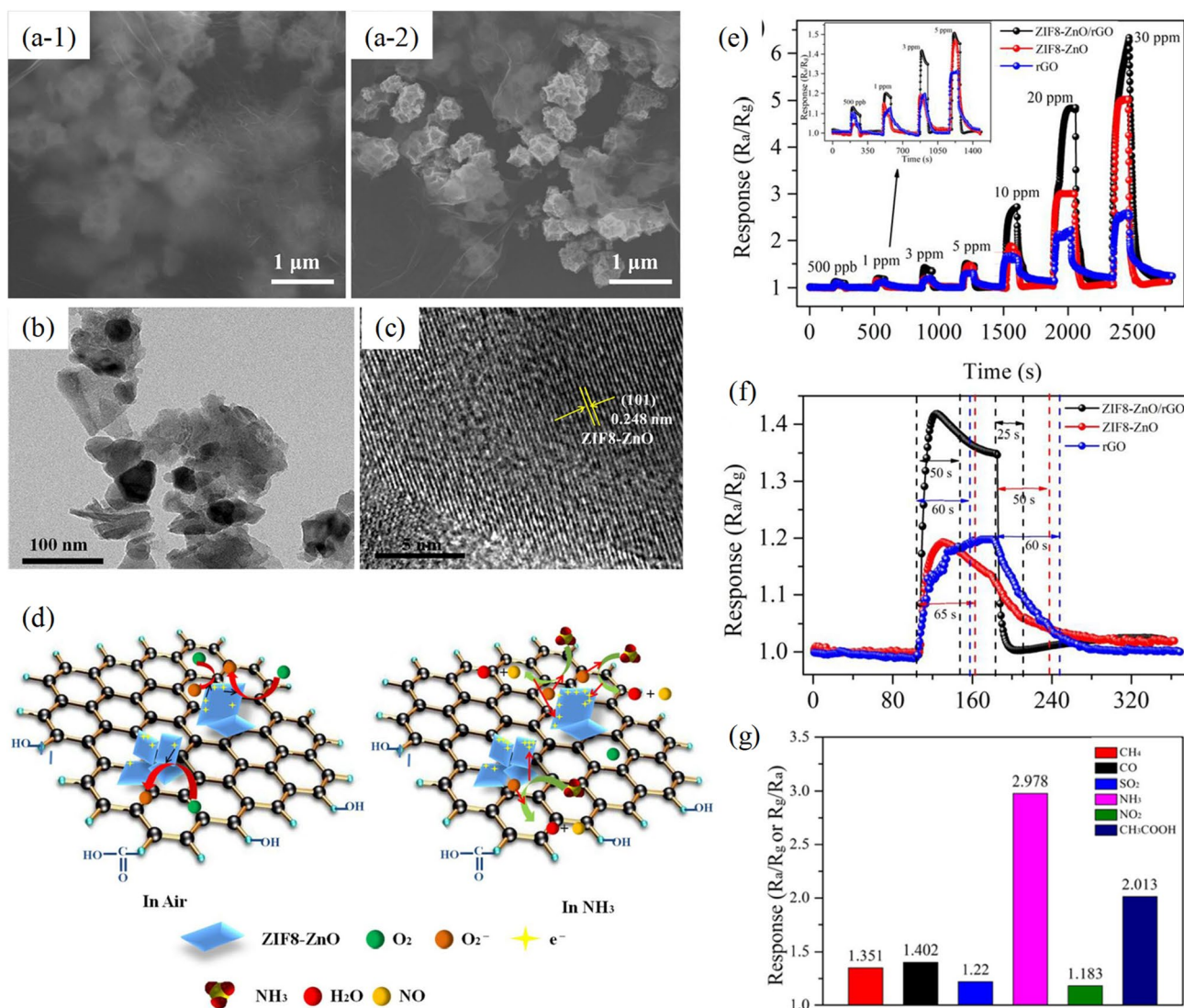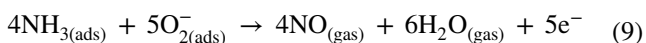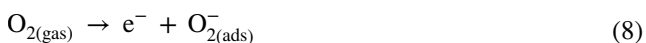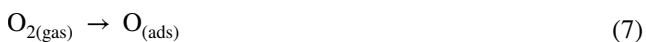
**Fig. 16 a** SEM images of ZIF8-ZnO/rGO composites; **b** A TEM image of ZIF8-ZnO/rGO; **c** HRTEM images of ZIF8-ZnO/rGO; **d** A schematic showing the ZIF8-ZnO/rGO sensor's sensing process in both air and NH3; **e** The responses of ZIF8-ZnO, rGO, and ZIF8-ZnO/rGO sensors to various concentrations of NH3; **f** The responses and recovery times of ZIF8-ZnO, rGO, and ZIF8-ZnO/rGO sensors to 10 ppm NH3; and **g** The selectivity of the ZIF8-ZnO/rGO film sensor for 10 ppm of various gas species [180]. *Reprinted with permission from Ref. (Wang* et al.*), Copyright 2020, Springer Nature*

respectively. In addition, the outcome shows the ZIF8-ZnO/rGO sensor to $NH_3$ has the optimum response from the different kinds of gases ($NO_2$, CO, $CH_3COOH$, $CH_4$, and $SO_2$) as depicted in Fig. 16g [180].

$$O_{2(gas)} \rightarrow O_{(ads)} \tag{7}$$

$$O_{2(gas)} \rightarrow e^- + O_{2(ads)}^- \tag{8}$$

$$4NH_{3(ads)} + 5O_{2(ads)}^- \rightarrow 4NO_{(gas)} + 6H_2O_{(gas)} + 5e^- \tag{9}$$

## 4.3 Volatile Organic Compounds (VOCs)

Volatile Organic Compounds (VOCs) easily volatilize in the atmosphere under normal conditions. A variety of chemicals like benzene, methanol, ethylene glycol, n-butanol, formaldehyde, methylene chloride, ethane, tetrachloroethylene, ethylene, toluene, xylene, etc. are listed as VOCs. Few VOCs are quite hazardous while few are less toxic. VOCs are emitted through various sources like refineries, motor vehicles, chemical manufacturing facilities, small or large-scale factories, and natural sources. All these materials cause some adverse effects on human life by causing acute or chronic health effects and they also affect the environment

and contribute to various issues like ozone layer depletion, and climate change. It is preferable to have a minimum concentration of VOCs below which are less harmful. One of the well-known gases that are particularly desirable to detect is VOCs.It is also preferable to detect these compounds due to stringent environmental laws and regulations. The concentration of VOCs can be measured and monitored by sensing them. For sensing VOCs, various sensors can be used but the recent interest is MOF-based nano-sensor which are flexible, selective, porous, accurate, and have a faster response time. Zinc, iron, cobalt, Nickel, and Sn-based MOF nanomaterials can be used as effective sensors. MOFs-derived nanostructured sensors for the VOCs gases detection are summarized in Table 5.

Ternary $\alpha$-$Fe_2O_3$-ZnO–Au nanocomposites for n Butanol and acetone detection were developed by Kaneti et al. [191]. 2–5 nm-sized Au particles were decorated on the surface of $Fe_2O_3$ and ZnO which contributed to improving the response by 2–6.5 times that of the single or binary composite of ZnO, Au, or $Fe_2O_3$. Due to the presence of Au particles on the surface, a quantity of active oxygen was increased via catalytic dissociation of molecular oxygen which in turn caused a high degree of oxygen depletion [191].

Acetone is a colourless and commonly used organic solvent in labs and industrial applications [192]. Humans are minimally irritated by short-term contact with acetone at 300–500 ppm for about 5 min, while long-term contact with high concentrations of acetone causes dizziness, fatigue, weakness of muscular, as well kidney and nerve damage [193, 194].To monitor the industrial environment and human health, high-performance acetone gas sensors are needed. Hence, for the detection of acetone gas, Zhang [71] synthesized MOFs derived $ZnO/Co_3O_4$ hallow with excellent response, less response/recovery time, high selectivity for acetone, and great repeatability. The $ZnO/Co_3O_4$ nanopolyhedrons were fabricated via utilizing the ZIF-8/ZIF-67 mixture as a MOFs precursor to form a precipitated $ZnO/Co_3O_4$ film sensor as shown in the SEM image in Fig. 17a. As well as the material is also characterized by the TEM analysis as demonstrated in Fig. 17b and c. The gas sensing mechanism followed for the acetone as illustrated in Fig. 17d, and molecules of acetone start to react with adsorbed $O_2$ ions to form $CO_2$ as demonstrated in Eqs. 10, 11, 12, 13. The most important parameter for the $ZnO/Co_3O_4$ toward highly gas sensing sensitivity is because ZnO and $Co_3O_4$ are n-type and p-type, respectively with 3.37 and 2.2 eV band gap to generated p-n heterojunctions at $ZnO/Co_3O_4$, and it is important part responsible for the improvement of gas sensing. The $ZnO/Co_3O_4$ sensor exhibited a 30.01 response for the acetone gas concentration of 100 ppm at 300 °C operating temperature as elicited in Fig. 17e. The response and recovery time obtained are 8 s and 2 s for acetone as shown in Fig. 17f. The $ZnO/Co_3O_4$ is highly selective for acetone

among the various gases $H_2S$, $CH_4$, $C_6H_6$, $CH_2O$, LPG, and $NH_3$ as shown in Fig. 17g [71].

$$O_{2(gas)} \rightarrow O_{2(ads)} \tag{10}$$

$$O_{2(ads)} \rightarrow e^- + O_{2(ads)}^- \tag{11}$$

$$O_{2(ads)}^- + e^- \rightarrow 2O_{(ads)}^- \tag{12}$$

$$CH_3COCH_{3(gas)} + 6O_{(ads)}^- \rightarrow 3CO_2 + 3H_2O + 6e^- \tag{13}$$
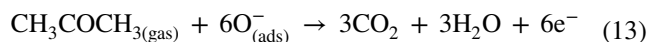
Zinc oxide-based nanocage having high sensing capacity (ppb or sub-ppm level) towards VOCs like benzene and acetone was developed by Li et al. [55]. According to their study, nanocage structure was proven to be better than singular ZnO and hollow nanocage showed a sensitivity of 2.3 ppm-1 for 0.1 ppm benzene and 15.3 ppm-1 toward 50 ppb acetone. A distinct hierarchical structure with a large specific surface area led to higher sensitivity. Alcohol and acetone were detected by MOF Copper-Benzene Tricarboxylate (Cu-BTC) nanoparticle synthesized as a layer of dielectric nanosensors of capacitive (Homayoonnia and Zeinali, 2016) [195]. According to the experiment, the sensor has a rapid response time, linearity, and reversible response time for various concentrations. Minimum detectable concentrations for acetone, isopropanol, ethanol, and methanol were 100.18 ppm, 77.80 ppm, 71.05 ppm, and 61.99 ppm, respectively using newly formed sensors.

Xiong and his group (2019) fabricated a $Co_3O_4$/graphene nanoscrolls derived from Co-MOF-74 for the detection of acetone. In comparison to other sensors, higher response (58.1 for 1 ppm), response time, and recovery time (12 s/66 s) were observed. Multidimensional gas transfer channels of nanoscrolls and large heterojunction interfaces were the key factors responsible for the fabulous response. Fabricated nanosphere has detection capability in the range of ppb as well with response 1.24 for 50 ppb acetone [196]. NiO/ZnO composites with varying $Ni^{2+}$ content were fabricated by Zhang et al. (2020). A comparison of response for acetone was done with pure and composite metal oxides and 5% NiO/ZnO was proven to be better with 97.134 response for 500 ppm acetone which was 7.3 times higher than that of pure ZnO. A detailed sensing mechanism was also discussed by the authors [197].

One type of colorless material with a distinctive fragrant smell that is frequently employed in consumer goods and industrial applications is toluene. Toluene, which has a powerful effect on the neurological system and can cause brain function problems as well as kidney or liver damage, is regrettably extremely dangerous to human health [198, 199]. Zhang and coworkers (2019) used NiFe-bimetallic
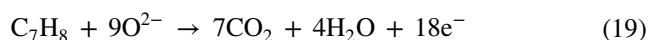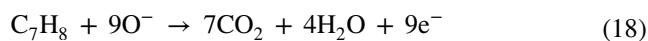
**Table 5** Summary of work done on MOF-derived metal oxide sensors for VOCs

| VOC | Precursor | Sensor | Synthesis route | Response | Temperature | Response/Recovery | Detection limit | References |
|---|---|---|---|---|---|---|---|---|
| Ethanol | ZIF-8 | Ag functionalized ZnO hollow nanocages (NCs) | Calcination of Ag encapsulated ZIF-8 MOF | The highest response for 84.6 for 100 ppm ethanol at 250 °C, and good selectivity and reproducibility | The optimum temperature of 250 °C | 5 s / 10 s | 64.5 ppb | [213] |
| | MIL-68(In/Ga) | Mesoporous In/Ga oxides (IGOs) derived from MIL-68(In/Ga) | Solvothermal synthesis of In/Ga-based MIL-68 followed by calcination at 500 deg C to produce In/Ga oxides | The highest response of 80–110 towards 300 ppm ethanol for IGOs produced from MIL-68 with In/Ga ratios of 3: 2 and 1: 1 | The optimal temperature of 200–235 °C | 3.5 s/7 s | 2 ppm | [220] |
| | ZIF-67 | MOFs derived Co3O4 Concave Nanocubes | Co₃O₄ Concave Nanocubes Fabricated by the calcinations of Co-based MOFs (Co-MOF, ZIF-67) | The highest response 3.4 towards 200 ppm ethanol and | The optimal temperature of 150–300 °C | Most minimal response/recovery time < 10 s | 10 ppm | [68] |
| Acetone | ZIF-8 and ZIF-67 | MOF-derived ZnO/Co₃O₄ nanocomposite film sensor | Calcination of ZIF-8/ZIF-67 mixture | Response of 30.01 for 100 ppm acetone, and high selectivity towards acetone presence of NH₃, HCHO, C₆H₆, CH₄, and H₂S | The optimum temperature of 300 °C | 8 s/2 s | Lowest conc. of 1 ppm reported | [71] |
| | ZIF-67 | Pd and Co₃O₄ functionalized SnO₂ hollow polyhedron nanocubes | Calculations of ZIF-67@Pd followed by Galvanic Replacement Reaction with SnCl₂ | $R_{air}/R_{gas} = 22.8$ @ 5 ppm acetone | The optimal temperature of 450 °C | 90.8 s/108.4 s | 5 ppb | [88] |
| n-propanol | Zn/Ni Bimetallic Organic Framework | Zn/Ni Bimetallic Organic Framework Derived ZnO/NiO Heterostructure | Synthesis of Zn/Ni Bi-MOF through ion exchange post-synthetic strategy followed by calcination to produce ZnO/NiO heterostructure | Ultrahigh response of 280.2 toward 500 ppm n-propanol | The optimal temperature of 275 °C | 31.3 s/18.2 s | 200 ppb | [219] |
| Toluene | NiFe-bimetallic metal–organic framework | NiFe₂O₄ Nano-Octahedrons | NiFe₂O₄ nano-octahedrons were calcinated from NiFe-bimetallic MOFs octahedrons synthesized by a facile refluxing method | Response 6.41 for 1000 ppm toluene response/recovery 25 s/40 s | The optimal temperature of 260 °C | 25 s /40 s | 1 ppm | [200] |

**Table 5** (continued)

| VOC | Precursor | Sensor | Synthesis route | Response | Temperature | Response/Recovery | Detection limit | References |
|---|---|---|---|---|---|---|---|---|
| Formaldehyde | Zn–Co–Prussian blue analog (PBA) | $Zn_3[Co(CN)_6]_2$ Prussian blue analog (PBA) MOF derived PDO-ZnO/ZnCo$_2$O$_4$ microspheres | Synthesis of $Zn_3[Co(CN)_6]_2$ solid microsphere through co-precipitation followed thermal annealing process and subsequent decoration of PdO nanoparticles | A high response of S=26.9 towards 100 ppm formaldehyde | The optimal temperature of 139 °C | 9 s/14 s | 200 ppb | [221] |

metal–organic framework (MOFs) octahedrons to fabricate $NiFe_2O_4$ nano-octahedrons with hollow interiors for toluene detection. Outstanding sensing phenomena were observed for 100 ppm toluene with fast response and recovery time- 25 s/40 s with a 1 ppm minimum detection limit concentration. Hollow interiors were not only responsible for better sensing properties but the catalytic activity of 30 nm-sized nanoparticles was another major reason for the same [200–202]. The morphological SEM and TEM images of the $NiFe_2O_4$ nano-octahedrons are presented in Fig. 18 and the sensing response increase with an increasing concentration of the toluene gas. In addition, The obtained great results for the detection of the toluene gases by the sensor response and other studies are presented in Fig. 18. The sensing mechanism of the sensor for the toluene can be clarified by the following Eqs. 14, 15, 16, 17, 18, 19:

$$O_{2(gas)} \rightarrow O_{2(ads)} \tag{14}$$

$$O_{2(ads)} + e^- \rightarrow O_{2(ads)}^- \tag{15}$$

$$O_{2(ads)}^- + e^- \rightarrow 2O_{(ads)}^- \tag{16}$$

$$O^- + e^- \rightarrow O^{2-} \tag{17}$$

$$C_7H_8 + 9O^- \rightarrow 7CO_2 + 4H_2O + 9e^- \tag{18}$$

$$C_7H_8 + 9O^{2-} \rightarrow 7CO_2 + 4H_2O + 18e^- \tag{19}$$

Koo et al. [203] the publication reported on the use as a template of metal@MOFs for the production of complicated catalysts decorated on WO$_3$-based chemiresistors is another significant study. The gas sensing abilities of WO$_3$ nanofibers were significantly enhanced by the metal@metal oxides generated from metal@MOFs. Using an electrospinning technique, Pd-loaded ZIF-8 (Pd@ZIF-8) was decorated on electrospun nanofibers made of polymers and precursors of tungsten (W) (Fig. 19a). The as-spun nanofibers were successfully functionalized by the ultrasmall Pd nanoparticles loaded in ZIF-8, as seen in Fig. 19b and c. Pd@ZIF-8 loaded nanofibers were further calcined to yield WO$_3$ nanofibers functionalized with Pd-loaded ZnO nanocubes (Pd@ZnO) (Fig. 19d and e). Interestingly, the Pd@ZnO-loaded WO$_3$ nanofibers showed better toluene detection capacity (R$_{air}$/R$_{gas}$ = 22.22 to 1 ppm at 350 °C) with good selectivity and quick response time (~ 20 s). The multi-heterojunctions structures of WO$_3$-Pd,ZnO-Pd, and WO$_3$-ZnO were responsible for inducing the huge electron depletion zone in n-type WO$_3$
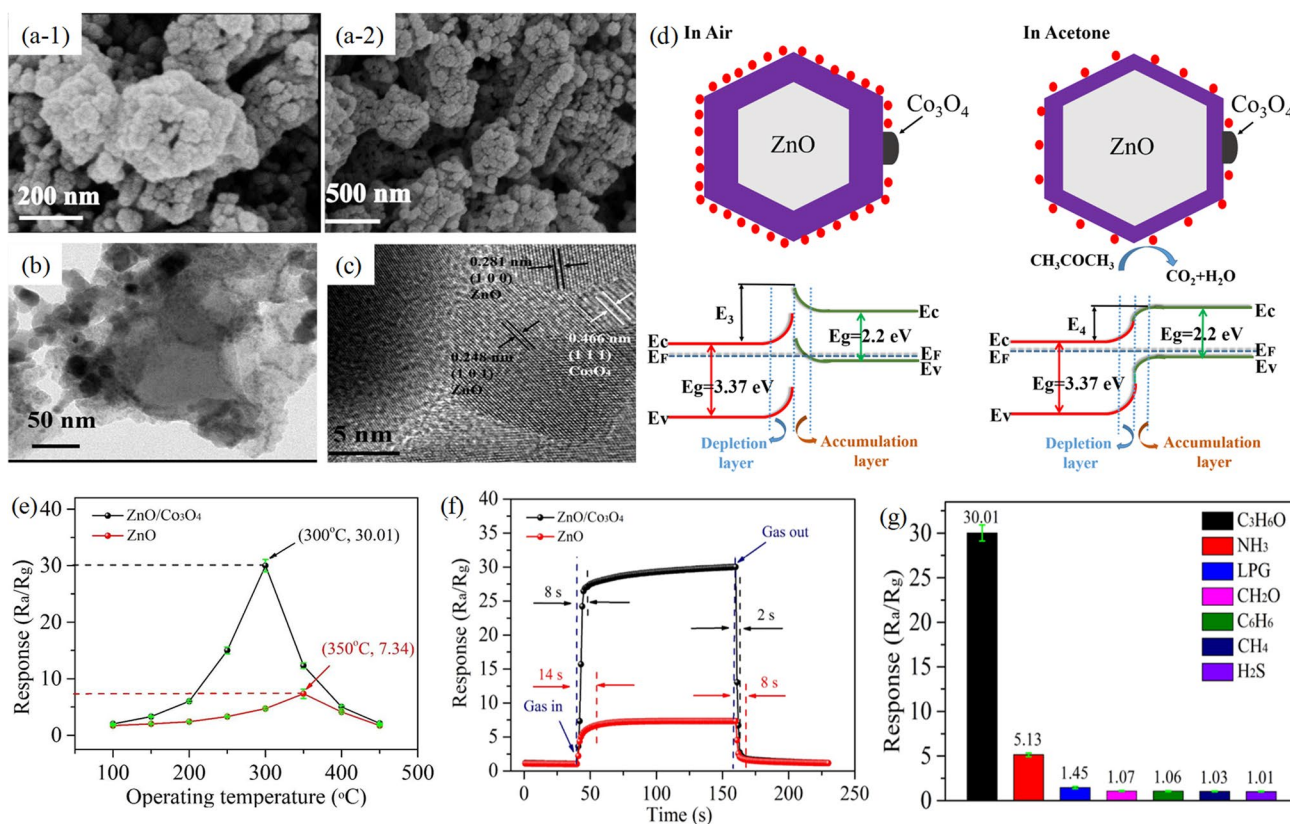
**Fig. 17 a** SEM Image of the hallow ZnO/Co$_3$O$_4$nanocomposites; **b, c** TEM and HRTEM analysis for nanocomposites of ZnO/Co$_3$O$_4$; **d** Schematic illustration of sensing mechanism of the ZnO/Co$_3$O$_4$ sensor in air and in acetone; **e** Response curve of ZnO and ZnO/Co$_3$O$_4$ for 100 ppm acetone at different temperature; **f** Response-Recovery curve of ZnO and ZnO/Co$_3$O$_4$ to 100 ppm acetone; **g** Selectivity of the ZnO/Co$_3$O$_4$ sensor for various gases [71]. *Reprinted with permission from Ref. (Zhang* et al.*), Copyright 2018, Elsevier*

nanofibers, which allowed for a significant resistance fluctuation during toluene sensing [204]. Additionally, when exposed to toluene, Pd nanoparticles were immediately converted to Pd, and when exposed to air, they partly oxidized to PdO. Which effectively modulated the surface depletion layers (Fig. 19g).

For detection of VOC—n-Butanol, porous iron oxide was synthesized through heating of Fe-MOF (FeFe(CN)$_6$). Materials having diverse phase compositions like α-Fe$_2$O$_3$, γ-Fe$_2$O$_3$, and combine phases of α-Fe$_2$O$_3$ and γ-Fe$_2$O$_3$ showed different results in the performance of gas sensing due to differences in the mechanism of sense. Authors concluded that, though α-Fe$_2$O$_3$ nanomaterial had a smaller specific surface area around 13.1 m$^2$ g$^{-1}$ than that of γ-Fe$_2$O$_3$ (108.3 m$^2$g$^{-1}$), it showed a higher response towards the n-butanol [77]. In another study of n-Butanol detection by Wang and other coworkers (2019) [205], porous metal oxide of cobalt was synthesized and the effect of size and shape of metal oxide on sensing properties was studied. By varying the ratio of Co$^{2+}$ ions and methyl imidazole, different morphologies—octadecahedron created from a rhombic dodecahedron that had been truncated, a multilayered flower-like

structure, and rhombic dodecahedron were studied for sensing n-Butanol. For small-sized nanoparticles, larger quantities of them at the surface showed better sensitivity towards VOC. Figure 20 shows the response curves, response recovery, and selectivity of as-prepared porous Co$_3$O$_4$ sensors.

Andres and his group (2020) [206] prepared capacitive type thin films of MIL-96(Al) nanoparticles on substrates of Si/SiO$_2$ sensor for the detection of VOCs like methanol, toluene, chloroform, major being water, and methanol (Fig. 20). Quick response time of around 10–15 min was observed for a single MOF monolayer than that of drop cast film (50 min) [206]. Cheng et al., [207] Co$_3$O$_4$ nanospheres were synthesized from CO-based MOF. The effect of calcination temperature was studied and concluded that the nanosphere calcined at 400 °C temperature showed a higher response of 53.78 for n butanol. Stability, selectivity, and reproducibility were also examined and response values were around 86.74% and 74.93% even after 45 and 75 days respectively [207].

Various classes of VOCs like aromatics, ketones, aliphatics, aldehyde, alcohol, chlorinated compounds, etc. were studied and compiled by Li and colleagues (2020). A
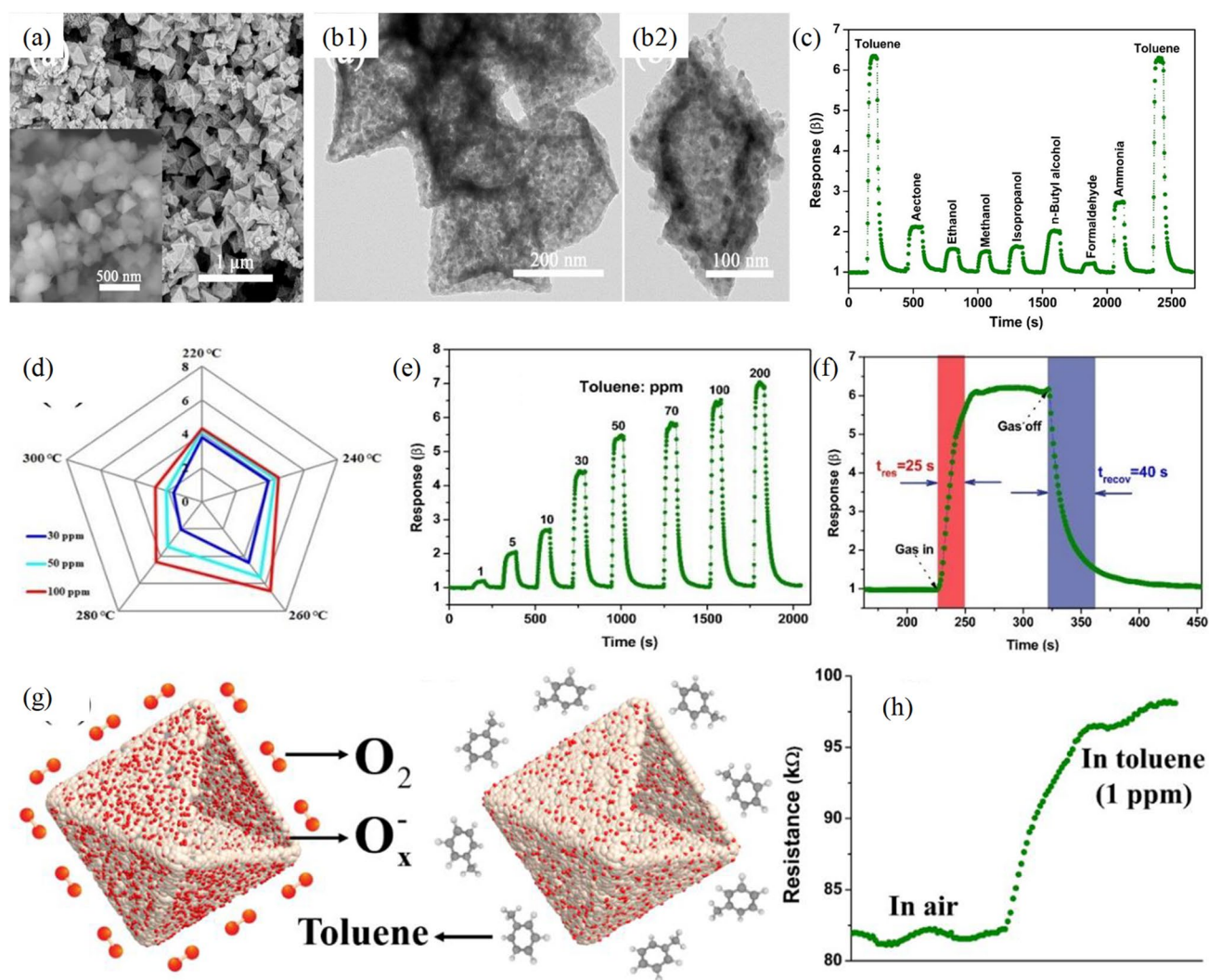
**Fig. 18 a** The FESEM image of NiFe$_2$O$_4$ nano-octahedrons; **b** The TEM image of NiFe$_2$O$_4$ nano-octahedrons; **c** selectivity test of the sensor NiFe$_2$O$_4$ to various gases of 100 ppm concentrations at 260 °C; **d** Polar graphs of the NiFe$_2$O$_4$ sensor response to toluene 30, 50 and 100 ppm at temperature range 220–300 °C; **e** Dynamic curve of the NiFe$_2$O$_4$ nano-octahedrons sensor for the different concentrations of toluene; **f** The response/recovery to 100 ppm toluene; **g** schematic illustration of gas sensing mechanism of the sensor in air and in toluene; **h** The change in resistance to exposure of the toluene of 1 ppm at 260 °C [200]

detailed study of the mechanism and application of MOF was done in this review paper [41] (Fig. 21).

It is widely known that ethanol vapor is one of the most thoroughly investigated gases in the domain of gas sensors, in large part because of the high demand in the biomedical, chemical, and culinary sectors, notably in wine-quality monitoring and breath analysis [208–211]. Hence, it is essential to create a superior ethanol gas sensor with excellent response. Zhang et al. [212]built a gas sensor for ethanol detection using hierarchical hollow ZnO nanocages generated from ZIF-8 with a superior 139.41 response and Fig. 22 displays the response/recovery time of 2.8/56.4 s for the 100 ppm ethanol at an operating temperature of 325 °C. Later on, for the detection of ethanol Zhang et al. [213] reported MOFs-derived nanocage

of ZnO hollow functionalized with nanoscale Ag catalyst by the process as shown in Fig. 23a. ZIF-8 should be created, Ag-ZIF-8 precursor must be generated by reducing Ag ions into Ag nanoparticles, and Ag-ZnO hollow NCs must be developed by calcination of the Ag-ZIF-8 precursor in the air at 500 °C with a rate of heating 10 °C min$^{-1}$. The SEM morphological image of ZnO-hollow and Ag-ZnO hollow are shown in Fig. 23b and c, respectively. The ZIF-8 template exhibit a smooth surface in cubic nanostructure in three-dimensional. To add with, the TEM image of the prepared Ag-ZnO hollow nanocage is displayed in Fig. 23d with porosity and hollow structure. Figure 23f demonstrate the response curve by the five kinds of sensor toward the detection of concentration of 100 ppm ethanol gases at various operating temperature.
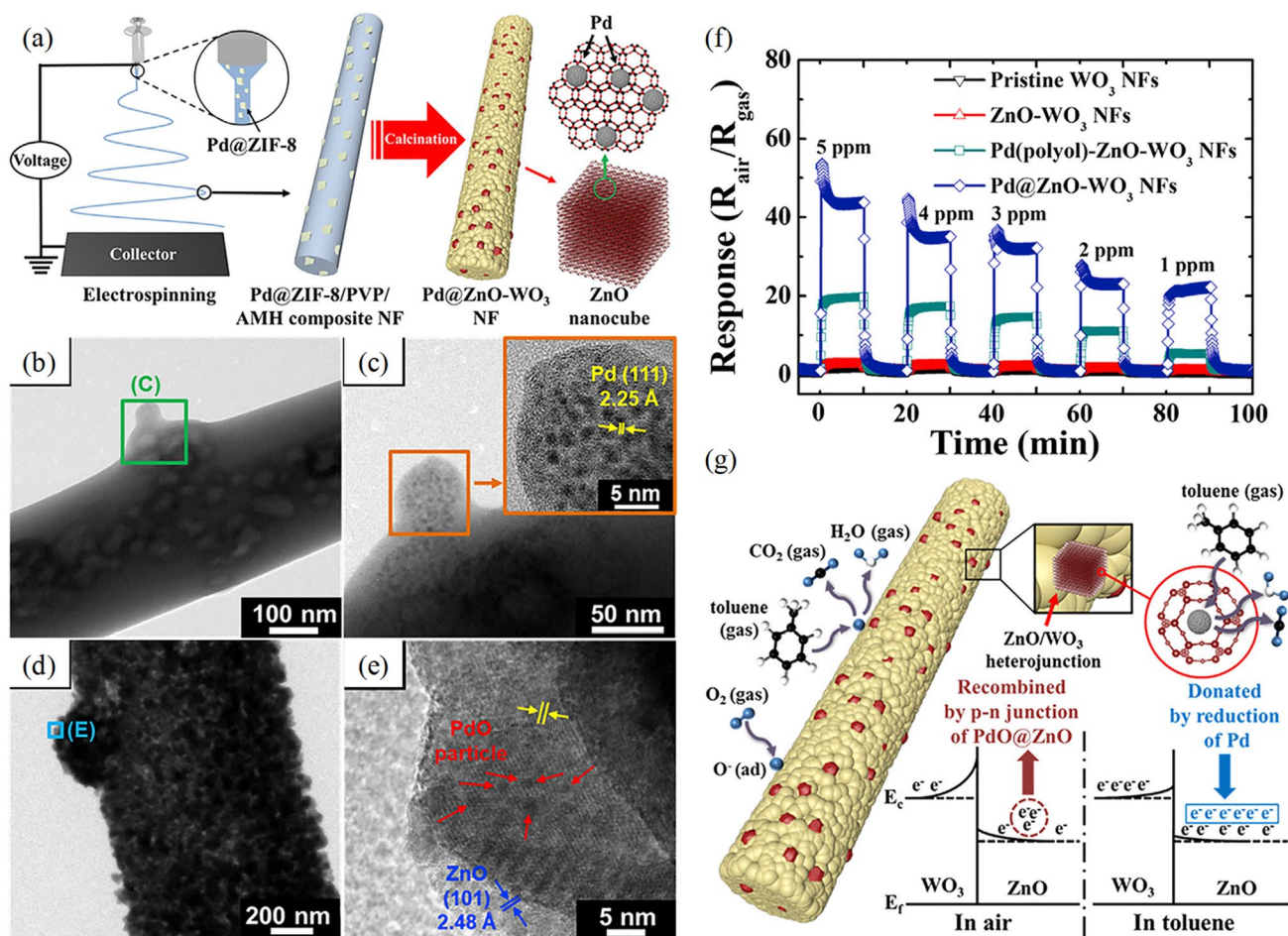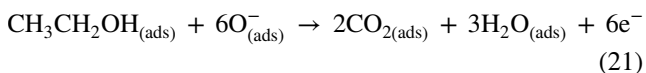
**Fig. 19** **a** Synthesis of Pd@ZnO loaded WO$_3$ nanofibers schematic diagram; **b** TEM image of Pd@ZIF-8 loaded as-spun nanofiber; **c** HRTEM image of Pd@ZIF-8 loaded as-spun nanofiber; **d** TEM image of Pd@ZnO loaded WO$_3$ nanofiber; **e** HRTEM image of Pd@ ZnO loaded WO$_3$ nanofiber; **f** Sensing properties for Pd@ZnO loaded WO$_3$ nanofibers [203]. *Reprinted with permission from Ref. (Koo et al.), Copyright 2016, ACS*

In which, 1.0 ml Ag-ZnO exhibited most effective response ($R_a/R_g = 84.6$). The study also investigated the selectivity of sensors toward various gases, such as acetic acid, methanol, ammonia, formic acid, carbon dioxide, nitrogen dioxide, and ethanol (Fig. 23g). The sensor exhibits a very fast response/recovery time of 5 s/10 s for the 100 ppm ethanol as elicited in Fig. 23h. Moreover, the sensing mechanism involved in the interaction between O$^-$ species and ethanol, as shown in Eqs. 20 and 21 [213].

$$O_{2(ads)} \rightarrow e^- + 2O^-_{2(ads)} \tag{20}$$

$$CH_3CH_2OH_{(ads)} + 6O^-_{(ads)} \rightarrow 2CO_{2(ads)} + 3H_2O_{(ads)} + 6e^- \tag{21}$$

One of the most significant organic solvents, n-propanol is manufactured in large quantities and consumed in numerous industrial sectors, including printing, cosmetics, and pharmaceuticals [214]. N-propanol, on the other hand, is a colorless, explosive, and deadly volatile organic compound (VOC) that is harmful to human health and generally causes explosions when exposed to heat or flame [215]. As a result, it is now crucial for the protection of human health and the environment to build n-propanol sensors that are affordable, extremely sensitive, and selective. Recently, Bi-MOFs (Bimetallic organic framework), a new kind of hybrid material involved inorganic–organic structure composed of organic ligand and 2 ions of metal have been considered as new generation material for gas sensing [68, 183, 216, 217]. For example, Sun et al. By calcining a Co and Zn-based bimetallic organic framework created Co$_3$O$_4$/ZnO composites that display high selectivity and good stability for formaldehyde [218]. Li et al. effectively created a bamboo-like CuO/In$_2$O$_3$ heterostructure based on a Cu/In bimetallic organic framework with enhanced H$_2$S sensing properties[183]. Zhao et al. [219] developed Zn/Ni
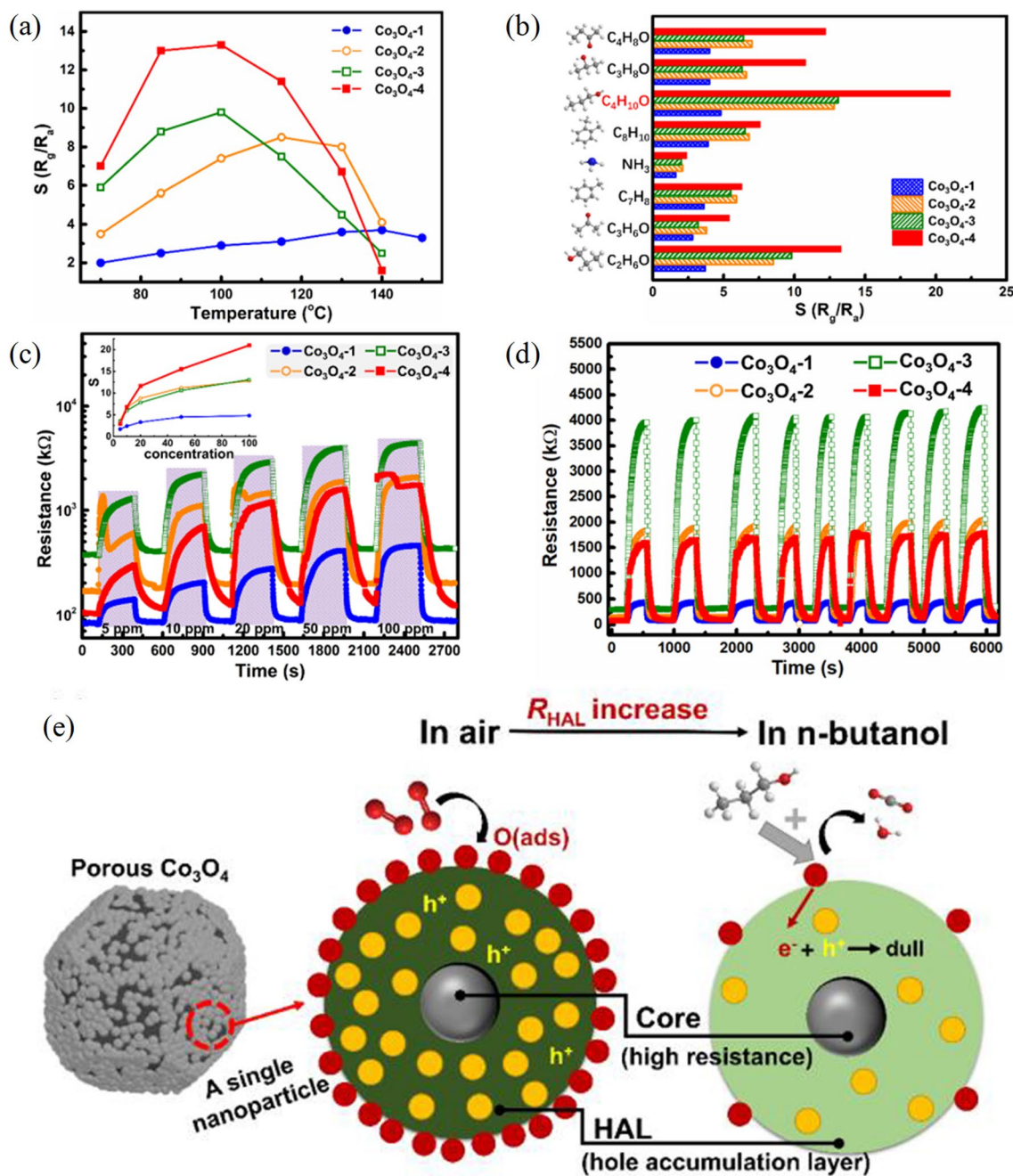
**Fig. 20** Main gas-sensing properties of as-prepared porous $Co_3O_4$ sensors where $Co_3O_4$-1, $Co_3O_4$-2, $Co_3O_4$-3 and $Co_3O_4$-4 represent Co2 +:2-mIM ratios of 1:4, 1:20, 1:40 and 1:80 respectively during synthesis **a** Operating temperature-dependent response curves for ethanol concentrations of 100 ppm; **b** Comparison of response to several 100 ppm VOC types at their respective acceptable operating temperatures; **c** At the ideal operating temperatures, sensing transient curves to various n-butanol concentrations and their concentration-dependent response curves were measured; **d** 9 periods of response-recovery curves at the corresponding optimal operating temperatures to 100 ppm n-butanol; **e** Schematics diagrams illustrated the gas sensing mechanism for the n-butanol by the $Co_3O_4$ [205]. *Reprinted with permission from Ref. (Wang* et al., *2019), Copyright 2019, Elsevier*

Bi-MOFs derived ZnO/NiO heterostructured for n-propanol detection. Here, with the use of an ion-exchange post-synthetic method and subsequent calcination technique, effectively manufacture a Zn/Ni Bi-MOF derived ZnO/NiO heterostructure for n-propanol sensing. The ion exchange approach eliminates the inhomogeneous issue brought on by the various reaction kinetics of metals and allows for the synthesis of Bi-MOFs, which is not possible using traditional solvothermal techniques. Figure 24a shows the concept for creating a ZnO/NiO heterostructure for n-propanol gas detection. Figure 24b
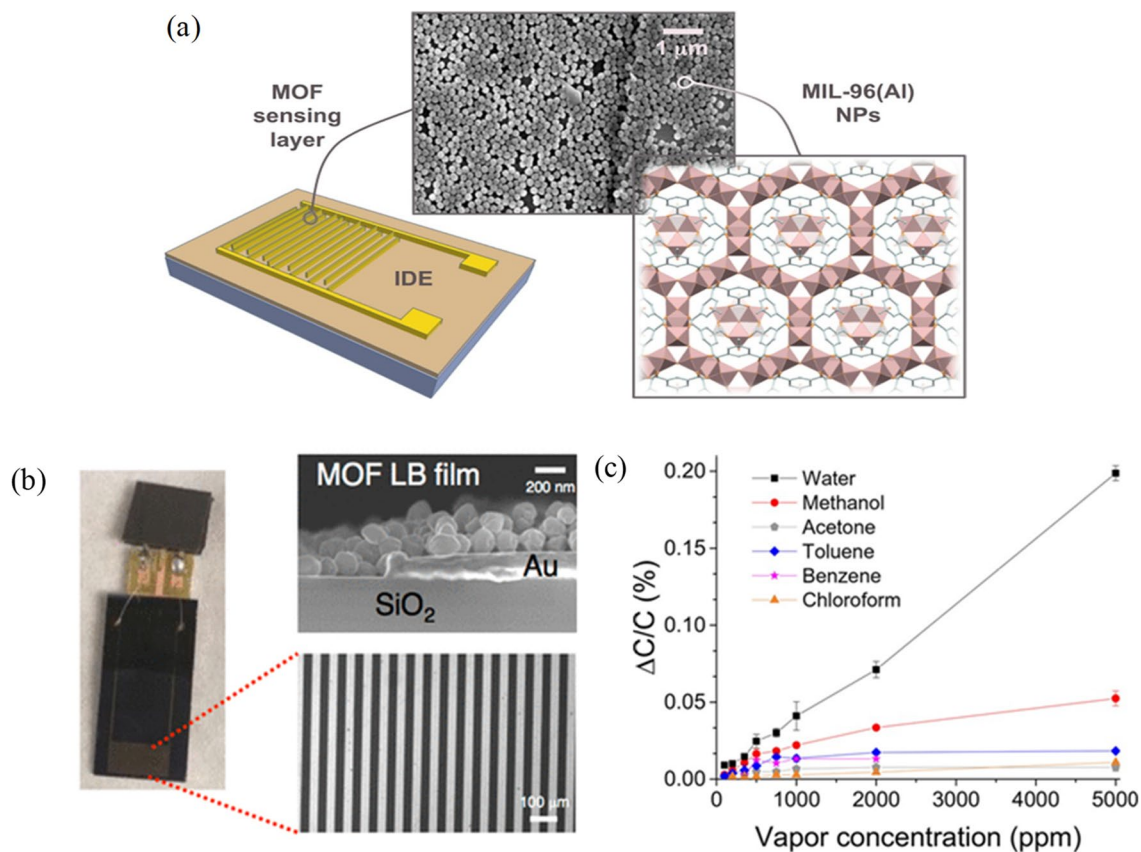
**Fig. 21 a** Schematic diagram of the prepared thin films of MIL-96(Al) NPs on Si/SiO$_2$; **b** Prepared MOFs LB Film of MIL-96(Al) NPs on Si/SiO$_2$ and demonstrated SEM image; **c** Selectivity of LB- based MIL-96(Al) for different VOCs gases of 0 to 5000 ppm [206]. *Reprinted with permission from Ref. (Andres et al., 2020), Copyright 2020, ACS*
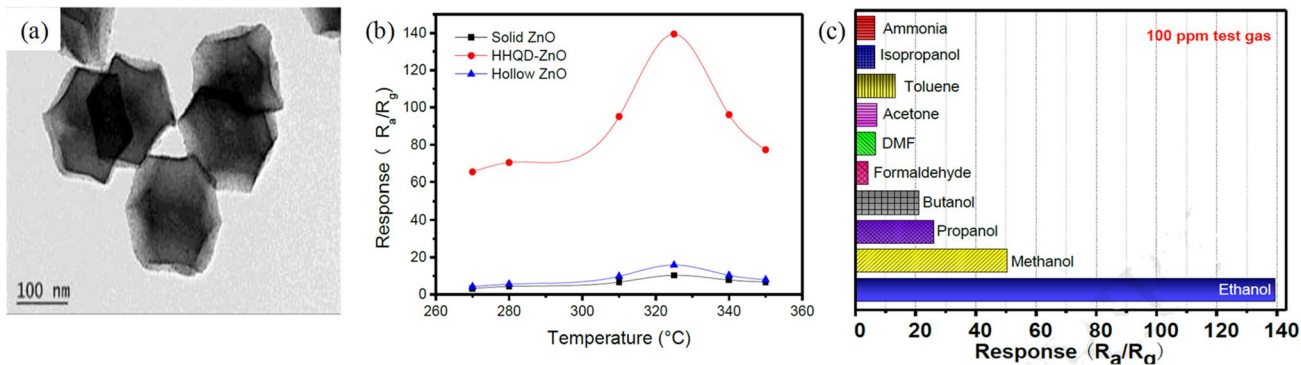


**Fig. 22** HHQD-ZnO nanocages are shown in **a** TEM pictures; **b** sensor HHQD-ZnO, hollow ZnO, and solid ZnO nanocages for the detection of 100 ppm ethanol at various temperatures; and **c** response-based HHQD-ZnO nanocages for the detection of various gases at 100 ppm concentrations [212]. *Reprinted with permission from Ref. (Zhang et al., 2019), Copyright 2019, Elsevier*

shows the SEM morphology of ZnO/NiO-48 h after calcination, Fig. 24c and Fig. 24d display the elemental mapping of the Zn and Ni, respectively. The response for the detection of n-propanol gas at various temperatures, by the calcination process at different times, is demonstrated in Fig. 24f. The sensor response was 282.2 toward 500 ppm n-propanol at an operating temperature of 275 °C. The n-propanol gas is highly selective by the ZnO/NiO-48 h (Fig. 24g). Figure 24i shows an example of an air and n-propanol gas detection apparatus. When exposed to air, the oxygen molecules will absorb onto the ZnO/NiO surface of the sensor, capturing free electrons from the ZnO to produce oxygen species ($O^{2-}$, $2O^-$). When
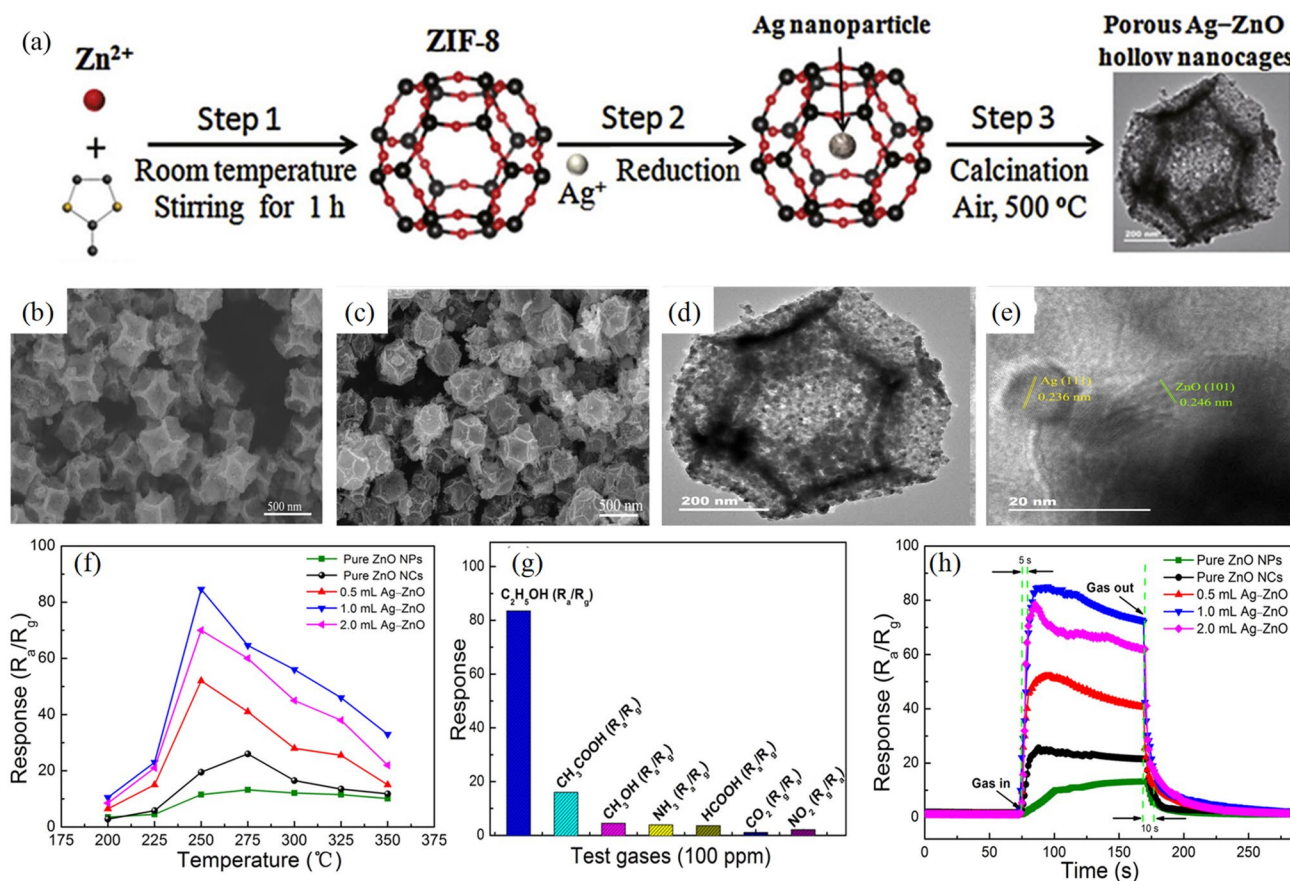
**Fig. 23** **a** Steps involved in the synthesis of hollow Ag-ZnO NCs are shown schematically. Steps involved in the synthesis of hollow Ag-ZnO NCs are shown schematically; **b** SEM image of pristine ZnO hollow NCs; **c** SEM image of Ag–ZnO hollow NCs; **d** TEM image of the Ag-ZnO hollow nanocage; **e** HRTEM image of the Ag-ZnO hollow nanocage; **f** Response curve for the 100 ppm ethanol by the different 5 type sensor at different temperature; **g** Selectivity study for the Various gases of 100 ppm concentration by the Ag-ZnO NCs; **h** Response-recovery curve for the 100 ppm ethanol by the 5 different types Ag-ZnO sensor [213]. *Reprinted with permission from Ref. (Zhang et al., 2019), Copyright 2019, Elsevier*

n-propanol is exposed, it begins to react with oxygen species, releasing the electrons it had been holding onto [219].

## 5 Conclusion and Future Perspective

All in all, it can be concluded that Metal–organic frameworks can be put in the category of advanced materials for gas sensing devices. To begin with, MOFs-based gas sensors have been extensively used in the last one decade as it eliminates the issues produced by conventional gas sensors. This material can be utilized to receive the properties of gas sensors like high selectivity, sensitivity, long-lasting features, affordable synthesis routes, and so on. However, the problem related to the number of analytes that absorbs on the surface of MOF-based sensors still remains. Thus, to remove this hindrance nanostructures have been introduced to the MOF-based materials, with this the gas sensor produced with enhanced gas sensing capacity. Nanostructures-based

embedded MOFs provide numerous advantages such as a greater number of active sites, large pore sizes, less time consumption in terms of redox reaction between analytes and the surface of the material, high efficiency, high selectivity and stability, more accurate results, and to the name of few. Hence, these days scientists have put more emphasis on the more advanced routes to develop such types of sensors so that the detection of toxic gases in various fields will become more transparent and feasible.

After literature, we have identified a few drawbacks with respect to nano-derived MOFs gas sensors. The foremost one is, stability-the short-term stability is achieved but, long-term stability is still problematic, this particular occurs when the atmosphere consists of the humid environment, the variations in the PH, and so on. To remove this, the selection of metal in the MOF material is the key. Second, the charge transport mechanism is still not understood properly, various computational modeling can be used to identify proper structure–property correlations. Third, it is still very difficult to integrate
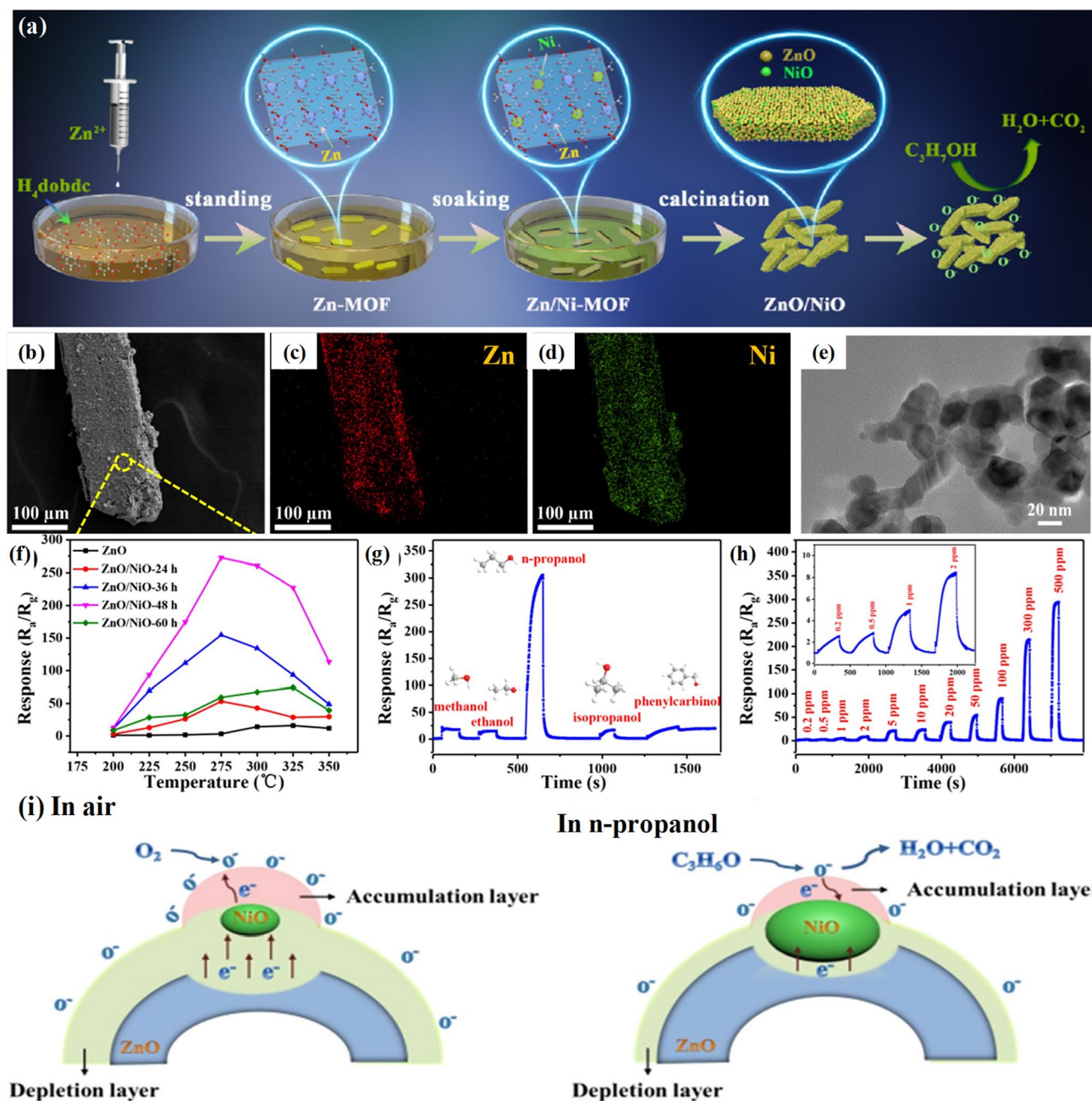
**Fig. 24** **a** Schematic Diagram for the fabrication of ZnO/NiO Heterostructure to n-propanol gas detection; **b-d** SEM images and elemental mapping of ZnO/NiO-48 h; **e** TEM image of NiO/ZnO-48 h; **f** Response curve of ZnO/NiO heterostructure and ZnO toward 500 ppm n-propanol at various temperature; **g** Selectivity test of NiO/ZnO heterostructure towards different gases of 500 ppm concentration; **h** Dynamic response curve of ZnO/NiO-48 h towards 0.2–500 ppm n-propanol concentration at operating temperature 275 °C; **i** Schematic diagram of gas sensing mechanism of ZnO/NiO heterostructure exposure in air and n-propanol [219]. *Reprinted with permission from Ref. (Zhao* et al., *2021), Copyright 2021, ACS*

targeted MOFs onto various tiny electronic devices with good homogeneity, adjustable thickness, orientation, noticeable adhesion/contacting, and accurate location, especially with complex designs (such as patterns and optical waveguides). A generic approach that is applicable to most MOFs and resolves the aforementioned problem would allow MOFs to

be used in micro-and/or optoelectronic devices with a variety of applications in mind, such as gas sensing. Fourth, the majority of studies show that single manufacturing of MOFs-based sensors, instead of array integrated sensors with multiple MOFs could be used to measure complex gases. For better data processing and pre-training, the MOF-based sensors, and

pertinent algorithms must be created or adopted. As a result, Machine learning-based lifetime prediction, self-calibration, and anomaly detection in MOF-based sensors are practical and economical. Overall, this review certainly provides fundamental insights into MOFs-derived nanostructure as a gas sensor. Besides the issues, some of the potential applications of MOF derived nanostructure of gas sensor can be explored such as in aerospace, medical health, industrial production, in IoT 4.0 industrial revolution, smart wear, smart home, food safety, and, security check. In addition to that, these type of sensors activity may further exploited to identify the working of sensor in humid, acidic, or alkaline conditions. This review will help the upcoming sophomores who will do the research in this field; also it will help all the researchers who are working with gas sensing devices. Finally, we hope this paper will spread awareness in the commercial market to develop and start installing MOF-based gas sensors, instead of a conventional ones.

## Declarations

**Competing Interest** Authors state they do not have any conflict of interest.

## References

1. S.-J. Kim, S.-J. Choi, J.-S. Jang, H.-J. Cho, I.-D. Kim, Acc. Chem. Res. **50**, 1587 (2017)
2. A. Loutfi, S. Coradeschi, G.K. Mani, P. Shankar, J.B.B. Rayappan, J. Food Eng. **144**, 103 (2015)
3. S.K. Brown, M.R. Sim, M.J. Abramson, C.N. Gray, Indoor Air **4**, 123 (1994)
4. R. Kostiainen, Atmos. Environ. **29**, 693 (1995)
5. N. Joshi, T. Hayasaka, Y. Liu, H. Liu, O.N. Oliveira, L. Lin, Microchim. Acta **185**, 213 (2018)
6. V. Shah, J. Bhaliya, G.M. Patel, P. Joshi, J. Inorg. Organomet. Polym. Mater. **32**, 741 (2022)
7. N. Joshi, V.K. Tomer, R. Malik, J. Nie, Functional nanomaterials advances in gas sensing technologies, in *Recent advances on uv-enhanced oxide nanostructures gas sensors*. ed. by S. Thomas, N. Joshi, K. Tomer (Springer, Singapore, 2020), pp.143–159
8. S. Thomas, N. Joshi, T. Vijay, *Functional Nanomaterials Advances in Gas Sensing Technologies* (Springer Singapore, Singapore, 2020)
9. N. Joshi, L.F. da Silva, H. Jadhav, J.-C. M'Peko, B.B. Millan Torres, K. Aguir, V.R. Mastelaro, O.N. Oliveira, RSC Adv. **6**, 92655 (2016)
10. N. Joshi, L.F. da Silva, H.S. Jadhav, F.M. Shimizu, P.H. Suman, J.-C. M'Peko, M.O. Orlandi, J.G. Seo, V.R. Mastelaro, O.N. Oliveira, Sens. Actuators B Chem. **257**, 906 (2018)
11. R. Malik, V.K. Tomer, V. Chaudhary, N. Joshi, S. Duhan, *In met. Oxide nanocomposites* (Wiley, Hoboken, 2020), pp.265–301
12. N. Joshi, F. M. Shimizu, I. T. Awan, J. C. M'Peko, V. R. Mastelaro, O. N. Oliveira, and L. F. Da Silva, in *Proc. IEEE Sensors* (IEEE, 2017), pp. 1–3
13. N. Joshi, L.F. da Silva, F.M. Shimizu, V.R. Mastelaro, J.-C. M'Peko, L. Lin, O.N. Oliveira, Microchim. Acta **186**, 418 (2019)
14. L. Wang, Sensors Actuators A Phys. **307**, 111984 (2020)
15. J. Bhaliya, M.R. Popaliya, G.M. Patel, A. Mishra, V. Shah, *In 1D semicond. Hybrid nanostructures* (Wiley, Hoboken, 2023), pp.127–162
16. Y. Xu, L. Zheng, C. Yang, W. Zheng, X. Liu, J. Zhang, A.C.S. Appl, Mater. Interfaces **12**, 20704 (2020)
17. H. Liu, Y. Chu, Y. Liu, T. Hayasaka, N. Joshi, Y. Cui, X. Wang, Z. You, and L. Lin, in *Proc. IEEE Int. Conf. Micro Electro Mech. Syst.* (IEEE, 2018). pp. 210–213.
18. H. Liu, Y. Liu, Y. Chu, T. Hayasaka, N. Joshi, Y. Cui, X. Wang, Z. You, L. Lin, Sensors Actuators B Chem. **263**, 94 (2018)
19. H. Liu, Y. Chu, Y. Liu, T. Hayasaka, Z. Shao, N. Joshi, X. Wang, Z. You, and L. Lin, 2019 IEEE 32nd Int. Conf. Micro Electro Mech. Syst. (2019). 488
20. Y. Yan, G. Yang, J.-L. Xu, M. Zhang, C.-C. Kuo, S.-D. Wang, Sci. Technol. Adv. Mater. **21**, 768 (2020)
21. A. Kumar, N. Joshi, *In nanobatteries and nanogenerators* (Elsevier, Amsterdam, 2021), pp.463–489
22. R. Malik, N. Joshi, V.K. Tomer, Adv. Mater. **2**, 4190 (2021)
23. R. Malik, V.K. Tomer, N. Joshi, V. Chaudhary, L. Lin, *In nanosensors for smart cities* (Elsevier, Amsterdam, 2020), pp.251–266
24. T. Wu, N. Prasetya, K. Li, J. Memb. Sci. **615**, 118493 (2020)
25. I.-D. Kim, A. Rothschild, H.L. Tuller, Acta Mater. **61**, 974 (2013)
26. M.-S. Yao, W.-H. Li, G. Xu, Coord. Chem. Rev. **426**, 213479 (2021)
27. X.-F. Wang, X.-Z. Song, K.-M. Sun, L. Cheng, W. Ma, Polyhedron **152**, 155 (2018)
28. M. Kiani, M.U. Rehman, X. Tian, B. Yakobson, Adv. Mater. Technol. **7**, 2101252 (2021)
29. H. Wang, W.P. Lustig, J. Li, Chem. Soc. Rev. **47**, 4729 (2018)
30. R. Malik, N. Joshi, V.K. Tomer, Mater. Adv. **2**, 4190 (2021)
31. I. Stassen, N. Burtch, A. Talin, P. Falcaro, M. Allendorf, R. Ameloot, Chem. Soc. Rev. **46**, 3185 (2017)
32. M. Campbell, M. Dincă, Sensors **17**, 1108 (2017)
33. W.-T. Koo, J.-S. Jang, I.-D. Kim, Chem **5**, 1938 (2019)
34. H. Li, M. Eddaoudi, M. O'Keeffe, O.M. Yaghi, Nature **402**, 276 (1999)
35. O.M. Yaghi, G. Li, H. Li, Nature **378**, 703 (1995)
36. B. Yan, J. Mater. Chem. C **7**, 8155 (2019)
37. A. Karmakar, P. Samanta, A.V. Desai, S.K. Ghosh, Acc. Chem. Res. **50**, 2457 (2017)
38. J.V. Alegre-Requena, E. Marqués-López, R.P. Herrera, D.D. Díaz, Cryst. Eng. Comm. **18**, 3985 (2016)
39. C. Arul, K. Moulaee, N. Donato, D. Iannazzo, N. Lavanya, G. Neri, C. Sekar, Sens. Actuators B Chem. **329**, 129053 (2021)
40. S.M. Majhi, A. Ali, P. Rai, Y.E. Greish, A. Alzamly, S.G. Surya, N. Qamhieh, S.T. Mahmoud, Nanoscale Adv. **4**, 697 (2022)
41. H.-Y. Li, S.-N. Zhao, S.-Q. Zang, J. Li, Chem. Soc. Rev. **49**, 6364 (2020)
42. H. Yuan, N. Li, W. Fan, H. Cai, D. Zhao, Adv. Sci. **9**, 2104374 (2022)
43. X. Huang, Z. Gong, Y. Lv, TrAC. Trends Anal. Chem. **153**, 116644 (2022)
44. E.M. Materón, R.S. Lima, N. Joshi, F.M. Shimizu, O.N. Oliveira, *In micro nano technol* (Elsevier, Amsterdam, 2019), pp.321–336
45. E.M. Materon, N. Joshi, F.M. Shimizu, R.C. Faria, O.N. Oliveira, *In Met. Oxides* (Elsevier, Amsterdam, 2021), pp.293–311

46. E.M. Materon, F.R. Gómez, N. Joshi, C.J. Dalmaschio, E. Carrilho, O.N. Oliveira, *In Nanosensors Smart Manuf* (Elsevier, Amsterdam, 2021), pp.347–371

47. E.M. Materon, G. Ibáñez-Redín, N. Joshi, D. Gonçalves, O.N. Oliveira, R.C. Faria, *In Nanosensors for Environmental Applications* (2020), pp. 87–129

48. J. Annamalai, P. Murugan, D. Ganapathy, D. Nallaswamy, R. Atchudan, S. Arya, A. Khosla, S. Barathi, A.K. Sundramoorthy, Chemosphere 298, 134184 (2022)

49. R.A. Gonçalves, R.P. Toledo, N. Joshi, O.M. Berengue, Molecules 26, 2236 (2021)

50. L. Esrafili, A.A. Tehrani, A. Morsali, L. Carlucci, D.M. Proserpio, Inorganica Chim. Acta 484, 386 (2019)

51. G. Ibáñez-Redín, N. Joshi, G.F. do Nascimento, D. Wilson, M.E. Melendez, A.L. Carvalho, R.M. Reis, D. Gonçalves, O.N. Oliveira, Microchim. Acta 187, 1 (2020).

52. M. Vasudevan, M.J.Y. Tai, V. Perumal, S.C.B. Gopinath, S.S. Murthe, M. Ovinis, N.M. Mohamed, N. Joshi, J. Taiwan Inst. Chem. Eng. 118, 245 (2021)

53. I.G. Subramani, V. Perumal, S.C.B. Gopinath, N.M. Mohamed, N. Joshi, M. Ovinis, L.L. Sze, J. Taiwan Inst. Chem. Eng. 116, 26 (2020)

54. M. Vasudevan, M.J.Y. Tai, V. Perumal, S.C.B. Gopinath, S.S. Murthe, M. Ovinis, N.M. Mohamed, N. Joshi, Biotechnol. Appl. Biochem. 68, 1386 (2020)

55. W. Li, X. Wu, N. Han, J. Chen, X. Qian, Y. Deng, W. Tang, Y. Chen, Sens. Actuators B Chem. 225, 158 (2016)

56. R. Malik, V.K. Tomer, N. Joshi, T. Dankwort, L. Lin, L. Kienle, A.C.S. Appl, Mater. Interfaces 10, 34087 (2018)

57. R. Zhang, T. Zhou, L. Wang, T. Zhang, A.C.S. Appl, Mater. Interfaces 10, 9765 (2018)

58. J. Nie, Y. Wu, Q. Huang, N. Joshi, N. Li, X. Meng, S. Zheng, M. Zhang, B. Mi, L. Lin, A.C.S. Appl, Mater. Interfaces 11, 1699 (2019)

59. Y. Wu, Q. Huang, J. Nie, J. Liang, N. Joshi, T. Hayasaka, S. Zhao, M. Zhang, X. Wang, L. Lin, J. Nanosci. Nanotechnol. 19, 5310 (2019)

60. S. Sagadevan, M.R. Bin Johan, F.A. Aziz, H.-L. Hsu, R. Selvin, H.H. Hegazy, A. Umar, H. Algarni, S.L. Roselin, J. Nanoelectron. Optoelectron. 14, 583 (2019)

61. M. Poloju, N. Jayababu, M.V. Ramana Reddy, Mater. Sci. Eng. B 227, 61 (2018)

62. X. Shi, W. Zhou, D. Ma, Q. Ma, D. Bridges, Y. Ma, A. Hu, J. Nanomater. 2015, 1 (2015)

63. Z.U. Abideen, J.-H. Kim, J.-H. Lee, J.-Y. Kim, A. Mirzaei, H.W. Kim, S.S. Kim, J. Korean Ceram. Soc. 54, 366 (2017)

64. S. Bai, C. Liu, R. Luo, A. Chen, Appl. Surf. Sci. 437, 304 (2018)

65. S. Gupta, M. Tripathi, Open Chem. 10, 279 (2012)

66. M. Parashar, V.K. Shukla, R. Singh, J. Mater. Sci. Mater. Electron. 31, 3729 (2020)

67. Y. Wang, Y. Lü, W. Zhan, Z. Xie, Q. Kuang, L. Zheng, J. Mater. Chem. A 3, 12796 (2015)

68. Y. Lü, W. Zhan, Y. He, Y. Wang, X. Kong, Q. Kuang, Z. Xie, L. Zheng, A.C.S. Appl, Mater. Interfaces 6, 4186 (2014)

69. Y. Yin, N. Zhang, J. Han, C. Liu, S. Adimi, S. Wen, X. Li, S. Ruan, Sensors Actuators B Chem. 297, 126738 (2019)

70. Z. Wu, Z. Li, H. Li, M. Sun, S. Han, C. Cai, W. Shen, Y. Fu, A.C.S. Appl, Mater. Interfaces 11, 12761 (2019)

71. D. Zhang, Z. Yang, Z. Wu, G. Dong, Sens. Actuators B Chem. 283, 42 (2019)

72. J. Zhang, D. Zeng, Q. Zhu, J. Wu, Q. Huang, W. Zhang, C. Xie, Phys. Chem. Chem. Phys. 18, 5386 (2016)

73. D. Wang, C. Zhai, L. Du, K. Gu, M. Zhang, Inorg. Chem. Front. 7, 1474 (2020)

74. Q. Mi, D. Zhang, X. Zhang, D. Wang, J. Alloys Compd. 860, 158252 (2021)

75. M. Weber, J.-H. Kim, J.-H. Lee, J.-Y. Kim, I. Iatsunskyi, E. Coy, M. Drobek, A. Julbe, M. Bechelany, S.S. Kim, A.C.S. Appl, Mater. Interfaces 10, 34765 (2018)

76. D. Zhang, H. Chen, P. Li, D. Wang, Z. Yang, IEEE Sens. J. 19, 2909 (2019)

77. M. Wang, T. Hou, Z. Shen, X. Zhao, H. Ji, Sens. Actuators B Chem. 292, 171 (2019)

78. P. Gao, R. Liu, H. Huang, X. Jia, H. Pan, RSC Adv. 6, 94699 (2016)

79. H. Hosseini, H. Ahmar, A. Dehghani, A. Bagheri, A.R. Fakhari, M.M. Amini, Electrochim. Acta 88, 301 (2013)

80. L. Zhu, J. Wang, J. Liu, M.S. Nasir, J. Zhu, S. Li, J. Liang, W. Yan, Sens. Actuators B Chem. 326, 128819 (2021)

81. W.-T. Koo, J.-S. Jang, S.-J. Choi, H.-J. Cho, I.-D. Kim, A.C.S. Appl, Mater. Interfaces 9, 18069 (2017)

82. M.G. Campbell, D. Sheberla, S.F. Liu, T.M. Swager, M. Dincă, Angew. Chemie Int. Ed. 54, 4349 (2015)

83. C.-W. Kung, A.E. Platero-Prats, R.J. Drout, J. Kang, T.C. Wang, C.O. Audu, M.C. Hersam, K.W. Chapman, O.K. Farha, J.T. Hupp, A.C.S. Appl, Mater. Interfaces 10, 30532 (2018)

84. A.U. Czaja, N. Trukhan, U. Müller, Chem. Soc. Rev. 38, 1284 (2009)

85. M.-S. Yao, W.-X. Tang, G.-E. Wang, B. Nath, G. Xu, Adv. Mater. 28, 5229 (2016)

86. W.-T. Koo, S. Qiao, A.F. Ogata, G. Jha, J.-S. Jang, V.T. Chen, I.-D. Kim, R.M. Penner, ACS Nano 11, 9276 (2017)

87. W.-T. Koo, J.-H. Cha, J.-W. Jung, S.-J. Choi, J.-S. Jang, D.-H. Kim, I.-D. Kim, Adv. Funct. Mater. 28, 1802575 (2018)

88. J.-S. Jang, W.-T. Koo, S.-J. Choi, I.-D. Kim, J. Am. Chem. Soc. 139, 11868 (2017)

89. J.-S. Jang, W.-T. Koo, D.-H. Kim, I.-D. Kim, A.C.S. Cent, Sci. 4, 929 (2018)

90. J. Wang, Q. Zhong, Y. Xiong, D. Cheng, Y. Zeng, Y. Bu, Appl. Surf. Sci. 483, 1158 (2019)

91. S. Zhang, P. Song, M. Liu, Y. Zheng, Q. Wang, Inorg. Chem. Commun. 142, 109658 (2022)

92. Z. Meng, R.M. Stolz, L. Mendecki, K.A. Mirica, Chem. Rev. 119, 478 (2019)

93. V. Shah, J. Bhaliya, G.M. Patel, P. Joshi, Top. Catal. (2022). https://doi.org/10.1007/s11244-022-01564-y

94. J.-H. Lee, T.-B. Nguyen, D.-K. Nguyen, J.-H. Kim, J.-Y. Kim, B.T. Phan, S.S. Kim, Sensors 19, 3323 (2019)

95. A.B. Gadkari, T.J. Shinde, P.N. Vasambekar, IEEE Sens. J. 11, 849 (2011)

96. D.J. Wales, J. Grand, V.P. Ting, R.D. Burke, K.J. Edler, C.R. Bowen, S. Mintova, A.D. Burrows, Chem. Soc. Rev. 44, 4290 (2015)

97. Z. Dai, T. Liang, J.-H. Lee, Nanoscale Adv. 1, 1626 (2019)

98. Y. Feng, H. Zhang, L. Fang, W. Li, Y. Wang, J. Mater. Chem. A 4, 11507 (2016)

99. D.D. Trung, N.D. Cuong, P.L. Quang, N.T. Ngoc Anh, D.T. Quang, P.C. Nam, K.Q. Trung, S.T. Nguyen, N. Van Hieu, Sens. Actuators A Phys. 296, 110 (2019)

100. M. Yuasa, T. Masaki, T. Kida, K. Shimanoe, N. Yamazoe, Sens. Actuators B Chem. 136, 99 (2009)

101. R. Malik, N. Joshi, V.K. Tomer, Coord. Chem. Rev. 466, 214611 (2022)

102. N. Joshi, G. Pransu, C. Adam Conte-Junior, Crit. Rev. Food Sci. Nutr. (2022). https://doi.org/10.1080/10408398.2022.2078950

103. V. Shah, J. Bhaliya, G.M. Patel, K. Deshmukh, Polym. Adv. Technol. 33, 3023 (2022)

104. G.M. Patel, V. Shah, J. Bhaliya, K. Mehta, *In nanotechnology-based smart remote sens. Networks disaster prev* (Elsevier, Amsterdam, 2022), pp.19–42

105. G.M. Patel, V. Shah, M. Vora, *In Shape. Mem. Compos. Based Polym. Met. 4D Print* (Springer International Publishing, Cham, 2022), pp.115–153

106. G.M. Patel, V.R. Shah, G.J. Bhatt, P.T. Deota, *In Nanosensors Smart Manuf* (Elsevier, Amsterdam, 2021), pp.555–580

107. N. Joshi, M.L. Braunger, F.M. Shimizu, A. Riul, O.N. Oliveira, *In nanosensors Environ. Appl., Kumar Tute* (Springer, Berlin, 2020), pp.131–155

108. Y. Wu, N. Joshi, S. Zhao, H. Long, L. Zhou, G. Ma, B. Peng, O.N. Oliveira Jr., A. Zettl, L. Lin, Appl. Surf. Sci. **529**, 147110 (2020)

109. N. Joshi, M.L. Braunger, F.M. Shimizu, A. Riul Jr., O.N. Oliveira, Multifunct. Mater. **4**, 032002 (2021)

110. A. Kumar, N. Joshi, S. Samanta, A. Singh, A.K. Debnath, A.K. Chauhan, M. Roy, R. Prasad, K. Roy, M.M. Chehimi, D.K. Aswal, S.K. Gupta, Sensors Actuators, B Chem. **206**, 653 (2015)

111. N. Joshi, V. Saxena, A. Singh, S.P. Koiry, A.K. Debnath, M.M. Chehimi, D.K. Aswal, S.K. Gupta, Sensors Actuators, B Chem. **200**, 227 (2014)

112. A. Mekki, N. Joshi, A. Singh, Z. Salmi, P. Jha, P. Decorse, S. Lau-Truong, R. Mahmoud, M.M. Chehimi, D.K. Aswal, S.K. Gupta, Org. Electron. Physics, Mater. Appl. **15**, 71 (2014)

113. A. Singh, A. Kumar, A. Kumar, S. Samanta, N. Joshi, V. Balouria, A.K. Debnath, R. Prasad, Z. Salmi, M.M. Chehimi, D.K. Aswal, Appl. Phys. Lett. **102**, 132107 (2013)

114. A. Singh, Z. Salmi, N. Joshi, P. Jha, P. Decorse, H. Lecoq, S. Lau-Truong, M. Jouini, D.K. Aswal, M.M. Chehimi, RSC Adv. **3**, 24567 (2013)

115. A. Singh, Z. Salmi, P. Jha, N. Joshi, A. Kumar, P. Decorse, H. Lecoq, S. Lau-Truong, D.K. Aswal, S.K. Gupta, M.M. Chehimi, RSC Adv. **3**, 13329 (2013)

116. A. Singh, Z. Salmi, N. Joshi, P. Jha, A. Kumar, H. Lecoq, S. Lau, M.M. Chehimi, D.K. Aswal, S.K. Gupta, RSC Adv. **3**, 13329 (2013)

117. S.W. Lee, W. Lee, Y. Hong, G. Lee, D.S. Yoon, Sens. Actuators B Chem. **255**, 1788 (2018)

118. S.-J. Choi, H.-J. Choi, W.-T. Koo, D. Huh, H. Lee, I.-D. Kim, A.C.S. Appl, Mater. Interfaces **9**, 40593 (2017)

119. Z. Yang, D. Zhang, H. Chen, Sens. Actuators B Chem. **300**, 127037 (2019)

120. X. Zhong, Y. Shen, S. Zhao, X. Chen, C. Han, D. Wei, P. Fang, D. Meng, Ceram. Int. **45**, 2556 (2019)

121. M. Khan, M. Rao, Q. Li, Sensors **19**, 905 (2019)

122. J. Yun, C. Zhu, Q. Wang, Q. Hu, G. Yang, Chemosphere **217**, 18 (2019)

123. J. Yun, C. Zhu, Q. Wang, Q. Hu, G. Yang, Catal. Commun. **114**, 79 (2018)

124. D. Zhang, D. Wu, X. Zong, Z. Yang, J. Mater. Sci. Mater. Electron. **30**, 11070 (2019)

125. X. Zhang, Z. Zhai, J. Wang, X. Hao, Y. Sun, S. Yu, X. Lin, Y. Qin, C. Li, ChemNanoMat **7**, 1117 (2021)

126. S. Das, V. Jayaraman, Prog. Mater. Sci. **66**, 112 (2014)

127. M.Y. Kim, Y.N. Choi, J.M. Bae, T.S. Oh, Ceram. Int. **38**, S657 (2012)

128. O. Wurzinger, G. Reinhardt, Sens. Actuators B Chem. **103**, 104 (2004)

129. S.M.A. Durrani, M.F. Al-Kuhaili, I.A. Bakhtiari, M.B. Haider, Sensors **12**, 2598 (2012)

130. M.E. Dmello, N.G. Sundaram, S.B. Kalidindi, Chem. A Eur. J. **24**, 9220 (2018)

131. M. Belaqziz, M. Amjoud, A. Gaddari, B. Rhouta, D. Mezzane, Superlattices Microstruct. **71**, 185 (2014)

132. L. Yu, Y. Li, H. Yu, K. Zhang, X. Wang, X. Chen, J. Yue, T. Huo, H. Ge, K.A. Alamry, H.M. Marwani, S. Wang, Sens. Actuators B Chem. **266**, 717 (2018)

133. L. Shao, Z. Wu, H. Duan, T. Shaymurat, Sens. Actuators B Chem. **258**, 937 (2018)

134. Z. Zhu, J.-L. Chang, C.-H. Wu, T.-L. Chou, R.-J. Wu, Sens. Actuators B Chem. **232**, 442 (2016)

135. L.F. da Silva, A.C. Catto, W. Avansi, L.S. Cavalcante, J. Andrés, K. Aguir, V.R. Mastelaro, E. Longo, Nanoscale **6**, 4058 (2014)

136. R.-J. Wu, Y.-C. Chiu, C.-H. Wu, Y.-J. Su, Thin Solid Films **574**, 156 (2015)

137. D. Zhang, Z. Yang, P. Li, X. Zhou, Sens. Actuators B Chem. **301**, 127081 (2019)

138. C.W. White, J.G. Martin, Proc. Am. Thorac. Soc. **7**, 257 (2010)

139. D.R. Patil, L.A. Patil, Sens. Actuators B Chem. **123**, 546 (2007)

140. F. Bender, C. Kim, T. Mlsna, J.F. Vetelino, Sens. Actuators B Chem. **77**, 281 (2001)

141. T. Van Dang, N. Duc Hoa, N. Van Duy, N. Van Hieu, ACS Appl. Mater. Interfaces **8**, 4828 (2016)

142. P. Li, H. Fan, Y. Cai, Colloids Surf. A Physicochem. Eng. Asp. **453**, 109 (2014)

143. S.T. Navale, V.V. Jadhav, K.K. Tehare, R.U.R. Sagar, C.S. Biswas, M. Galluzzi, W. Liang, V.B. Patil, R.S. Mane, F.J. Stadler, Sens. Actuators B Chem. **238**, 1102 (2017)

144. X. Zhao, Z. Li, X. Lou, M. Li, N. Zhang, J. Adv. Ceram. **2**, 31 (2013)

145. P. Li, H. Fan, Mater. Sci. Semicond. Process. **29**, 83 (2015)

146. J. Ma, H. Fan, X. Zheng, H. Wang, N. Zhao, M. Zhang, A.K. Yadav, W. Wang, W. Dong, S. Wang, J. Hazard. Mater. **387**, 122017 (2020)

147. E.-X. Chen, H. Yang, J. Zhang, Inorg. Chem. **53**, 5411 (2014)

148. P. Wargocki, D.P. Wyon, Y.K. Baik, G. Clausen, P.O. Fanger, Indoor Air **9**, 165 (1999)

149. H. Yang, X.-W. He, F. Wang, Y. Kang, J. Zhang, J. Mater. Chem. **22**, 21849 (2012)

150. E.-X. Chen, H.-R. Fu, R. Lin, Y.-X. Tan, J. Zhang, A.C.S. Appl, Mater. Interfaces **6**, 22871 (2014)

151. M.E. Dmello, N.G. Sundaram, A. Singh, A.K. Singh, S.B. Kalidindi, Chem. Commun. **55**, 349 (2019)

152. J. Long, S. Wang, Z. Ding, S. Wang, Y. Zhou, L. Huang, X. Wang, Chem. Commun. **48**, 11656 (2012)

153. H.-L. Wang, H. Yeh, Y.-C. Chen, Y.-C. Lai, C.-Y. Lin, K.-Y. Lu, R.-M. Ho, B.-H. Li, C.-H. Lin, D.-H. Tsai, A.C.S. Appl, Mater. Interfaces **10**, 9332 (2018)

154. D. Zhang, Z. Yang, S. Yu, Q. Mi, Q. Pan, Coord. Chem. Rev. **413**, 213272 (2020)

155. H. Yuan, S.A.A.A. Aljneibi, J. Yuan, Y. Wang, H. Liu, J. Fang, C. Tang, X. Yan, H. Cai, Y. Gu, S.J. Pennycook, J. Tao, D. Zhao, Adv. Mater. **31**, 1807161 (2019)

156. N. Van Hieu, N.A.P. Duc, T. Trung, M.A. Tuan, N.D. Chien, Sens. Actuators B Chem. **144**, 450 (2010)

157. L. Satyanarayana, K.M. Reddy, S.V. Manorama, Mater. Chem. Phys. **82**, 21 (2003)

158. A.I. Khudiar, A.K. Elttayef, M.K. Khalaf, A.M. Oufi, Mater. Res. Express **6**, 126450 (2020)

159. R. Lv, Q. Zhang, W. Wang, Y. Lin, S. Zhang, Sensors **21**, 4069 (2021)

160. T.M. Ngoc, N. Van Duy, C.M. Hung, N.D. Hoa, H. Nguyen, M. Tonezzer, N. Van Hieu, Anal. Chim. Acta **1069**, 108 (2019)

161. J. Wu, Y. Yang, C. Zhang, H. Yu, L. Huang, X. Dong, J. Wang, X. Wang, Dalt. Trans. **48**, 7720 (2019)

162. A. Natkaeo, D. Phokharatkul, J.H. Hodak, A. Wisitsoraat, S.K. Hodak, Sens. Actuators B Chem. **260**, 571 (2018)

163. L. Mai, L. Xu, Q. Gao, C. Han, B. Hu, Y. Pi, Nano Lett. **10**, 2604 (2010)

164. W. Liu, J. Wu, Y. Yang, H. Yu, X. Dong, X. Wang, Z. Liu, T. Wang, B. Zhao, J. Mater. Sci. Mater. Electron. **29**, 4624 (2018)

165. C. Zhang, S. Zhang, Y. Yang, H. Yu, X. Dong, Sens. Actuators B Chem. **325**, 128804 (2020)

166. M.-H. Pham, G.-T. Vuong, A.-T. Vu, T.-O. Do, Langmuir 27, 15261 (2011)
167. J. Ma, L. Mei, Y. Chen, Q. Li, T. Wang, Z. Xu, X. Duan, W. Zheng, Nanoscale 5, 895 (2013)
168. K. Tian, X.-X. Wang, Z.-Y. Yu, H.-Y. Li, X. Guo, A.C.S. Appl, Mater. Interfaces 9, 29669 (2017)
169. Y. Wang, F. Kong, B. Zhu, S. Wang, S. Wu, W. Huang, Mater. Sci. Eng. B 140, 98 (2007)
170. J. Wu, Y. Yang, H. Yu, X. Dong, T. Wang, New J. Chem. 43, 10501 (2019)
171. Q.-Y. Ouyang, L. Li, Q.-S. Wang, Y. Zhang, T.-S. Wang, F.-N. Meng, Y.-J. Chen, P. Gao, Sens. Actuators B Chem. 169, 17 (2012)
172. D. Zhang, J. Liu, C. Jiang, A. Liu, B. Xia, Sens. Actuators B Chem. 240, 55 (2017)
173. M. Yin, Z. Zhu, J. Alloys Compd. 789, 941 (2019)
174. D. Zhang, Z. Wu, X. Zong, Y. Zhang, Sens. Actuators B Chem. 274, 575 (2018)
175. D. Zhang, Z. Wu, P. Li, X. Zong, G. Dong, Y. Zhang, Sens. Actuators B Chem. 258, 895 (2018)
176. R.K. Kampara, P.K. Rai, B.G. Jeyaprakash, Sensors Actuators B Chem. 255, 1064 (2018)
177. V. Khorramshahi, J. Karamdel, R. Yousefi, Ceram. Int. 45, 7034 (2019)
178. G. Ren, Z. Li, W. Yang, M. Faheem, J. Xing, X. Zou, Q. Pan, G. Zhu, Y. Du, Sens. Actuators B Chem. 284, 421 (2019)
179. N. Jafari, S. Zeinali, J. Shadmehr, J. Mater. Sci. Mater. Electron. 30, 12339 (2019)
180. D. Wang, M. Chi, D. Zhang, D. Wu, J. Mater. Sci. Mater. Electron. 31, 4463 (2020)
181. C. Wang, H. Wang, D. Zhao, X. Wei, X. Li, W. Liu, H. Liu, Sensors 19, 615 (2019)
182. X. Zhou, X. Lin, S. Yang, S. Zhu, X. Chen, B. Dong, X. Bai, X. Wen, L. Geyu, H. Song, Sens. Actuators B Chem. 309, 127802 (2020)
183. S. Li, L. Xie, M. He, X. Hu, G. Luo, C. Chen, Z. Zhu, Sens. Actuators B Chem. 310, 127828 (2020)
184. J. Tan, S. Hussain, C. Ge, M. Wang, S. Shah, G. Liu, G. Qiao, Sens. Actuators B Chem. 303, 127251 (2020)
185. V. Chernikova, O. Yassine, O. Shekhah, M. Eddaoudi, K.N. Salama, J. Mater. Chem. A 6, 5550 (2018)
186. N. Ingle, P. Sayyad, G. Bodkhe, M. Mahadik, T. AL-Gahouari, S. Shirsat, M.D. Shirsat, Appl. Phys. A. 126, 723 (2020)
187. Z. Yang, D. Zhang, D. Wang, Sens. Actuators B Chem. 304, 127369 (2020)
188. K. Rui, X. Wang, M. Du, Y. Zhang, Q. Wang, Z. Ma, Q. Zhang, D. Li, X. Huang, G. Sun, J. Zhu, W. Huang, A.C.S. Appl, Mater. Interfaces 10, 2837 (2018)
189. B. Chocarro-Ruiz, J. Pérez-Carvajal, C. Avci, O. Calvo-Lozano, M.I. Alonso, D. Maspoch, L.M. Lechuga, J. Mater. Chem. A 6, 13171 (2018)
190. Z. Dou, J. Yu, Y. Cui, Y. Yang, Z. Wang, D. Yang, G. Qian, J. Am. Chem. Soc. 136, 5527 (2014)
191. Y.V. Kaneti, J. Moriceau, M. Liu, Y. Yuan, Q. Zakaria, X. Jiang, A. Yu, Sens. Actuators B Chem. 209, 889 (2015)
192. G. Lin, H. Wang, X. Li, X. Lai, Y. Zou, X. Zhou, D. Liu, J. Wan, H. Xin, Sens. Actuators B Chem. 255, 3364 (2018)
193. S.T. Navale, Z.B. Yang, C. Liu, P.J. Cao, V.B. Patil, N.S. Ramgir, R.S. Mane, F.J. Stadler, Sens. Actuators B Chem. 255, 1701 (2018)
194. T. Zhou, T. Zhang, Y. Zeng, R. Zhang, Z. Lou, J. Deng, L. Wang, Sens. Actuators B Chem. 255, 1436 (2018)
195. S. Homayoonnia, S. Zeinali, Sensors Actuators B Chem. 237, 776 (2016)
196. Y. Xiong, X. Chang, X. Qiao, K. Li, L. Zhu, F. Xia, X. Li, Q. Zheng, W. Xing, Q. Xue, Sens. Actuators B Chem. 300, 127011 (2019)
197. N. Zhang, H. Li, Z. Xu, R. Yuan, Y. Xu, Y. Cui, Nanomaterials 10, 386 (2020)
198. A. Mirzaei, J.-H. Kim, H.W. Kim, S.S. Kim, J. Mater. Chem. C 6, 4342 (2018)
199. R. Malik, V.K. Tomer, V. Chaudhary, M.S. Dahiya, S.P. Nehra, S. Duhan, K. Kailasam, Sens. Actuators B Chem. 255, 3564 (2018)
200. Y. Zhang, C. Jia, Q. Wang, Q. Kong, G. Chen, H. Guan, C. Dong, Nanomaterials 9, 1059 (2019)
201. E.M. Materón, C.M. Miyazaki, O. Carr, N. Joshi, P.H.S. Picciani, C.J. Dalmaschio, F. Davis, F.M. Shimizu, Appl. Surf. Sci. Adv. 6, 100163 (2021)
202. C.M. Miyazaki, N. Joshi, O.N. Oliveira, F.M. Shimizu, *In Metal, Metal-Oxides and Metal Sulfides for Batteries, Fuel Cells, Solar Cells, Photocatalysis and Health Sensors* (Cham: Springer International Publishing, 2021) pp.169–208
203. W.-T. Koo, S.-J. Choi, S.-J. Kim, J.-S. Jang, H.L. Tuller, I.-D. Kim, J. Am. Chem. Soc. 138, 13431 (2016)
204. D.R. Miller, S.A. Akbar, P.A. Morris, Sens. Actuators B Chem. 204, 250 (2014)
205. M. Wang, Z. Shen, X. Zhao, F. Duanmu, H. Yu, H. Ji, J. Hazard. Mater. 371, 352 (2019)
206. M.A. Andrés, M.T. Vijjapu, S.G. Surya, O. Shekhah, K.N. Salama, C. Serre, M. Eddaoudi, O. Roubeau, I. Gascón, A.C.S. Appl, Mater. Interfaces 12, 4155 (2020)
207. L. Cheng, Y. He, M. Gong, X. He, Z. Ning, H. Yu, Z. Jiao, J. Alloys Compd. 857, 158205 (2021)
208. H. Tang, Y. Li, C. Zheng, J. Ye, X. Hou, Y. Lv, Talanta 72, 1593 (2007)
209. L. Tessaro, A. Aquino, P. de Almeida Rodrigues, N. Joshi, R.G. Ferrari, C.A. Conte-Junior, Nanomaterials 12, 821 (2022)
210. Y.-W. Lu, C. Wang, N. Joshi, H. Liu, Water Cycle 3, 44 (2022)
211. A. Gusain, N.J. Joshi, P.V. Varde, D.K. Aswal, Sensors Actuators, B Chem. 239, 734 (2017)
212. X. Zhang, W. Lan, J. Xu, Y. Luo, J. Pan, C. Liao, L. Yang, W. Tan, X. Huang, Sens. Actuators B Chem. 289, 144 (2019)
213. J. Zhang, H. Lu, L. Zhang, D. Leng, Y. Zhang, W. Wang, Y. Gao, H. Lu, J. Gao, G. Zhu, Z. Yang, C. Wang, Sens. Actuators B Chem. 291, 458 (2019)
214. C. Dong, X. Xing, N. Chen, X. Liu, Y. Wang, Sens. Actuators B Chem. 230, 1 (2016)
215. Y. Yin, Y. Shen, P. Zhou, R. Lu, A. Li, S. Zhao, W. Liu, D. Wei, K. Wei, Appl. Surf. Sci. 509, 145335 (2020)
216. H. Deng, S. Grunder, K.E. Cordova, C. Valente, H. Furukawa, M. Hmadeh, F. Gándara, A.C. Whalley, Z. Liu, S. Asahina, H. Kazumori, M. O'Keeffe, O. Terasaki, J.F. Stoddart, O.M. Yaghi, Science 336, 1018 (2012)
217. X. Han, S. Yang, M. Schröder, Nat. Rev. Chem. 3, 108 (2019)
218. J. Sun, L. Sun, S. Bai, H. Fu, J. Guo, Y. Feng, R. Luo, D. Li, A. Chen, Sens. Actuators B Chem. 285, 291 (2019)
219. Y. Zhao, S. Wang, X. Zhai, L. Shao, X. Bai, Y. Liu, T. Wang, Y. Li, L. Zhang, F. Fan, F. Meng, X. Zhang, Y. Fu, A.C.S. Appl, Mater. Interfaces 13, 9206 (2021)
220. Y.F. Cui, W. Jiang, S. Liang, L.F. Zhu, Y.W. Yao, J. Mater. Chem. A 6, 14930 (2018)
221. N. Zhang, Y. Lu, Y. Fan, J. Zhou, X. Li, S. Adimi, C. Liu, S. Ruan, Sens. Actuators B Chem. 315, 128118 (2020)

**Mr. Jaydip D. Bhaliya** has received his B.Sc. in Industrial Chemistry from ITM Vocational University and M.Sc. degrees in Industrial Chemistry from ITM (SLS) Baroda University, Vadodara, India. Following his graduation, he is currently working as a project associate at CSIR-Indian Institute of Chemical Technology, Hyderabad, India. He has published 5 research papers in the peer-review international journals with renowned international publications such as the Elsevier, Wiley, and Springer etc. He has contributed 4 book chapters with peer reviewed books of international publishers. His research interest is mainly focused on the synthesis, characterization and property investigations of polymer nanocomposites for anti-coating, and gas sensing applications. Moreover, he has also participated in various national and international conferences.

**Mr. Vraj R. Shah** has received his B.Sc. in Industrial Chemistry from ITM Vocational University and M.Sc. degrees in Industrial Chemistry from ITM (SLS) Baroda University, Vadodara, India. Following his graduation, he is currently working as a teaching assistant at ITM (SLS) Baroda University, India. He has published 5 research papers in the peer-review international journals with renowned international publications such as the Elsevier, Wiley, Springer and Taylor & Francis, etc. He has contributed 8 book chapters with peer reviewed books of international publishers. He's research interest mainly focuses on Nanocomposites, gas sensing devices, computational chemistry. In addition, he has also received the prestigious award called "Best young researcher presentation award" from Sardar Vallabhbhai Patel National Institute of Technology (SVNIT), Surat. He has also participated in various national and international conferences.

**Dr. Gautam Patel** obtained PG from Institute of Science and Technology for Advanced Studies and Research (ISTAR), Vallabh Vidya Nagar and Doctoral degree from the M. S. University of Baroda, Vadodara. He is the Head and Associate Professor in Department of Applied Chemistry, School of Science, ITM (SLS) Baroda University, Vadodara, Gujarat, India. His area of specialization is Organic Synthesis, Green Chemistry, Nano Sciences and Nano technology. He has 3 patents to his name. He has published a book and 10 research papers in International Journals. He has contributed 12 book chapters with peer reviewed books of international publishers. He serves as a Referee Reviewer to many International Journals. He has attended more than 15 international and national conferences. He is a life member of Nuclear Magnetic Resonance Society (NMRS), IISc, Bangalore, India. He is a recipient of Research Fellowships in Sciences for Meritorious Students (RFSMS) under UGC Scheme during the period 2009–2013. He is a Member Observer for National Testing Agency, India. He has delivered academic talks at various places within India.

**Dr. Kalim Deshmukh** Ph.D., is a senior researcher at the New Technologies-Research Centre, University of West Bohemia, Pilsen, Czech Republic. He has over 15 years of research experience in the field of synthesis, characterization and investigations of the structure-property relationships of a wide variety of polymeric materials, polymer blends and nanocomposites for various technological applications. His research interest is mainly focused on the synthesis, characterization and property investigations of polymer nanocomposites reinforced with different nanofillers including various nanoparticles and carbon allotropes such as carbon black, carbon nanotubes, graphene and its derivatives for energy storage, energy harvesting, gas sensing, EMI shielding and high-k dielectric applications. He has published over 110 research articles in peer-reviewed journals and 36 book chapters (h-index = 41; > 6100 citations, google scholar) with renowned international publications such as the RSC, Elsevier, Wiley, Springer and Taylor & Francis, etc. Besides, he has edited/co-edited about 10 books on different topics "for Elsevier, Springer, Wiley-VCH, ACS and RSC publications. Moreover, he has actively participated and presented his research work at several international conferences and also, he has been serving as a reviewer for over 60 reputed international journals.